The QCD deconfinement transition in $N_\mathrm{f} = 2$ LQCD using Wilson fermions

Dissertation
zur Erlangung des Doktorgrades
der Naturwissenschaften

vorgelegt beim Fachbereich Physik
der Johann Wolfgang Goethe-Universität
in Frankfurt am Main

von
Alena Wilhelmine Schön
aus Bad Homburg vor der Höhe

Frankfurt am Main 2023
D30

vom Fachbereich Physik der
Johann Wolfgang Goethe-Universität als Dissertation angenommen.

Dekan: Prof. Dr. Roger Erb

Gutachter: Prof. Dr. Owe Philipsen
Prof. Dr. Marc Wagner

Datum der Disputation:

Contents

Abstract

In this thesis, we use lattice QCD to study a part of the QCD phase diagram, specifically the QCD phase transition at $\mu = 0$, where the QCD matter changes from hadron gas to quark-gluon plasma (QGP) with increasing temperature. This phase transition takes place as a crossover, but when theoretically changing the masses of the quarks, the order of the phase transition changes as well.

We focus on the region of heavy quark masses with $N_\mathrm{f} = 2$ flavours, where we investigate the critical quark mass at the second order phase transition in the form of a Z_2 point between the first-order and the crossover region. The first-order region is positioned at infinitely heavy quarks. As the quark masses decrease, the associated Z_3 centre symmetry breaks explicitly, causing the first-order phase transition to weaken until it turns into the Z_2 point and finally into a crossover.

We study this Z_2 point using simulations at $N_\mathrm{f} = 2$ and lattices of the sizes $N_\tau \in \{6, 8, 10, 12\}$, partially building on previous work, in which the simulations for $N_\tau \in \{6, 8, 10\}$ were started. The simulations for $N_\tau = 12$ are not finished yet though, but we were able to draw some preliminary conclusions. These simulations are run on GPUs and CPUs, using the codes CL^{2}QCD and openQCD-FASTSUM, respectively. Afterwards, the data goes through a first analysis step in the form of the Python program PLASMA, preparing it for the two techniques we use to analyse the nature of the phase transition.

As a first, reliable analysis method, we perform a finite size scaling analysis of the data to find the location of the Z_2 point. Since we are using lattice QCD, performing a continuum extrapolation is necessary to reach the continuum result. In regard to this, the finite size scaling analysis method is hampered by the excessive amount of simulated data that is needed regarding statistics and the total number of simulations, which is why this thesis is only an intermediate step towards the continuum limit.

This also leads to the second analysis technique we explore in this thesis. We start to design a Landau theory which describes the phase boundary for heavy masses at $N_\mathrm{f} = 2$ based on the simulated data. We develop a Landau functional for every N_τ we have simulation data for. Albeit the results are not at the same precision as the ones from the finite size scaling analysis, we are able to reproduce the position of the Z_2 point for every N_τ. Even though we are not able to take a continuum extrapolation right now, after more development takes place in future works, this approach might, in the long run, lead to a continuum result that won't need as many simulations as the finite size scaling analysis.

Deutsche Zusammenfassung

QCD beschreibt eine der vier fundamentalen Wechselwirkungen: die starke Wechselwirkung. Die drei weiteren Wechselwirkungen sind Gravitation, die schwache Wechselwirkung und die elektromagnetische Wechselwirkung. Drei der fundamentalen Wechselwirkungen lassen sich als sogenannten Quantenfeldtheorien beschreiben und sind im Standardmodell der Teilchenphysik zusammengefasst; lediglich die Gravitation wird durch die allgemeine Relativitätstheorie beschrieben. Da die Gravitation jedoch viele Größenordnungen schwächer als die restlichen Wechselwirkungen ist, spielt sie für die meisten Themen in der Teilchenphysik keine Rolle.

Die starke Wechselwirkung findet zwischen Quarks und Gluonen statt, wobei Gluonen die Austauschteilchen der starken Wechselwirkung sind. Quarks sind Spin-$\frac{1}{2}$ Teilchen, also Fermionen, mit einer nicht ganzzahligen elektronischen Ladung. Zusätzlich besitzen sie die Eigenschaft *Flavour*, welche die sechs verschiedenen Arten von Quarks (Up, Down, Strange, Charm, Bottom und Top) unterscheidet. Die Erhaltungsgröße von QCD ist die *Farbladung*, ähnlich wie bei der elektromagnetischen Wechselwirkung die elektrische Ladung. Es gibt drei verschiedene Farbladungen (rot, blau und grün), sowie deren jeweiligen Antifarben. Quarks haben immer genau eine Farbe und Antiquarks genau eine Antifarbe. Im Gegensatz zur elektromagnetischen Wechselwirkung tragen bei der starken Wechselwirkung aber nicht nur Quarks, sondern auch die Austauschteilchen, also Gluonen, eine Farbladung. Dadurch können auch die Gluonen miteinander wechselwirken, was auch daran erkennbar ist, dass die QCD durch die nicht-abelsche Eichgruppe $SU(3)$ beschrieben wird. Für die Farbzusammensetzung der Gluonen ergeben sich aus der Gruppentheorie acht Möglichkeiten, welche als Kombination aus Farbe und Antifarbe realisiert ist, über die die Farbladung der Quarks bei einer Wechselwirkung getauscht werden. Farbladung lässt sich nicht beobachten, woraus sich schließen lässt, dass alle physikalischen Zustände farblos sein müssen. Das bedeutet, dass Quarks nur als gebundene Zustände auftreten können: als *Hadronen*. Die zwei wichtigsten Arten von Hadronen sind *Baryonen* und *Mesonen*. Baryonen bestehen aus drei Quarks mit jeweils unterschiedlicher Farbladung, sodass alle drei Farben in einem Baryon vorkommen. Genauso gibt es Antibaryonen, die aus drei Antiquarks mit allen drei Antifarben bestehen. Mesonen bestehen aus einem Quark und einem Antiquark, wobei das Quark eine beliebige Farbe trägt und das Antiquark die dazugehörige Antifarbe, dadurch sind diese Hadronen farblos. Es existieren noch weitere farblose Hadronen, wie Pentaquarks, die aus vier Quarks und einem Antiquark bestehen. Dabei liegen alle drei Farbladungen vor, die doppelt vorkommende Farbladung ist die zur Antifarbe zugehörige. Eine weitere Möglichkeit sind Tetraquarks, die aus zwei Quarks und zwei Antiquarks bestehen, mit zwei Farben und den entsprechenden Antifarben. Durch die Selbst-

wechselwirkung der Gluonen könnten auch Glueballs existieren, Teilchen, die nur aus Gluonen bestehen.

Der Umstand, dass Quarks und Gluonen nur in gebundenen Zuständen auftreten können, wird auch als *Confinement* bezeichnet. Ein Effekt des Confinements ist, dass die Kopplungsstärke zwischen zwei verbundenen Quarks zunimmt, wenn diese weiter voneinander entfernt werden. Wenn die Energie, die aufgewandt wird um die beiden Quarks zu trennen, hoch genug wird, entsteht ein neues Quark-Antiquark Paar, welches sich mit den ursprünglichen, jetzt getrennten, Quarks verbindet und dadurch neue, farblose Zustände entstehen lässt. Das Gegenteil des Confinements ist die *asymptotische Freiheit*. Bei großen Energien, und bei kleinen Abständen zwischen zwei Quarks, nimmt die Kopplungsstärke zwischen den Quarks ab, wodurch sich diese wie asymptotisch freie Teilchen verhalten. Auch dieser Effekt beruht auf der nicht-abelschen Eichsymmetrie $SU(3)$ der QCD.

Bei extrem hohen Temperaturen oder auch Baryon-Dichten sind Quarks und Gluonen nicht mehr durch Confinement gebunden, sondern liegen als quasi-freie Teilchen in Form eines *Quark-Gluon-Plasmas* vor. Aufgrund der extremen Umstände die es braucht, damit ein Quark-Gluon-Plasma entsteht, kommt es in der Natur kaum vor. Ein Zeitpunkt, zu dem ein Quark-Gluon-Plasma existiert hat, war kurz nach dem Anfang des Universums, zwischen 10^{-33} bis 10^{-32} Sekunden nach dem Urknall hat sich ein Quark-Gluon-Plasma gebildet. Ungefähr 10^{-6} Sekunden nach dem Urknall war das Universum aber bereits so weit heruntergekühlt, dass ein Phasenübergang zu hadronischer Materie stattfand. Zum jetzigen Zeitpunkt könnte ein Quark-Gluon-Plasma nur noch in Neutronensternen natürlich vorkommen, es ist aber auch möglich, auf der Erde mit Hilfe von Schwerionenbeschleunigern wie dem LHC am CERN in Genf ein Quark-Gluon-Plasma zu erzeugen und damit das Phasendiagramm der QCD zu untersuchen.

Auch theoretische Untersuchungen von QCD und deren Phasendiagramm sind nicht ohne Probleme möglich. Die intrinsische Energieskala zeigt den hadronischen Bereich und ist als $\Lambda_{QCD} \approx 200 - 400$ MeV definiert. In diesem Bereich divergiert die Kopplung, weswegen perturbative Ansätze nur oberhalb der intrinsischen Energieskala der QCD angewendet werden können, zur Untersuchung dieser Energiebereiche muss deswegen auf andere Methodiken ausgewichen werden. Eine viel genutzte Möglichkeit hierzu ist *Gitter QCD*. Hierbei wird die kontinuierliche Raum-Zeit durch ein diskretes Gitter mit Gitterabstand a ersetzt, was einem ultraviolettem Cut-Off im Impulsraum bei $1/a$ entspricht, durch den die Theorie regularisiert wird. Die ursprüngliche QCD wird prinzipiell wieder erreicht, in dem der Gitterabstand gegen null geschickt wird, $a \to 0$, auch wenn sich dieser Prozess in realen Berechnungen komplizierter gestaltet.

Gitter QCD kann durch eine Wick-Rotation in die euklidische Raum-Zeit überführt werden. In dieser Formulierung lässt sie sich gut mit Monte-Carlo-Simulationen analysieren, auch wenn diese, je nach Problemstellung, sehr rechenintensiv werden können. Insbesondere leichte Quarkmassen lassen sich nur unter hohem Rechenaufwand simulieren. Außerdem schränkt das *Vorzeichenproblem* den Bereich, in dem Simulationen durchgeführt werden können, auf $\mu_B/T \gtrsim 1$ ein, da außerhalb dieses Bereichs die Fermionendeterminante stark oszilliert und damit nicht mehr ausgewertet werden kann.

Ein weiteres Problem der Gitter QCD ist das *Dopplerproblem*, welches auftritt, wenn die QCD naiv diskretisiert wird. Durch das Dopplerproblem besitzt die Theorie sechzehn Fermionen, anstatt, wie im Kontinuum, lediglich eines. Es gibt eine Vielzahl an Diskretisierungsmethoden, um mit dem Dopplerproblem umzugehen, die jedoch alle auch gewisse Nachteile mit sich bringen. Der Hauptgrund dafür ist das Nielsen-Ninomiya-Theorem, welches besagt, dass es nicht möglich ist, auf dem Gitter gleichzeitig Doppler zu beseitigen und eine chirale Symmetrie zu realisieren.

In dieser Arbeit simulieren wir Gitter QCD mit *Wilson Fermionen*, bei denen das Dopplerproblem durch das Hinzufügen eines Massenterms gelöst wird, durch den die unphysikalischen Fermionen von der Theorie entkoppeln. Dadurch wird allerdings, wie erwartet, die chirale Symmetrie explizit gebrochen. Für unsere Arbeit ist dies allerdings nicht von Belang, da für unsere Untersuchungen nur die Zentrumssymmetrie relevant ist. Für die Simulationen mit einem Hybrid-Monte-Carlo Algorithmus benutzen wir zwei Codes, CL^{2}QCD und openQCD-FASTSUM. CL^{2}QCD benutzt GPUs und wurde in der Arbeitsgruppe von Owe Philipsen entwickelt. Mit diesem Code haben wir auf drei Clustern Simulationen laufen lassen, dem L-CSC an der GSI in Darmstadt, auf dem LOEWE-CSC und dessen Nachfolger Goethe-HLR, beide in Frankfurt. openQCD-FASTSUM beruht auf dem etablierten Code openQCD, welcher initial von Martin Lüscher und Stefan Schaefer entwickelt wurde. Die Weiterentwicklung openQCD-FASTSUM stammt von Jonas Rylund Glesaaen und Benjamin Jäger. Dieser Code läuft auf CPUs und wurde auf dem Cluster Goethe-HLR in Frankfurt verwendet.

Mit den so generierten Daten untersuchen wir im QCD Phasendiagramm den Phasenübergang von hadronischer Materie zu Quark Gluon Plasma bei chemischem Potential $\mu = 0$ und einer Temperatur zwischen $150 - 170$ MeV. Dort ist der Phasenübergang kein echter Phasenübergang, sondern ein *Crossover*, ein Übergang zwischen zwei Phasen, bei dem keine Diskontinuitäten, Singularitäten oder Änderungen in der Symmetrie des Systems auftreten. Verändert man allerdings die Quarkmassen und die Anzahl der Flavour, also der Quarksorten, so kann sich die Ordnung des Phasenübergangs ändern. Dies wird im *Columbia Plot* dargestellt, welcher die Änderung der Ordnung des Phasenüberganges in Abhängigkeit der drei leichtesten Quarks zeigt, wobei up und down Quark als entartet angenommen werden. Wenn eine der Quarkmassen unendlich wird, so entkoppelt diese von der Theorie und die Anzahl der Flavour verringert sich. Bei sehr kleinen Quarkmassen $m_q \to 0$ und sehr großen Quarkmassen $m_q \to \infty$ geht man davon aus, dass die Ordnung des Phasenüberganges in einen Phasenübergang erster Ordnung übergeht. Bei Phasenübergängen erster Ordnung ändert sich die Symmetrie des Systems, zusätzlich wird dort latente Wärme erzeugt. Ein Phasenübergang wird auch durch den *Ordnungsparameter* angezeigt, der bei einem Phasenübergang erster Ordnung eine Diskontinuität hat. Dort springt er von null auf einen von null verschiedenen Wert. Im Gegensatz dazu steigt bei einem Crossover der Ordnungsparameter kontinuierlich an. Da eine Linie eines Phasenübergangs erster Ordnung in einem Endpunkt zweiter Ordnung endet, liegt zwischen der Crossover Region und den Regionen erster Ordnung eine Linie eines Phasenübergangs zweiter Ordnung, eine Z_2-Linie. Phasenübergänge zweiter Ordnung sind auch durch eine Änderung der Symmetrie charakterisiert, allerdings hat der Ordnungsparameter keine direkte Diskontinuität, sondern nur dessen erste Ab-

leitung. Die Struktur des Columbia Plots konnte noch nicht abschließend bestätigt werden, gerade im Bereich kleiner Quarkmassen ist die Unsicherheit bezüglich der Struktur groß, da sich dieser Bereich nur schwer untersuchen lässt, weil Simulationen mit sinkender Quarkmasse immer kostenintensiver werden.

In dieser Arbeit beschäftigen wir uns mit dem Bereich schwerer Massen, $m_q \to \infty$, der Phasenübergang in diesem Bereich ist der Deconfinement Übergang. Wir betrachten die Theorie mit zwei entarteten Quarkflavours, $N_\mathrm{f} = 2$, und befinden uns dementsprechend an der oberen Kante des Columbia Plots, wo die Masse des strange Quarks unendlich ist ($m_s \to \infty$), wodurch dieses von der Theorie entkoppelt. Der Deconfinement Phasenübergang und dessen Ordnung hängt mit der Zentrumssymmetrie zusammen, der betrachtete Ordnungsparameter ist der *Polyakovloop*. Wenn der Polyakovloop gleich null ist, so liegt Confinement vor. Wenn der Polyakovloop ungleich null wird, setzt das Deconfinement ein. Bei unendlichen Massen bricht die Zentrumssymmetrie spontan, deswegen liegt ein Phasenübergang erster Ordnung vor. Wenn die Quarkmassen endlich werden, bricht die Zentrumssymmetrie explizit, wodurch der Phasenübergang erster Ordnung geschwächt wird. Für einen gewissen Massenbereich bleibt der Phasenübergang erster Ordnung bestehen, bis er schließlich in der Z_2-Linie endet und letztendlich in einen Crossover übergeht. Da wir die Änderung der Ordnung des Phasenüberganges nur auf der $N_\mathrm{f} = 2$-Linie im Columbia Plot betrachten, sprechen wir im Folgenden nicht mehr von einer Z_2-Linie sondern von einem Z_2-Punkt.

Das Ziel ist es nun, den Z_2-Punkt für $N_\mathrm{f} = 2$ bei schweren Massen zu lokalisieren. Zuerst lassen wir dazu die besprochenen Gitter QCD Simulationen mit dem Polyakovloop als Ordnungsparameter laufen, allerdings liefern diese nicht direkt den Kontinuumswert. Deswegen muss erst der Gitterabstand gegen null geschickt werden ($a \to 0$). Dafür müssen Simulationen an verschiedenen Gitterabständen durchgeführt werden. Der Gitterabstand lässt sich allerdings in Simulationen nicht direkt kontrollieren, stattdessen wird er über die temporale Ausdehnung des Gitters angepasst, da $1/T = aN_\tau$ gilt. Neben der temporalen Ausdehnung hat das Gitter auch eine dreidimensionale räumliche Ausdehnung N_s, welche für unsere Zwecke einige Faktoren größer sein muss als die zeitliche Ausdehnung N_τ. Aus diesem Grund haben wir für vier verschiedene temporale Ausdehnungen $N_\tau \in \{6, 8, 10, 12\}$ unterschiedliche räumliche Ausdehnungen N_s simuliert. Die Simulationen für $N_\tau = 12$ sind noch nicht abgeschlossen worden, es fehlt sowohl an Statistik als auch an weiteren Volumina N_s, wobei die bisher simulierten räumlichen Ausdehnungen nicht groß genug sind. Beides liegt vor allem daran, dass mit steigenden N_τ die Simulationszeit im Vergleich zur Vergrößerung des zu simulierenden Gitters überproportionalen ansteigt. Bei den niedrigen N_τ hat es ausgereicht, N_s $4-6$ Mal größer als N_τ zu wählen, während bei $N_\tau = 10$ mit diesen Faktoren bereits die Auswertungsmethode angepasst werden musste, um *finite size Effekte* zu vermindern. Bei $N_\tau = 12$ ist bereits absehbar, dass die Faktoren höher sein müssen, da die finite size Effekte mit steigendem N_τ anwachsen. Die beste Möglichkeit, um damit umzugehen ist es, höhere N_s zu wählen, was aber die Simulationszeiten ansteigen lässt. Ein weiterer Grund für die steigende Dauer der Simulationen mit höheren N_τ ist die Autokorrelationszeit, die mit größerem N_τ wächst. Da bei Monte Carlo Simulationen die einzelnen Datenpunkte miteinander korreliert sind, muss, um unkorrelierte Daten zu erzeugen,

durch die Autokorrelationszeit berechnet werden, wie stark die Korrelation zwischen den Datenpunkten ist. Anhand dieser wird die Anzahl der unkorrelierten Ereignisse bestimmt, die durch die Anzahl der Datenpunkte geteilt durch das Doppelte der Autokorrelationszeit bestimmt wird, $N_{\text{indep}} = \frac{N}{2\tau_{\text{int}}}$. Daraus folgt, dass für steigende Autokorrelationszeiten die Anzahl der tatsächlich zur Verfügung stehenden Datenpunkte abnimmt. Wir konnten feststellen, dass die Autokorrelationszeit mit steigendem N_τ besonders um den Z_2 Punkt herum stark ansteigt. Dadurch müssen immer mehr Datenpunkte simuliert werden, um eine vergleichbare Anzahl an unkorrelierten Datenpunkten zu erreichen.

Aus den Simulationsdaten haben wir den Z_2-Punkt für jede der temporalen Ausdehnungen N_τ bestimmt. Dafür haben wir zuerst eine *finite size scaling Analyse* verwendet, die bereits in vorherigen Arbeiten angewandt wurde und verlässliche und präzise Ergebnisse liefert. In dieser Analyse werden Simulationen an verschiedenen N_s je N_τ benötigt, da der Z_2 Punkt bestimmt wird, indem die Datenpunkte über verschiedenen Quarkmassen je N_s gefittet werden und der Schnittpunkt aus diesen N_s-Linien den Z_2 Punkt identifiziert. Bei dieser Methodik sind die wachsenden finite size Effekte ein großes Problem. Teilweise können diese über einen zusätzlichen Korrekturterm abgefangen werden, jedoch werden für höhere temporale Ausdehnungen weiterhin größere Volumina benötigt werden. Dadurch, und durch die generell großen benötigten Datenmengen, kommen bei dieser Methode besonders die Nachteile des steigenden Ressourcenbedarfs der Simulationen zu tragen.

Aus diesem Grund wurde in dieser Arbeit ein weiterer Ansatz zur Lokalisierung des Z_2-Punktes getestet. Diese Analyse beruht auf der Entwicklung einer Landau Theorie, welche die Phasengrenze für schwere Quarkmassen mit $N_\text{f} = 2$ beschreibt. Dieser Ansatz befindet sich noch in der Entwicklung, weshalb wir damit die Lokalisierung des Z_2-Punktes nicht weiter vorantreiben konnten, sondern nur die aus der finite size scaling Analyse gewonnenen Ergebnisse bestätigt haben. Dabei konnten wir für jede temporale Ausdehnung N_τ ein eigenes Landau Funktional finden, welches zu einem ähnlichen Wert für die Lokalisation des Z_2-Punktes wie die finite size scaling Analyse führt. Hierfür reicht es jedoch aus, ein einziges Volumen N_s zu betrachten. Dieses muss, wie wir festgestellt haben, nicht mal einen besonders hohen Faktor größer als N_τ sein, die besten Ergebnisse erzielte ein Faktor von 5.

Um zu sehen, wie nah wir mit diesen beiden Analysen dem Kontinuumslimes bereits gekommen sind, haben wir schlussendlich noch die Massen der Pionen an den Z_2 Punkten je N_τ bestimmt. Dafür betrachtet man die Pionenmasse in Gittereinheiten, in unseren Fällen liegt diese immer bei $am_\pi > 1$, was bedeutet, dass es noch nicht möglich ist, einen sinnvollen Kontinuumslimes aus den Ergebnissen zu ziehen. Der Grund hierfür ist, dass eine Pionenmasse mit $am_\pi > 1$ bedeutet, dass das Pion kleiner als der Gitterabstand a ist, wodurch es nicht durch den Gitterabstand aufgelöst werden kann. Es ist jedoch zu beobachten, dass sich für $N_\tau = 10$ und $N_\tau = 12$ die Pionenmasse dem Wert 1 langsam annähert, auch wenn trotzdem in zukünftigen Arbeiten noch weitere temporale Gitterausdehnungen N_τ untersucht werden müssen.

Insgesamt stellt diese Arbeit damit in gewisser Weise ein Zwischenschritt zum Erreichen eines Kontinuumswerts für den Z_2-Punkt für schwere Massen für $N_\text{f} = 2$ dar. Wir konnten auf früheren Arbeiten aufbauen, ein genaueres Bild über den verblei-

benden Simulationsaufwand für die Analyse mithilfe der finite size scaling Methode entwickeln, sowie mit der Landau Methodik voraussichtlich einen Startpunkt für weitere, mit weniger Simulationsaufwand verbundene, Analysen setzen.

Kapitel 1

Introduction

Phase transitions are an important phenomenon in our daily lives, they are all around us. The most important and also well-known phase transitions are the ones of water, at temperatures below 0°C it freezes, at temperatures above 100°C it boils, and then turns into vapour. Those transitions not only depend on temperature, but also on pressure, which needs to be at 1013 hPa for the phase transitions to take place at those exact temperatures. These are phase transitions we experience daily, when we cook or drink tea, we bring water to a boil, transitioning the water from a fluid to gas. When putting ice cubes in our drinks, they heat up and the water of the ice cubes transitions from its solid, frozen state into a liquid state. Water also condenses on multiple surfaces, for example on glasses when going from a cooler to a warmer place, like when in winter, one comes from the cold outside into a warm house. Other phase transitions influencing our day-to-day lives are, for example, the phase transitions of metal or plastic, which, when molten, can be formed easily and then cool down to form a solid object. Refrigerators are another example, they use phase transitions to keep our food from perishing by keeping it cool and fresh.

But there are also phase transitions that we are not experiencing in our daily lives, but which are nevertheless important topics of research. One example which played a role in the formation of our world, is the phase transition of QCD, between the hadron gas phase and the Quark-Gluon-Plasma. This phase transition took place at the very beginning of our universe, about 10^{-33} to 10^{-32} seconds after the Big Bang, the universe was extremely dense and heated up to such extreme temperatures, that a quark-gluon plasma (QGP) was produced. Afterwards, the universe got less dense and cooled down significantly, leading to the creation of hadrons at about 10^{-6} seconds after the Big Bang. Since the temperatures and densities needed to form a QGP are immense, a QGP might also exist in neutron stars, but on Earth it can only be observed in high-energy particle accelerators. In those experiments, the shape of this phase transition in the QCD phase diagram is explored via heavy-ion collisions through the tracking of jets [1, 2]. To explore the whole phase transition, multiple experiments are running worldwide, exploring the phase transition at different temperatures and baryon densities. An overview of the most important experiments and their parameter range can be seen in Figure 1.1. Depicted are the experiments LHC at CERN in Genf, RHIC at Brookhaven National Laboratory in Upton, SPS at CERN in Genf, FAIR at GSI in Darmstadt (currently

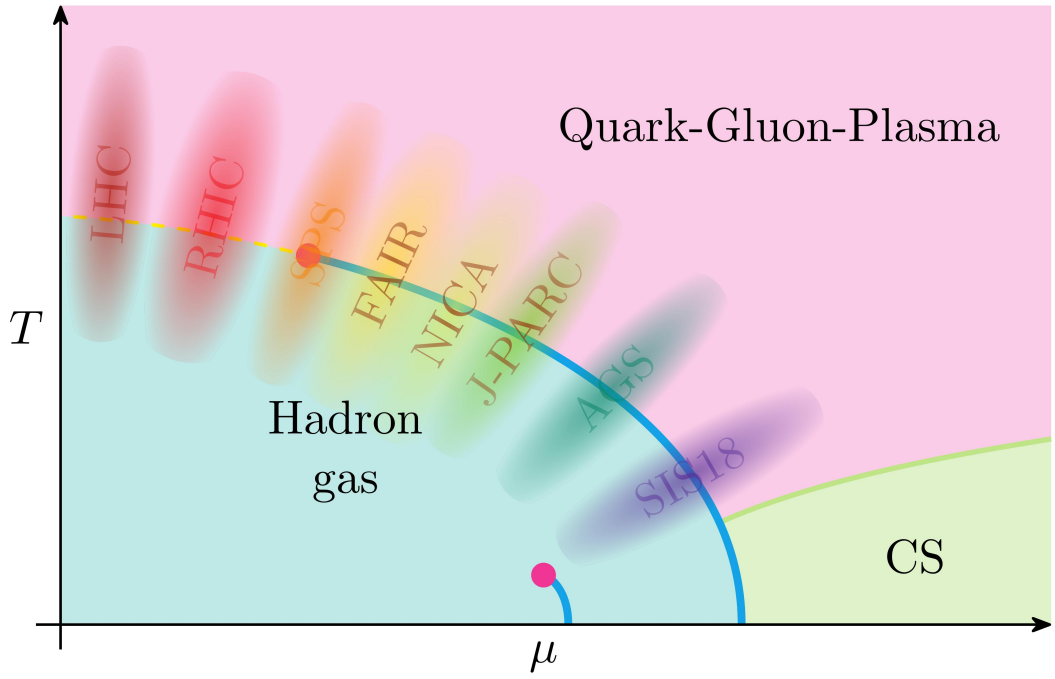

Figure 1.1: Schematic illustration of the QCD phase diagram in the $T - \mu$-plane. Some of the most important experiments for probing the phase diagram are schematically represented. Since their range might be larger than depicted here, the borders are shaded.

still under construction), NICA in Dubna (currently to be commissioned in 2023), J-PARC in Tokai, AGS at Brookhaven National Laboratory in Upton and SIS18 at GSI in Darmstadt.

But what exactly are QCD and QGP? QCD, which stands for quantum chromodynamics, describes the interaction between quarks and gluons, which are the constituents of nucleons [3, 4], under the strong interaction. Quarks are spin-$\frac{1}{2}$ particles, so fermions, with a non-integer electric charge. Quarks come in six flavours, which are different types of quarks with different charges, quantum numbers and weights: up (2.3 MeV), down (4.8 MeV), strange (95 MeV), charm (1.3 GeV), bottom (4.2 GeV) and top (173 GeV) [5]. Gluons are gauge bosons, the massless exchange particles of QCD.

The strong interaction isn't the only fundamental interaction though, there are also the electromagnetic interaction, the weak interaction and gravity. Three of the fundamental forces, excluding gravity, are described by the *Standard Model of particle physics*. The Standard Model is built as a quantum field theory, just like the three underlying fundamental forces. A quantum field theory is defined and categorised through its corresponding symmetry groups, which are also called gauge groups. Gravity is not included since it can't be described as a quantum field theory, because the Feynman diagrams have divergences that make the theory non-renormalisable. This, however, does not render the Standard model useless, because the gravitational force between particles is magnitudes smaller than the forces from the other interactions. Nearly all particles have a mass, with the exceptions being

the photon and gluon. This mass stems from the Higgs mechanism [6, 7], which works via the Higgs field. When the symmetry associated with the Higgs field is spontaneously broken, the particles which interact with the Higgs field get a mass. The Higgs boson, the particle related to the excitation of the Higgs field, was found at LHC at CERN in 2012 [8, 9]. This particle was postulated in 1964 by three independent groups, by Robert Brout and François Englert, by Peter Higgs and by Gerald Guralnik, Carl R. Hagen and Tom Kibble. Even though quarks have a mass stemming from the Higgs mechanism, the quark condensate, consisting of the constituent quarks and *sea quarks*, is only responsible for 9% of the mass of a nucleon. The remaining 91% of the mass stem from glue field and quark energy, as well as from a trace anomaly [10].

Focusing on the strong interaction again, its theory, QCD, is also formulated as a quantum field theory (QFT), to be precise as a non-Abelian gauge field theory [11, 12, 13, 14]. QCD is associated with the quantum number *colour*. Historically, colour charge was first introduced because of the Δ^{++} baryon. The particle contains three up-quarks with the same spin, which leads to a symmetric wave function, even though the wave function has to be antisymmetric because the Δ^{++} baryon is a fermion. This is solved by introducing the colour charge, which can take on three different values so that the three quarks are distinguishable, and the wave function is asymmetric. The number of different colours is also related to the symmetry group of QCD, therefore we know that $N_c = 3$, since the symmetry group of QCD is $SU(3)$. All particles interacting under the strong force have a colour charge. The three colours are red, blue and green, but there also exists an associated anticolour to every colour. Colour charge cannot be observed, which means that all physical states must be colourless. This can be realised by combining three quarks, all of different colour charge, creating a baryon, or an antibaryon, when three antiquarks with all three anticolours are combined. Another possibility is a meson, a particle built out of a quark and an antiquark, where the antiquark carries the matching anticolour to the colour of the quark. Further options are pentaquarks, built out of four quarks and an antiquark, where the quarks have all three colours, and the colour being present twice is matched by the anticolour of the antiquark. Furthermore, tetraquarks are built out of two quarks and two antiquarks, where the anticolours of the antiquarks match the colours of the quarks. But also gluons have colour charge, which makes QCD quite special, because this means that they themselves interact under the strong interaction, even though they are the exchange particles of the theory. This means, that glueballs could exist, particles only constructed out of gluons. The property of self-interaction is also connected to the non-Abelian gauge group $SU(3)$ of QCD. From group theory it is also known that there have to exist eight different gluons, which all have a different colour charge [15, 16], which is always a combination of a colour and anticolour. When the gluons interact with quarks, the quarks change their colour charge according to the gluon.

The fact that quarks exist in colour-bound states only, so in colourless states, is also called *confinement*. The opposite of confinement is *asymptotic freedom* [17, 18, 14, 19, 20, 13, 21], at high energies or small distances between quarks, the coupling is getting weak so that the particles appear asymptotically free. Confinement and asymptotic freedom indicate the existence of a quark-gluon plasma (QPG),

which occurs at extremely high temperatures or high baryon densities. There, quarks and gluons are not bound by confinement anymore, they exist as quasi-free particles and colour charges are free. The phase transition to quark-gluon plasma is depicted in the QCD phase diagram Figure 1.1. The phase structure is under heavy investigation, experimentally and theoretically. Theoretical explorations of the QCD phase diagram face many problems, caused by the non-Abelian nature of the theory. The intrinsic mass scale of QCD at the length scale of $\mathcal{O}(1)$, where quarks and gluons interact, lies between $\Lambda_{QCD} \approx 200 - 400$ MeV, this defines the length at which QCD interactions take place as $1/\Lambda_{QCD} = 1$ fm. Perturbation theory is only applicable at energies $E \gg \Lambda_{QCD}$ since the coupling diverges in the region of Λ_{QCD} because of confinement. To explore these energy regions, other techniques like *lattice QCD* (LQCD) can be used [22, 23, 24, 25]. LQCD is not free from problems though, it is especially hindered by the sign problem [26], which makes the numerical evaluation of the fermion determinant impossible because it is highly oscillatory, and therefore the partition function can't be evaluated. The sign problem does not appear everywhere though. At $\mu_B = 0$, the sign problem does not exist because the fermion determinant doesn't become imaginary. The fermion determinant can still be evaluated up to $\mu/T \gtrsim 1$ in a reliable way when using different approaches circumventing the sign problem [27].

In this work, we want to focus on the QCD phase diagram at $\mu = 0$, where the phase transition is confirmed to take place as a crossover at $T = 150 - 170$ MeV [28]. Our objective is to learn more about this phase transition as a function of the quark masses. When the quark masses are varied to unphysical values, the crossover phase transition changes to a different order of phase transition. This is of interest because restrictions for the physical regions follow from the phase structure at unphysical quark masses. We will study the sector where the up and down quark have a degenerate, heavy mass, and the other quarks are infinitely heavy and therefore decouple from the theory. When varying the masses of the degenerate light quarks, we expect the phase transition to shift from a crossover to a first order phase transition. We want to locate the point at which the order of the phase transition changes, which is indicated by a Z_2-point. The goal is to get closer to a continuum extrapolation of the mass of the Z_2-point at $\mu = 0$ in the heavy mass region. To reach this goal, we perform simulations and analyse those with a *finite size scaling analysis*, which is impacted by finite size effects. We also started with the first step of exploring this phase boundary via *Landau theory*.

In Chapter 2 we will discuss the basics of QCD on the lattice at zero and finite temperature and its symmetries. Chapter 3 will give an overview of the numerical methods and codebases used for the simulations. Chapter 4 explores the topic of phase transitions, including critical exponents, scaling laws and Landau theory, as well as the QCD phase diagram and the Columbia plot. In Chapter 5 we describe how the simulations were run, the two different methods of analysing the simulation results, the results of these analyses and the difficulties we were presented with. Finally, Chapter 6 will give a conclusion and an outlook into the future.

Chapter 2

Lattice Quantum Chromodynamics

This chapter gives a short introduction to continuum QCD, before it moves on to LQCD, which is its main focus. We will discuss the Wilson fermion discretisation as well as Wilson and Polyakov loops. We will also give an overview of the continuum limit, LQCD at finite temperatures at zero chemical potential and the centre symmetry.

For additional information, refer to the standard literature on which this section is based [22, 23, 29, 30, 31]. In this thesis, we will use Euclidean space time, details on the notation and other conventions can be found in Appendix A.1. We also use the Einstein summation convention.

2.1 Continuum QCD

QCD describes the interactions between quarks and gluons and is formulated as a quantum field theory. The goal of this section is to derive and describe the actions and the partition function of continuum QCD.

Dirac 4-spinors describe the fermions of the theory, which are the quarks:

$$\psi^{(f)}(x)_{\substack{\alpha \\ c}}, \bar{\psi}^{(f)}(x)_{\substack{\alpha \\ c}}, \tag{2.1}$$

where x denotes the position in space-time, $\alpha \in \{1, 2, 3, 4\}$ describes the Dirac index, $c \in \{1, \cdots, N_\mathrm{c}\}$ stands for the colour index and $f \in \{1, \cdots, N_\mathrm{f}\}$ for the flavour index. The physical values for the colour and flavour index are $N_\mathrm{c} = 3$ and $N_\mathrm{f} = 6$. In this work we will exclude the heavy quark flavours though and only consider the up and down quark, leading to $N_\mathrm{f} = 2$ as the flavour index. Also, in Euclidean space-time, ψ and $\bar{\psi}$ are independent integration variables.

The gluons are described as gauge fields

$$A_\mu(x)_{cd}, \tag{2.2}$$

with x again denoting space-time, the colour indices c, d and the Euclidean Lorentz-index $\mu \in \{1, 2, 3, 4\}$. These gauge fields are hermitian, traceless matrices, which makes them an element of the Lie algebra $su(3)$.

The gauge fields can therefore also be written as:

$$A_\mu(x) = \sum_{i=1}^{8} A_\mu^{(i)}(x) T_i, \tag{2.3}$$

with the generators of $SU(3)$ represented through T_i, which are a basis for traceless hermitian 3×3 matrices. $A_\mu^{(i)}$ are the colour components, with $i \in \{1, \cdots, 8\}$.

With these components at hand, the fermionic part of the QCD action can be built as a bilinear functional in the fields $\psi^{(f)}(x)$ and $\bar{\psi}^{(f)}(x)$ which also includes a coupling term to the gluonic field $A_\mu(x)_{cd}$ and sums over the actions of all individual flavours:

$$\mathcal{S}_\mathrm{f}[\psi, \bar{\psi}, A] = \sum_{f=1}^{N_\mathrm{f}} \int \mathrm{d}^4x \; \bar{\psi}^{(f)}(x)_c^\alpha \left((\gamma_\mu)_{\alpha\beta} \left(\delta_{cd} \partial_\mu + i A_\mu(x)_{cd} \right) + m^{(f)} \delta_{\alpha\beta} \delta_{cd} \right) \psi^{(f)}(x)_{\beta}^{\,d}. \tag{2.4}$$

Since the coupling to the gluon fields is identical for all quark flavours, the flavour index of the sum only has an influence on the masses of the quarks $m^{(f)}$. The gluon fields $A_\mu(x)_{cd}$ are coupled to the quark fields $\psi^{(f)}(x)$ and $\bar{\psi}^{(f)}(x)$ via the summation over the colour indices c and d, the coupling is changed for each component μ through the multiplication with the Euclidean Dirac matrices γ_μ (c.f. Appendix A.1). Additionally, the Dirac components of the quark fields are mixed by the partial derivatives ∂_μ.

The fermion action is required to be invariant under $SU(3)$ colour rotations, denoted by the $SU(3)$ matrices $\Omega(x)$, which are complex 3×3 matrices that have to be unitary with a determinant of 1, since they are part of the $SU(3)$ group. These matrices are not commutative, making the $SU(3)$ a non-Abelian group, from which follows that QCD is a Yang-Mills theory [32].

To fulfil the required invariance, the QCD action needs to be invariant under the following transformations:

$$\begin{aligned} \psi(x) \to \psi'(x) &= \Omega(x)\psi(x) \\ \bar{\psi}(x) \to \bar{\psi}'(x) &= \bar{\psi}(x)\Omega(x)^\dagger \\ A_\mu(x) \to A'_\mu(x) &= \Omega(x)A_\mu(x)\Omega(x)^\dagger + i(\delta_\mu \Omega(x))\Omega(x)^\dagger. \end{aligned} \tag{2.5}$$

To arrive at the transformation of $A_\mu(x)$, the transformations of $\psi(x)$ and $\bar{\psi}(x)$ have to be applied to the fermion action, from which then the transformation of $A_\mu(x)$ can be determined.

With these transformations at hand, it is now possible to transform the complete fermionic QCD action

$$\mathcal{S}_\mathrm{f}[\psi', \bar{\psi}', A'_\mu] = \mathcal{S}_\mathrm{f}[\psi, \bar{\psi}, A_\mu]. \tag{2.6}$$

Next, the gauge action of QCD has to be defined. An important part of the gauge action is the field strength tensor $F_{\mu\nu}(x)$, which is defined using the covariant derivative $D_\mu(x)$:

$$D_\mu(x) = \delta_\mu + i\, A_\mu(x), \tag{2.7}$$

which transforms as:

$$D_\mu(x) \to D'_\mu(x) = \partial_\mu + i A'_\mu(x) = \Omega(x) D_\mu(x) \Omega(x)^\dagger. \tag{2.8}$$

Under this transformation, $D_\mu(x)\psi(x)$ and $\psi(x)$ transform in an identical manner.

The field strength tensor is then written as:

$$F_{\mu\nu}(x) = -i\,[D_\mu(x), D_\nu(x)] = \delta_\mu A_\nu(x) - \delta_\nu A_\mu(x) + i\,[A_\mu(x), A_\nu(x)]. \tag{2.9}$$

The field strength tensor inherits the transformation of the covariant derivative, since it is the commutator of two covariant derivatives:

$$F_{\mu\nu}(x) \to F'_{\mu\nu}(x) = \Omega(x) F_{\mu\nu}(x) \Omega(x)^\dagger. \tag{2.10}$$

From this parts, the gauge action can be built:

$$\mathcal{S}_\mathrm{g}[A] = \frac{1}{2g^2} \int \mathrm{d}^4x \, \mathrm{Tr}[F_{\mu\nu}(x) F_{\mu\nu}(x)]. \tag{2.11}$$

From the sum over the Lorentz indices μ, ν follows that the gauge action is a Lorentz scalar. It is also invariant under gauge transformations:

$$\mathcal{S}_\mathrm{g}[A'] = \mathcal{S}_\mathrm{g}[A]. \tag{2.12}$$

This invariance follows from Eq. (2.10), the property $\Omega(x)^\dagger = \Omega(x)^{-1}$, and the fact that the trace is invariant under cyclic permutations.

The field strength tensor can also be written in terms of its components using Eq. (2.3):

$$F^{(i)}_{\mu\nu}(x) = \delta_\mu A^{(i)}_\nu(x) - \delta_\nu A^{(i)}_\mu(x) - f_{ijk} A^{(j)}_\mu(x) A^{(k)}_\nu(x). \tag{2.13}$$

The gauge action can therefore be rewritten to:

$$\mathcal{S}_\mathrm{g}[A] = \frac{1}{4g^2} \sum_{i=1}^{8} \int \mathrm{d}^4x F^{(i)}_{\mu\nu}(x) F^{(i)}_{\mu\nu}(x). \tag{2.14}$$

The colour components of the gluon field get mixed by the quadratic term $A^{(i)}_\mu(x)$ in Eq. (2.13), leading to cubic and quartic orders of this term in the gauge action. This leads to self-interactions of the gluon, which are responsible for colour confinement.

Knowing the actions of QCD, the expectation value of an observable O can now be calculated as:

$$\langle O \rangle = \frac{1}{Z_{QCD}} \int \mathcal{D}[\psi, \bar{\psi}] \mathcal{D}[A] \; O[\psi, \bar{\psi}, A] e^{-\mathcal{S}_\mathrm{f}[\psi, \bar{\psi}, A] - \mathcal{S}_\mathrm{g}[A]}. \tag{2.15}$$

$\mathcal{D}[\psi, \bar{\psi}]$, $\mathcal{D}[A]$ are path integral measures that denote an integration over all possible field configurations, whereas Z_{QCD} denotes the partition function, as well as the normalisation of the expectation value, defined as

$$Z_{QCD} = \int \mathcal{D}[\psi, \bar{\psi}] \mathcal{D}[A] \; e^{-\mathcal{S}_\mathrm{f}[\psi, \bar{\psi}, A] - \mathcal{S}_\mathrm{g}[A]}. \tag{2.16}$$

2.2 Introducing LQCD

Next, we want to bring QCD onto the lattice. First, the 4D lattice Λ needs to be defined:

$$\Lambda = \{ n = (n_1, n_2, n_3, n_4) \,|\, n_1, n_2, n_3 = 0, 1, \cdots, N_\mathrm{s} - 1 \,;\, n_4 = 0, 1, \cdots N_\tau - 1 \}. \tag{2.17}$$

The points in space-time are separated by the lattice spacing a and labelled by the vectors $n \in \Lambda$. N_s describes the lattice extent into the spatial direction, while N_τ

is the lattice extent in the temporal direction. On these lattice points, the fermion fields are placed:

$$\psi(n), \bar{\psi}(n),\ n \in \Lambda. \tag{2.18}$$

The colour, Dirac and flavour indices are suppressed here for more clarity, since they are the same as in the continuum formulation. Also, for convenience, instead of the physical space-time point $x = an$, we label the position of the quarks on the lattice with the integer-valued 4-coordinate n.

The fermion action is discretised in the following way:

$$\mathcal{S}_{\mathrm{f}}^{0}[\psi, \bar{\psi}] = a^4 \sum_{n \in \Lambda} \bar{\psi}(n) \left(\sum_{\mu=1}^{4} \gamma_\mu \frac{\psi(n+\hat{\mu}) - \psi(n-\hat{\mu})}{2a} + m\psi(n) \right), \tag{2.19}$$

with the unit vector $\hat{\mu}$ pointing in the direction μ.

We also simply replaced the integral with a sum:

$$\int \mathrm{d}^4 x \to a^4 \sum_{n \in \Lambda}. \tag{2.20}$$

For the discretisation of the derivative there exist multiple possibilities, but the most sensible to work with in our case is the symmetric one:

$$\partial_\mu \psi(x) \to \frac{1}{2a} \left(\psi(n+\hat{\mu}) - \psi(n-\hat{\mu}) \right). \tag{2.21}$$

This derivative produces terms proportional to $\bar{\psi}(n)\psi(n+\hat{\mu})$:

$$\bar{\psi}(n)\psi(n+\hat{\mu}) \to \bar{\psi}'(n)\psi'(n+\hat{\mu}) = \bar{\psi}(n)\Omega(n)^\dagger \Omega(n+\hat{\mu})\psi(n+\hat{\mu}). \tag{2.22}$$

These terms are not gauge invariant, because the transformation $\Omega(n)$ and its hermitian conjugate $\Omega(n+\hat{\mu})^\dagger$ are not situated at the same lattice point. This can be saved by introducing the gauge fields fields $U_\mu(n)$, elements of $SU(3)$, which transform the following way:

$$U_\mu(n) \to U'_\mu(n) = \Omega(n) U_\mu(n) \Omega(n+\hat{\mu})^\dagger. \tag{2.23}$$

These gauge fields have an orientation and can therefore, for notational convenience, point in negative μ direction:

$$U_{-\mu}(n) \equiv U_\mu(n-\hat{\mu})^\dagger. \tag{2.24}$$

The gauge fields can be expressed through the algebra-valued lattice gauge fields $A_\mu(n)$:

$$U_\mu(n) = \exp(iaA_\mu(n)). \tag{2.25}$$

The object $\bar{\psi}(n)U'_\mu(n)\psi(n+\hat{\mu})$ can be formed out of fermion and gauge fields, and it is gauge invariant:

$$\bar{\psi}'(n)U'_\mu(n)\psi'(n+\hat{\mu}) = \bar{\psi}(n)\Omega(n)^\dagger U'_\mu(n)\Omega(n+\hat{\mu})\psi(n+\hat{\mu}). \tag{2.26}$$

Since the gauge fields populate the links between the lattice points n and $n+\hat{\mu}$, they are also known as link variables. Using them, it is possible to construct a gauge invariant fermion action, the so-called naive fermion action:

$$\mathcal{S}_{\mathrm{f}}^{0}[\psi,\bar{\psi},U]=a^{4}\sum_{n\in\Gamma}\bar{\psi}(n)\left(\sum_{\mu=1}^{4}\gamma_{\mu}\frac{U_{\mu}(n)\psi(n+\hat{\mu})-U_{-\mu}(n)\psi(n-\hat{\mu})}{2a}+m\psi(n)\right). \tag{2.27}$$

With the gauge links at hand, it is then possible to bring the gauge action $\mathcal{S}_{\mathrm{g}}[A]$ on the lattice. For this, one works with a closed loop of gauge links, because only these are invariant under gauge transformations. In the gauge action, the smallest non-trivial of these objects is used, the plaquette:

$$U_{\mu\nu}(n)=U_{\mu}(n)U_{\nu}(n+\hat{\mu})U_{\mu}(n+\hat{\nu})^{\dagger}U_{\nu}(n)^{\dagger}. \tag{2.28}$$

The Wilson gauge action [25] can thus be constructed as:

$$\mathcal{S}_{\mathrm{g}}[U]=\frac{2}{g^{2}}\sum_{n\in\Lambda}\sum_{\mu<\nu}\mathrm{Re}\,\mathrm{Tr}[\mathbb{1}-U_{\mu\nu}(n)]. \tag{2.29}$$

The trace in the action is taken in colour space and the sum over the Lorentz indices goes from $1\leq\mu<\nu\leq 4$. To reach the same structure as the continuum action Eq. (2.11), we included the factor $2/g^2$, which can also be expressed as $\frac{2}{g^2}=\frac{\beta}{3}$, with the so-called inverse gauge coupling $\beta=\frac{6}{g^2}$, which will play an important role in this work.

When taking $a\to 0$, the Wilson gauge action reproduces the continuum gauge action from Eq. (2.11).

2.3 Wilson Fermions

In Section 2.2, we already constructed the naive fermion action. Even though at a first glance it looks like the correct fermion action, it is not. In order to see the problem of the naive fermion action depicted in Eq. (2.27), it is brought into a compact form:

$$\mathcal{S}_{\mathrm{f}}[\psi,\bar{\psi},U]=a^{4}\sum_{n,m\in\Lambda}\sum_{a,b,\alpha,\beta}\bar{\psi}(n)_{\underset{a}{\alpha}}D(n|m)_{\underset{ab}{\alpha\beta}}\psi(m)_{\underset{b}{\beta}}, \tag{2.30}$$

where $D(n|m)_{\underset{ab}{\alpha\beta}}$ is the Dirac operator:

$$D(n|m)_{\underset{ab}{\alpha\beta}}=\sum_{\mu=1}^{4}(\gamma_{\mu})_{\alpha\beta}\frac{1}{2a}\left(U_{\mu}(n)_{ab}\delta_{n+\hat{\mu},m}-U_{\mu}(n-\hat{\mu})^{\dagger}\delta_{n-\hat{\mu},m}\right)+m_{0}\delta_{\alpha\beta}\delta_{ab}\delta_{nm}. \tag{2.31}$$

Fourier transforming this Dirac operator for free lattice fermions, i.e. $U_{\mu}(n)=\mathbb{1}$, and taking the the inverse leads to the momentum space propagator $\tilde{D}(p)^{-1}$. For massless fermions, $m=0$, it takes the following form:

$$\tilde{D}(p)^{-1}\Big|_{m=0}=\frac{-ia^{-1}\sum_{\mu}\gamma_{\mu}\sin(p_{\mu}a)}{a^{-2}\sum_{\mu}\sin(p_{\mu}a)^{2}}. \tag{2.32}$$

Taking the continuum limit of the momentum space propagator leads to the expected result:

$$\lim_{a\to 0} \tilde{D}(p)^{-1}\Big|_{m=0} = \frac{-i\sum_\mu \gamma_\mu p_\mu}{p^2}. \tag{2.33}$$

One sees directly, that the continuum momentum space propagator has its only pole, corresponding to a single fermion, at $p = (0,0,0,0)$. In contrast, the momentum space propagator on the lattice, c.f. Eq. (2.32), has additional poles whenever the components are placed at either $p_\mu = 0$ or $p_\mu = \pi/a$. This leads to 15 unwanted poles, meaning the theory has 15 unphysical fermions, also called *doublers*. Several different methods for getting rid of these doublers exist, but in this work, we will use, and therefore focus on, Wilson fermions.

To eliminate the doublers, Wilson suggested including an extra term into the momentum space Dirac propagator, which vanishes when the components take the value $p_\mu = 0$ and adds the contribution $\frac{2}{a}$ when the components are equal to $p_\mu = \pi/a$. The *Wilson term* adds to the doublers mass, leading to an overall mass of

$$m + \frac{2l}{a}, \tag{2.34}$$

with the number of momentum components l, which have the value $p_\mu = \pi/a$. Because the doublers are becoming very heavy in the continuum limit $a \to 0$, they decouple from the theory. Therefore, the unwanted poles will vanish.

The form of this Wilson term is

$$\tilde{D}(p) = m\mathbb{1} + \frac{i}{a}\sum_{\mu=1}^{4} \gamma_\mu \sin(p_\mu a) + \mathbb{1}\frac{1}{a}\sum_{\mu=1}^{4}(1-\cos(p_\mu a)). \tag{2.35}$$

For N_f fermion flavours, this leads to the following action:

$$\mathcal{S}_\mathrm{f}[\psi,\bar{\psi},U] = \sum_{f=1}^{N_\mathrm{f}} a^4 \sum_{n,m\in\Lambda} \bar{\psi}^{(f)}(n) D^{(f)}(n|m)\psi^{(f)}(m), \tag{2.36}$$

with the Dirac operator [25]

$$D^{(f)}(n|m) = \left(m_0^{(f)} + \frac{4}{a}\right)\delta_{\alpha\beta}\delta_{ab}\delta_{nm} - \frac{1}{2a}\sum_{\mu=\pm1}^{\pm4}(\mathbb{1}-\gamma_\mu)_{\alpha\beta}U_\mu(n)_{ab}\delta_{n+\hat{\mu},m}, \tag{2.37}$$

with the notation $\gamma_{-\mu} = -\gamma_\mu$ and the Wilson term in position space as the inverse Fourier transform of Eq. (2.35)

$$-a\sum_{\mu=1}^{4}\frac{U_\mu(n)_{ab}\delta_{n+\hat{\mu},m} - 2\delta_{ab}\delta n, m + U_{-\mu}(n)_{ab}\delta_{n-\hat{\mu},m}}{2a^2}. \tag{2.38}$$

Because this work is concerned with large quark masses, the quark propagator and the fermion determinant are expanded for large quark masses m:

$$D = C(\mathbb{1}-\kappa H) \text{ with } \kappa = \frac{1}{2(am+4)},\ C = m + \frac{4}{a}, \tag{2.39}$$

with κ as the *hopping parameter*, which is a real number and is used to control the bare quark mass m_0 in the Monte Carlo Simulations run for this work. All nearest neighbour terms of the Dirac operator are gathered in H, the *hopping matrix*:

$$H(n|m)^{\alpha\beta}_{ab} = \sum_{\mu=\pm1}^{\pm4} (\mathbb{1} - \gamma_\mu)_{\alpha\beta} U_\mu(n)_{ab} \delta_{n+\hat{\mu},m}. \tag{2.40}$$

Through redefining the quark fields, the constant C of the expanded Dirac operator can be absorbed:

$$\psi \to \sqrt{C}\psi,\ \bar{\psi} \to \sqrt{C}\bar{\psi}. \tag{2.41}$$

The expanded Dirac operator can therefore be rewritten to $D = \mathbb{1} - \kappa H$.

With the fermion and gauge action at hand, it is possible to calculate an observable, analogous to Eq. (2.15):

$$\langle O \rangle = \frac{1}{Z} \int \mathcal{D}[\psi, \bar{\psi}] \mathcal{D}[U]\ O[\psi, \bar{\psi}, U] e^{-\mathcal{S}_\mathrm{f}[\psi,\bar{\psi},U] - \mathcal{S}_\mathrm{g}[U]}, \tag{2.42}$$

with the partition function similar to Eq. (2.16):

$$Z = \int \mathcal{D}[\psi, \bar{\psi}] \mathcal{D}[U]\ e^{-\mathcal{S}_\mathrm{f}[\psi,\bar{\psi},U] - \mathcal{S}_\mathrm{g}[U]}. \tag{2.43}$$

Wilson fermions and symmetries

The Wilson discretisation is breaking multiple symmetries. The obviously broken symmetries are the translational and rotational symmetries, which are broken because of the lattice and are recovered when taking the continuum limit. Wilson fermions also explicitly break chiral symmetry, a symmetry associated with the following transformation:

$$\psi \to \psi' = e^{i\alpha\gamma_5}\psi,\ \bar{\psi} \to \bar{\psi}' = \bar{\psi} e^{i\alpha\gamma_5}. \tag{2.44}$$

Since the Wilson Dirac operator, c.f. Eq. (2.37), does not anticommute with γ_5, $\{\gamma_5, D\} \neq 0$, it is not invariant under chiral transformations anymore.

On the other hand, charge conjugation $\mathcal{C}$ and parity $\mathcal{P}$, which respectively transform particles into antiparticles and reflections in the Euclidean space, are conserved.

Another conserved symmetry is the γ_5-hermiticity, where the Dirac operator obeys the transformation

$$(\gamma_5 D)^\dagger = \gamma_5 D \Leftrightarrow D^\dagger = \gamma_5 D \gamma_5. \tag{2.45}$$

This symmetry is very important for Monte Carlo Simulations, since it implies a real fermion determinant, because γ_5 hermitian Dirac operators have either real eigenvalues or eigenvalues that come in complex conjugate pairs.

All of these symmetry properties of Wilson fermions are connected the *Nielsen-Ninomiya-theorem* [33, 34, 35], which states that on the lattice, it is impossible to construct a theory which is free of doublers and simultaneously preserves locality, the chiral symmetry, translational invariance and hermiticity.

2.4 Wilson and Polyakov Loops

Next, we introduce two important gauge invariant observables, the Wilson loop and the Polyakov loop, which will be important later on as our order parameter of the deconfinement phase transition. Both the Wilson and Polyakov loop are made up from link variables. It is also possible to calculate the potential between two static colour sources from both of these observables.

2.4.1 Wilson Loop

The Wilson loop $W_{\mathcal{L}}$ is constructed as the trace over four expressions forming a closed loop:

$$W_{\mathcal{L}}[U] = \mathrm{Tr}[S(\mathbf{m},\mathbf{n},n_\tau)T(\mathbf{n},n_\tau)^\dagger S(\mathbf{m},\mathbf{n},0)^\dagger T(\mathbf{m},n_\tau)]. \tag{2.46}$$

The first components of the Wilson loop are the two Wilson lines $S(\mathbf{m},\mathbf{n},n_\tau)$, $S(\mathbf{m},\mathbf{n},0)$, forming a path $\mathcal{C}_{\mathbf{m},\mathbf{n}}$ which connects the two spatial points $\mathbf{m}$ and $\mathbf{n}$, while the link variables are constrained to a single time argument:

$$S(\mathbf{m},\mathbf{n},n_\tau) = \prod_{(\mathbf{k},j)\in\mathcal{C}_{m,n}} U_j(\mathbf{k},n_\tau). \tag{2.47}$$

The two temporal transporters $T(\mathbf{n},n_\tau)$, $T(\mathbf{m},n_\tau)$ are fixed at a specified spatial position, forming straight lines of n_τ link variables.

$$T(\mathbf{n},n_\tau) = \prod_{j=0}^{n_\tau-1} U_4(\mathbf{n},j). \tag{2.48}$$

When $\mathbf{m}$ and $\mathbf{n}$ fall on the same coordinate axis, one speaks of *planar Wilson loops*, of which the Plaquette, c.f. Eq. (2.28) is the smallest member. All other Wilson loops are *nonplanar Wilson loops*.

With the gauge set to the temporal gauge, $A_4(x) = 0$, $U_4(n) = \mathbb{1}$ holds, which transforms Eq. (2.25) to

$$T(\mathbf{n},n_\tau) = \prod_{j=0}^{n_\tau-1} U_4(\mathbf{n},j) = \mathbb{1}. \tag{2.49}$$

This shortens the expression for the expectation value of the Wilson loop to

$$\langle W_{\mathcal{L}}\rangle = \langle W_{\mathcal{L}}\rangle_{\mathrm{temp}} = \langle \mathrm{Tr}[S(\mathbf{m},\mathbf{n},n_\tau)S(\mathbf{m},\mathbf{n},0)^\dagger]\rangle_{\mathrm{temp}} \tag{2.50}$$

$$= \sum_k \langle 0|\hat{S}(\mathbf{m},\mathbf{n})_{ab}|k\rangle\langle k|\hat{S}(\mathbf{m},\mathbf{n})^\dagger_{ba}|0\rangle e^{-tE_k}. \tag{2.51}$$

The states $|k\rangle$ with non-vanishing overlap can be interpreted as a static quark-antiquark pair which is located at $\mathbf{m}$ and $\mathbf{n}$, with the lowest energy $E_1 = V(r)$ describing the energy of the quark-antiquark pair at spatial quark separation $r = a|\mathbf{m}-\mathbf{n}|$. For large n_τ, or large times since $t = an_\tau$, one finds

$$\langle W_{\mathcal{L}}\rangle \propto e^{-tV(r)}\left(1+\mathcal{O}(e^{-t\Delta E})\right). \tag{2.52}$$

The corrections, containing ΔE, the difference between the potential $V(r)$, which can be calculated using non-planar Wilson loops, and the first excited energy level, are exponentially suppressed.

Using Wilson loops, it is also possible to study the recovery of the rotational invariance close to the continuum limit, as well as the mass spectrum of glueballs [31].

2.4.2 Polyakov Loop

The Polyakov loop is constructed using a Wilson loop with $n_\tau = N_\tau$, where the spatial lines with different orientation sit on top of each other. The temporal gauge can't be used because of periodic boundary conditions, but the spatial parts of the loop can be gauged to $\mathbb{1}$, leading to a separation of the Wilson loop into two disconnected temporal paths $T(\mathbf{m}, N_\tau)$, $T(\mathbf{n}, N_\tau)^\dagger$. These loops are winding, at two different positions $\mathbf{m}$ and $\mathbf{n}$ and with opposite orientation, around the temporal direction of the lattice,

Taking the trace for both loops individually makes the Polyakov loops gauge invariant:

$$L(\mathbf{m}) = \mathrm{Tr}\left[\prod_{j=0}^{N_\tau - 1} U_4(\mathbf{m}, j)\right]. \tag{2.53}$$

Analogous to the Wilson loop, not using the gauge introduced for the Polyakov loop, the expectation value of two Polyakov loops separated by $r = a|\mathbf{m} - \mathbf{n}|$ can be calculated:

$$\langle L(\mathbf{m}) L(\mathbf{n})^\dagger \rangle \propto e^{-N_\tau a V(r)} \left(1 + \mathcal{O}(e^{-N_\tau a \Delta E})\right). \tag{2.54}$$

The string tension of the Wilson loop constraints the string tension stemming from the Polyakov loop from above [36].

As a side note, for the deconfinement phase transition, the order parameter is the vacuum expectation value of the Polyakov loop, which will therefore be used throughout this work.

2.5 Continuum Limit

After discussing all the basics of lattice QCD, it is now time to discuss how to obtain a continuum value from lattice results.

In principle, lattice QCD should transform into continuum QCD when taking $a \to 0$, this is called the *naive continuum limit*. The naive continuum limit can be realised from infinitely many lattice actions, but this does not ensure reaching a theory coinciding with QCD. To reach a correct continuum limit, a critical region in the parameter space with a diverging correlation length $\hat{\xi}$ has to exist for the lattice theory, because there the memory of the underlying lattice structure is lost by the system. Therefore, for some value of the coupling g, the system has to be critical, and then a continuum limit will be reached when, for the critical coupling $g^\star$, the following equation holds:

$$\lim_{g \to g^\star} \hat{\xi}(g) = \infty. \tag{2.55}$$

This follows because physical quantities in the continuum have to be finite, and also, an implicit scale that is correlated with g had to be introduced from the outside. In terms of this scale, it is possible to measure dimensioned observables.

To determine the relationship between the scale and the coupling, consider the observable Θ with the dimension d_Θ. The corresponding observable on the lattice $\hat{\Theta}$ depends on the bare parameters, like the coupling g or the masses. These bare parameters are not directly observable physical numbers, but their values can be found via setting the scale, where observables are computed on the lattice and then identified with experimental values.

If a continuum limit exists, it implies that the quantity $\Theta(g, a)$

$$\Theta(g, a) = \left(\frac{1}{a}\right)^{d_\Theta} \hat{\Theta}(g), \tag{2.56}$$

for $a \to 0$ approaches a finite limit, provided that g is adjusted with a appropriately, making $g(a)$ approach the critical coupling $g^\star$, so that

$$\lim_{a\to 0} \Theta(g(a), a) = \Theta_{\text{phys}}. \tag{2.57}$$

Therefore, $g(a)$ could be determined from these equations for sufficiently small lattice spacings by fixing $\Theta(g, a)$ to its physical value Θ_{phys}, if the dependence of $\hat{\Theta}$ on g is known.

This process is called *running of bare parameters* and is studied via the renormalisation group. The bare parameters are functions of the lattice spacing, e.g. $g(a)$, $m(a)$, ..., meaning that their value changes when a is changing, so that physics are kept constant.

The observable $\Theta(g, a)$ has to fulfil the renormalisation group equation, formulated by Callan and Symanzik, which gives the requirements for constant physics in a differential equation

$$\left(\frac{\partial}{\partial \ln a} + \frac{\partial g}{\partial \ln a}\frac{\partial}{\partial g}\right)\Theta(g, a) = \mathcal{O}\left(\left(\frac{a}{\xi}\right)^2 \ln\left(\frac{a}{\xi}\right)\right). \tag{2.58}$$

The equation is called the *renormalisation group equation*, because it related to a semi-group of scale-changing transformations. The term

$$\beta(g) = -\frac{\partial g}{\partial \ln a}, \tag{2.59}$$

which is not the same as the inverse lattice gauge coupling β, of the equation is also known as the *renormalisation group β-function*. It determines, up to an integration constant, the dependence of the coupling g on a.

To determine the β-function, it is expanded around $g = 0$ in a power series. Using perturbation theory, the coefficients can be calculated, resulting, for $SU(N)$ and N_f massless quarks, in:

$$\begin{aligned} \beta(g) &= -\beta_0 g^3 - \beta_1 g^5 + \mathcal{O}(g^7) \\ \beta_0 &= \frac{1}{(4\pi)^2}\left(\frac{11}{3}N - \frac{2}{3}N_\text{f}\right) \\ \beta_1 &= \frac{1}{(4\pi)^4}\left(\frac{34}{3}N^2 - \frac{10}{3}NN_\text{f} - \frac{N^2-1}{N}N_\text{f}\right). \end{aligned} \tag{2.60}$$

The form of the β-function depends in the regularisation scheme, but the first two coefficients don't, as they are universal.

Combining Eq. (2.59) and Eq. (2.60), solving the resulting equation using separation of variables, leads to:

$$a(g) = \frac{1}{\Lambda_L}(\beta_0 g^2)^{-\frac{\beta_1}{2\beta_0^2}} \exp\left(-\frac{1}{2\beta_0 g^2}\right)\left(1 + \mathcal{O}(g^2)\right). \tag{2.61}$$

Here, Λ_L is an integration constant used to set the scale, its exact value depending on the regularization scheme, and therefore on the chosen actions. Through inverting Eq. (2.61), one obtains the *running coupling* $g(a)$, which shows the change g goes through with changing a, leaving the physical observables independent of the scale fixing procedure:

$$g(a)^{-2} = \beta_0 \ln(a^{-2}\Lambda_L^{-2}) + \frac{\beta_1}{\beta_0}\ln\left(\ln(a^{-2}\Lambda_L^{-2})\right) + \mathcal{O}\left(\frac{1}{\ln(a^2\Lambda_L^2)}\right). \tag{2.62}$$

For $N_\mathrm{f} < 11N_\mathrm{c}/2$, a decrease in the lattice spacing a also decreases the running coupling. Because $g = 0$ is a zero of the β-function, the lattice spacing and the running coupling will vanish together. This is also known as *asymptotic freedom*, which was already mentioned in Chapter 1 and is one of the most interesting features of QCD.

To obtain the continuum limit, one would expect to send $\beta \to \infty$ in order to arrive at $a \to 0$, but this would lead to the physical volume shrinking, $V \to 0$, because it is proportional to a^4. To deal with this, one can increase the number of lattice points in the spatial and temporal directions, i.e. $N_\mathrm{s} \to \infty$ and $N_\tau \to \infty$, which is called the *thermodynamic limit*. Ideally, the thermodynamic limit is performed before the continuum limit, but this is not possible in numerical calculations. Therefore, in practice, to reach different values of a, the physical observable is calculated for a few βs. For all the different values of a, N_s and N_τ are then chosen so that the physical extensions $L = aN_\mathrm{s}$ and $T = aN_\tau$ are kept fixed for different as. It is then possible to study the dependence on the scale a by analysing the a-dependence of the results at a fixed physical volume, extrapolating to $a \to 0$ afterwards. This analysis is called *scaling analysis* and is repeated for different physical volumes, making it possible to extrapolate to infinite physical volume.

2.6 Finite Temperature LQCD at Zero Chemical Potential

It is now also necessary to introduce temperature to lattice QCD, because until now, we only considered zero temperature lattice QCD. The starting point is the thermodynamic partition function

$$Z(T) = \mathrm{Tr}\left[e^{-\beta\hat{H}}\right], \tag{2.63}$$

with $\hat{H}$ the Hamiltonian operator and $\beta = 1/T$ the inverse temperature, which should not be mistaken for the inverse gauge coupling $\beta = \frac{6}{g^2}$.

It is possible to transform this into a path integral, using periodic and anti-periodic boundary conditions for the time extent for bosons and fermions respectively, and keeping a finite temporal extent N_τ:

$$Z(T) = \int \mathcal{D}[\psi, \bar{\psi}]\mathcal{D}[U]\; e^{-\mathcal{S}_\mathrm{E}[\psi,\bar{\psi},A]}, \tag{2.64}$$

with the Euclidean action containing an integral of the complete space extent and an integral of a finite time extent over the Euclidean Lagrangian $\mathcal{L}_\mathrm{E}$:

$$\mathcal{S}_\mathrm{E}[\psi, \bar{\psi}, A] = \int_0^\beta \mathrm{d}t \int \mathrm{d}^3x \mathcal{L}_\mathrm{E}[\psi, \bar{\psi}, A]. \tag{2.65}$$

At finite temperatures, the spatial extent aN_s should still be a far greater than the largest correlation length of the system. However, the time extent aN_τ is restricted by β:

$$\beta = \frac{1}{T} = aN_\tau. \tag{2.66}$$

This shows that zero temperature simulations are not possible, since in order to reach $T \to 0$, it would be necessary to send $N_\tau \to \infty$, which is not an option in lattice simulations. From space-time symmetry follows though, that when $N_\tau > N_\mathrm{s}$ and N_s large enough, so that the system is not sensitive to the finite volume, physics are then insensitive to the boundaries in time direction. Therefore, such a case describes a *zero temperature simulation*. In return, for finite temperature simulations, one sets $N_\tau < N_\mathrm{s}$.

In finite temperature simulations, since it has to take on discrete values, N_τ can't be used for controlling the temperature, instead, the lattice spacing a has to be used, even though it can't be controlled directly. Therefore, the lattice spacing is changed via the inverse gauge coupling β, which is related to the lattice spacing via Eq. (2.61).

It is also of importance to avoid systematic errors in the simulations, e.g. finite volume and discretisation effects. For this to be fulfilled, it has to hold that

$$a \ll \xi \ll aN_\mathrm{s}, \tag{2.67}$$

because the finite size effects need to be small and the hadron has to be resolved on the lattice. The last part follows because for $T < T_c$, the correlation length ξ is equivalent to the inverse of the smallest hadron mass m_H^{-1}. Eq. (2.67) is not easy to fulfil, since a should be very small, leading to a steep increase for N_s. Because of limited computing power, this is therefore not strictly fulfilled in our simulations.

Another matter to address is the characteristic screening length, which is described by the inverse Debye screening mass, and is, for $T > T_c$, to be considered as the mass scale, scaling with the temperature. This leads to the conditions

$$a \ll \frac{1}{T} \ll aN_\mathrm{s} \Leftrightarrow 1 \ll N_\tau \ll N_\mathrm{s}. \tag{2.68}$$

This means, that the so-called aspect ratio N_s/N_τ should be as large as possible to keep the finite volume effects small. In this work, we frequently reach aspect ratios 6, sometimes going up to 7, with a maximum aspect ratio of 10, only reached for one simulation.

2.7 Symmetries of QCD

Centre Symmetry

After introducing temperature into lattice QCD, it is now possible to discuss the symmetry relevant to our studies, the centre symmetry, which is also called the Z_3 symmetry. A centre transformation can only take place for pure gauge theory, where $m_q \to \infty$. To perform the transformation, the elements $z = e^{2\pi i l/3}$, with $l \in \{0, 1, 2\}$, of the centre group Z_3 of $SU(3)$, get multiplied with every temporal link of the given time slice $N_\tau = t_0$:

$$U_4(\mathbf{n}, t_0) \to z U_4(\mathbf{n}, t_0). \tag{2.69}$$

The gauge action is invariant under centre transformations because it is made up of products of link variables, which form trivially closed loops. Since those loops have the same amount of links in both directions and the centre elements commute with all group elements, the centre elements cancel each other out, because $zz^\dagger = \mathbb{1}$ holds.

In contrast to the gauge action, the Polyakov loop is not invariant under centre transformations, because it loops around the time direction, which means it isn't closing in a topologically trivial way. Since under a centre transformation, only one time slice is therefore multiplied with a centre element, the Polyakov loop picks up a factor z:

$$L \to zL. \tag{2.70}$$

It is to be expected that for pure gauge theory, where the centre symmetry is intact, all centre elements are populated with the same probability, leading to

$$\langle L \rangle = \frac{1}{3}\langle L + zL + z^2 L \rangle = \frac{1}{3}\left(1 + e^{2\pi i/3} + e^{-2\pi i/3}\right)\langle L \rangle = 0. \tag{2.71}$$

When the centre symmetry is broken by increasing the temperature above the critical temperature, one sector of the centre elements is getting favoured, leading to $\langle L \rangle \neq 0$, which implies that the centre symmetry gets spontaneously broken because of the finite temperature transition of quenched QCD [37]. Furthermore, this means that the Polyakov loop is an order parameter of the centre symmetry, because it is associated with its breaking. This connection will be discussed in more detail in Section 4.1.

Going back to Section 2.4, where we related the Polyakov loop to the potential between quarks and antiquarks, we can now gain an even deeper insight into the phase transition. It is possible to relate Eq. (2.54) to the free energy $F_{\bar{q}q}$ at a given temperature:

$$\langle L(\mathbf{m}) L(\mathbf{n}^\dagger) \rangle = e^{-N_\tau a F_{\bar{q}q}(a|\mathbf{m}-\mathbf{n}|)} = e^{-F_{\bar{q}q}(r)/T}. \tag{2.72}$$

This needs to be normalised, for large distances one arrives at

$$\lim_{a|\mathbf{m}-\mathbf{n}|\to\infty} \langle L(\mathbf{m}) L(\mathbf{n})^\dagger \rangle = \langle L(\mathbf{m}) \rangle \langle L(\mathbf{n})^\dagger \rangle = |\langle L \rangle|^2, \tag{2.73}$$

where the spatial position has been omitted because of the translational invariance of the Polyakov loop.

Considering static potentials like the static quark potential $V(r) = A + \frac{B}{r} + \sigma r$, with $\sigma > 0$, that grow endlessly with separation distance, it is to be expected that $|\langle L \rangle|$ vanishes. Combining this with Eq. (2.72), one can derive the existence of the following two phases:

$$\begin{aligned} \langle L \rangle = 0 &\Longleftrightarrow \text{confinement} \\ \langle L \rangle \neq 0 &\Longleftrightarrow \text{deconfinement.} \end{aligned} \tag{2.74}$$

This responds to confinement for potentials $F_{\bar{q}q} \to \infty$ and deconfinement for finite potentials $F_{\bar{q}q}$. Expressed via temperature, this means that there is confinement at small temperatures, with the system undergoing a phase transition when increasing the temperature to the critical temperature T_c [38, 39], finally leading to deconfinement with a nonvanishing Polyakov loop for temperatures above T_c. In terms of the centre symmetry, looking at Eq. (2.71), one sees that an intact centre symmetry refers to confinement and a breaking of the centre symmetry relates to deconfinement.

Measuring this phase transition is not trivial though, because strictly speaking, the centre symmetry can only break in infinite volumes. Nevertheless, it is possible to observe in finite volume simulations that the simulation lingers in one phase of the Polyakov loop before tunneling to one of the others. Using larger volumes leads to less tunneling, meaning one gets a better estimate of the true value of $\langle L \rangle$, but even then the systematic error stemming from the tunneling is not under control. Therefore, one usually uses $\langle |L| \rangle$ instead of $\langle L \rangle$, because both are equivalent in the infinite volume limit.

An inclusion of quark masses, or dynamical fermions, also breaks the centre symmetry explicitly. This can be seen with Wilson fermions, where the fermion action also contains Polyakov loops, rendering the whole fermion action not invariant under the centre symmetry. Therefore, the Polyakov loop cannot be used anymore as a true order parameter, but its distribution may still be used to study the deconfinement phase transition. Also, the inclusion of dynamical fermions can be interpreted as a symmetry breaking field, an observation later used in Section 5.3.1.

Chiral Symmetry

Another important symmetry of QCD is the chiral symmetry, which is located at light quark masses, but we will discuss this symmetry very briefly, since it is not really relevant for this work concerned with heavy quarks. Furthermore, because of the Nielsen-Ninomiya theorem, chiral symmetry is not realised for ordinary Wilson fermions, making it even less relevant for us.

The chiral condensate $\langle \bar{\psi}\psi \rangle$ is the order parameter of the chiral symmetry, where $\langle \bar{\psi}\psi \rangle = 0$ indicates its breaking and $\langle \bar{\psi}\psi \rangle \neq 0$ that the chiral symmetry is intact.

One way to realise the chiral symmetry on the lattice is to use Ginsparg-Wilson fermions instead. One starts from the symmetry of the massless fermion action

$$SU(N_f)_L \times SU(N_f)_R \times U(1)_V \times U(1)_A. \tag{2.75}$$

The noninvariance of the fermion integration measure breaks the axial symmetry $U(1)_A$, which is also called the axial anomaly. A spontaneous breaking of the chiral

symmetry leads to Goldstone bosons. In QCD these are the very light pions, which have a mass because the chiral symmetry is always explicitly broken by the small masses of the up- and down-quark.

Chapter 3

Numerical Methods and Algorithms

This chapter describes the numerical aspects of this work, giving a short summary of the most important algorithms, as well as an introduction of the software used in the simulations and a discussion about the details of the data analysis. It is mostly based on [22].

3.1 Lattice Simulations via Hybrid Monte Carlo

In lattice QCD simulations, one usually wants to evaluate observables and a corresponding error, oftentimes, like in this work, using a *Hybrid Monte Carlo (HMC) algorithm* [40] for the simulations. Since QCD observables stem from path integrals, they first need to be expressed in a way suitable for simulations. Therefore, we first take a look at how the expectation value of an observable $\langle O(x) \rangle$ is expressed generally for the purpose of Monte Carlo simulations:

$$\langle O \rangle = \frac{\int \mathcal{D}x \; O(x) e^{-\mathcal{S}(x)}}{\int \mathcal{D}x \; e^{-\mathcal{S}(x)}}, \tag{3.1}$$

with the Boltzmann factor $e^{-\mathcal{S}(x)}$, which is later used as probability weight. An average over N values provides an approximation for this:

$$\langle O \rangle = \lim_{N \to \infty} \frac{1}{N} \sum_{n=1}^{N} O[U_n]. \tag{3.2}$$

The sampling of each U_n is done in accordance with the probability distribution density

$$dP(U) = \frac{e^{-\mathcal{S}[U]} \mathcal{D}[U]}{\int \mathcal{D}[U] \; e^{-\mathcal{S}[U]}}. \tag{3.3}$$

Such configurations U_n can be found via *Markov chains*, a process where a new configuration is generated from the previous configuration. The configurations are then labelled in order by the index n. The elements of a Markov chain are drawn in a *Markov process*, with the Boltzmann factor $e^{-\mathcal{S}(x)}$ as a weight for the probability with which the next element in the Markov chain is drawn. In this thesis, we create new configurations using an HMC algorithm, which is built using multiple other algorithms.

Metropolis algorithm

The first algorithm we will discuss is the *Metropolis algorithm* [41], which can be used to obtain a set of pseudo-randomly distributed configurations via a Markov chain.

To achieve this, one starts with an arbitrary configuration $U_\mu(n)$, then generates the potential updated configuration $U_\mu(n)'$ via an update step, creating a path of configurations until a sufficient number of configurations is reached. The important step for the Metropolis algorithm, the *Metropolis step*, is now to ensure the proper distribution. The new configuration $U_\mu(n)'$ only gets accepted if the change ΔS of the action resulting from the update step fulfils $e^{-\Delta S} > \eta$, where η is a random number, drawn from a uniform distribution with range 0 to 1. If the condition is not fulfilled, the update step is repeated.

The initial configuration can be chosen from *hot* or *cold*. A cold start means that the initial configuration only contains unit matrices, with a hot start, the initial configuration is filled with random matrices. These first trajectories are almost always unusual and should be discarded. This process is called *thermalisation* and should only end when the observables measured at the configurations start to fluctuate around their mean, indicating that the thermalisation is completed.

Heat Bath algorithm

The next algorithm we want to discuss is the *Heat Bath algorithm* [41, 42, 43]. This algorithm is used for pure gauge theory and follows the concept of the Metropolis algorithm. The update step is performed according to an exact algorithm for $SU(2)$, which updates every link efficiently according to its neighbours, because for $SU(2)$, summing over two elements leads to a matrix which is proportional to another $SU(2)$ matrix. It is also possible to use the Heat Bath algorithm for $SU(3)$, because $SU(3)$ links can be reduced to three $SU(2)$ subgroups, which then can be updated the usual way and are afterwards extended back to $SU(3)$.

Path Integral in Lattice Simulations

Another important piece for constructing an HMC algorithm for lattice QCD is the expression of its path integral in a way that is usable in simulations. We start with the path integral Eq. (2.42)

$$\langle O \rangle = \frac{1}{Z} \int \mathcal{D}[\psi, \bar{\psi}] \mathcal{D}[U] \; O[\psi, \bar{\psi}, U] e^{-\mathcal{S}[U,\psi,\bar{\psi}]}. \tag{3.4}$$

Integrating out the fermion fields gives the determinant of the fermion matrix D, leaving only an integral over all gauge configurations:

$$\langle O \rangle = \frac{1}{Z} \int \mathcal{D}U \; O[\psi, \bar{\psi}, U] \det(M[U]) e^{-\mathcal{S}_\mathrm{g}[U]}, \tag{3.5}$$

with $M = DD^\dagger$. Using the relation $\det(M) = e^{\mathrm{Tr}(\ln(M))}$, this can be rewritten to:

$$\langle O \rangle = \frac{1}{Z} \int \mathcal{D}U \; O[\psi, \bar{\psi}, U] e^{-\mathcal{S}_\mathrm{eff}[U]}; \qquad \mathcal{S}_\mathrm{eff}[U] = \mathcal{S}_\mathrm{g}[U] - \mathrm{Tr}(\ln(M)). \tag{3.6}$$

The action can then be used as a probability distribution for sampling the gauge fields:

$$P[U] = \frac{1}{Z} e^{-\mathcal{S}_{\mathrm{g}}[U]} \det(M[U]). \tag{3.7}$$

This means though, that the fermion determinant must be real and non-negative, which can be satisfied through the γ_5 hermiticity, combined with using degenerate masses.

The fermion can also be replaced by an integral over pseudo-fermion fields ϕ:

$$\det(M[U]) \sim \int \mathcal{D}[\phi^\dagger]\mathcal{D}[\phi]\; e^{-\phi^\dagger M^{-1}[U]\phi}. \tag{3.8}$$

Considering $N_{\mathrm{f}} = 2$, the effective action can therefore also be expressed as

$$\mathcal{S}_{\mathrm{eff}}[U, \phi] = \mathcal{S}_{\mathrm{g}}[U] + \phi^\dagger M^{-1}[U]\phi. \tag{3.9}$$

Molecular dynamics algorithm

For the Hybrid Monte Carlo algorithm, now only the crucial *Molecular Dynamics* step is missing, which is the update step using a Markov process to generate the configurations. To use the Molecular Dynamics step within the HMC, one embeds the effective action into a fictitious molecular dynamics system where the chain of the configurations follows from an evolution of the system in the fictitious time τ. The development of the fields U with τ is then described by Hamiltonian dynamics, where the Hamiltonian of the system, with the conjugate momenta $\pi(\tau)$:

$$H(U, \pi) = \frac{\pi^2}{2} + \mathcal{S}_{\mathrm{eff}}[U]. \tag{3.10}$$

Each step, the system is evolved over time τ according to the Hamilton equation of motion:

$$\dot{\pi} = -\partial\mathcal{S}_{\mathrm{eff}}/\partial U \equiv F; \;\; \dot{U} = \pi, \tag{3.11}$$

with F as a force. The numerical evolution of these equations also introduces a step size $\Delta\tau$, with an error $\mathcal{O}((\Delta\tau)^2)$ for a simple linear evolution. This can be dealt with by the introduction of a corrective step, which is used in the Hybrid Monte Carlo algorithm.

Hybrid Monte Carlo algorithm

The principle of the HMC algorithm is to first construct a new configuration along a trajectory, a chain of small steps in the molecular dynamics evolution, and then to decide via a Metropolis step if the new configuration is to be accepted. It is furthermore important to note that detailed balance needs to be ensured, i.e. the integration method must preserve the integration measure and the trajectory must be reversible. Multiple methods exist for integrating the molecular dynamics equations while obeying detailed balance, examples are the leapfrog integration scheme or the Omelyan-Mryglod-Folk integrator. The number of integration steps I controls the precision of the integration. Also, the conjugate momenta $\pi(t)$ and fermion fields ϕ are chosen randomly from a Gaussian distribution.

Overall, one HMC step consists of:

1. Momentum refreshment heatbath: From configuration U_n, generate set of conjugate momenta π from Gaussian distribution $P_G(\pi) \sim e^{-\pi^2/2}$

2. Pseudofermion heatbath: Generate pseudofermion field ϕ from Gaussian distribution $P(\chi) = e^{-\chi^\dagger \chi}$

3. Perform molecular dynamics evolution

4. Metropolis acceptance test with acceptance probability $P_{acc} = \min(1, e^{-\delta H})$

An important parameter of such simulations is the acceptance rate, which is the ratio of accepted configurations over the number of acceptance tests performed and can be varied through the number of molecular dynamics steps and the integration time τ. A low acceptance rate leads to longer simulation time, since more trajectories get rejected, but if the acceptance rate is too high, the space might not be sampled sufficiently. Typically, the acceptance rate is tuned to lie between 60% and 85%, to avoid both issues as well as possible.

3.2 Data Analysis

After obtaining data from simulations, it needs to be analysed. The following section will therefore describe the most important techniques we used for the data analysis.

3.2.1 Error Analysis

Variance and Statistical Analysis

From the HMC simulations, we have $(o_1, o_2, \ldots, o_N)$ values of our observable in form of a Markov sequence, which each correspond to a random variable O_i. The expectation value and variances for all of these random variables are identical:

$$\langle O_i \rangle = \langle O \rangle, \tag{3.12}$$

$$\sigma^2 = \langle (O_i - \langle O_i \rangle)^2 \rangle. \tag{3.13}$$

The unbiased estimator, so an estimator whose expected value is equal to the true value of the parameter, for this variable is:

$$\hat{O} = \frac{1}{N} \sum_{i=1}^{N} O_i, \quad \hat{\sigma}^2 = \frac{1}{N-1} \sum_{i=1}^{N} (O_i - \hat{O})^2. \tag{3.14}$$

For uncorrelated measurements, the standard deviation $\tilde{\sigma}$ is written as:

$$\tilde{\sigma}^2 = \frac{1}{N} \sigma^2. \tag{3.15}$$

This shows the decrease of the statistical error by $\sqrt{N}$.

Autocorrelation

Because our data stems from a time series, it has a high chance of being correlated, meaning that Eq. (3.15) does not hold anymore. This *autocorrelation* can be quantified via the autocorrelation function

$$C_O(O_i, O_{i+t}) = \langle O_i O_{i+t} \rangle - \langle O_i \rangle \langle O_{i+t} \rangle. \tag{3.16}$$

This only depends on the time separation t, so $C_O(t) = C_O(O_i, O_{i+t})$, if the Markov chain is in equilibrium. From this, one can also build the correlation function

$$\Gamma_O(t) \equiv \frac{C_O(t)}{C_O(0)}, \tag{3.17}$$

with $C_O(0) = \sigma^2$. This leads to the integrated autocorrelation time

$$\tau_{\text{int}} = \frac{1}{2} + \sum_{t=1}^{N} \Gamma_O(t), \tag{3.18}$$

which can be used to rewrite the variance as

$$\tilde{\sigma}^2 = \sigma^2 \frac{2\tau_{\text{int}}}{N}. \tag{3.19}$$

This decreases the number of measurements because out of N values, the number of effectively independent data is:

$$N_{\text{indep}} = \frac{N}{2\tau_{\text{int}}}, \tag{3.20}$$

which is also called the number of independent events.

The variance is then

$$\tilde{\sigma}^2_{\text{corrected}} = 2\tau_{\text{int}} \tilde{\sigma}^2, \tag{3.21}$$

In this work, we calculate the autocorrelation time τ_{int} with the Γ-method, for more details refer to [44].

An important effect related to the autocorrelation time is *critical slowing down*. The updating algorithm and the parameters of the lattice system influence the autocorrelation time

$$\tau_{\text{int}} \sim (\xi_O)^z, \tag{3.22}$$

with z depending on the updating algorithm and ξ_O the correlation length of the observable O, which is also the longest correlation length in the system. On a finite lattice, one has $\xi \leq L$, but the correlation length is also growing at critical points, which leads to the computational cost growing like $\sim L^z$. This is the effect which is called critical slowing down.

Techniques for the Evaluation of Correlated Datasets

When dealing with correlated data, it is important to transform it into uncorrelated data, which can be done via *binning*, also called *blocking*, a process where one divides the data into sub-blocks of size K. In general, one then computes the mean values of the blocks, using them as new variables O_i, which would lead to a decrease of $1/K$ in the variance if the original data were independent. This is repeated for different values of K, until the decreasing behaviour can be observed, indicating K to be large enough to consider the data uncorrelated.

In our case, we perform the binning using the autocorrelation time τ_{int}, dividing the data in bins of approximately $2\tau_{\text{int}}$. In most cases, N data is not going to be divided by $2\tau_{\text{int}}$ without a remainder. The bin size should therefore be chosen in a way that it divides N with a small remainder, meaning that the bin size can be chosen smaller or larger than $2\tau_{\text{int}}$. This leads to an under- or overestimation of the error, with an overestimation being preferred. This binned data can then be analysed with methods like the statistical bootstrap or the jackknife.

In the *statistical bootstrap*, one takes a set of N data and creates samples from this by randomly drawing N data of the original dataset, whereby the same data can be drawn multiple times. This method is very cost-efficient, because one reuses the same data over and over in the creation of new sets. After obtaining K sets of N data, the desired observable O is calculated for each of these sets, leading to the observables O_k with $k = 1, \ldots, K$. From this, one can calculate the biased estimators

$$\tilde{O} \equiv \frac{1}{K}\sum_{k=1}^{K} O_k, \quad \sigma^2 \equiv \frac{1}{K}\sum_{k=1}^{K}(O_k - \tilde{O})^2. \tag{3.23}$$

Because this estimator is not unbiased, $\tilde{O} \neq \hat{O}$ for finite K and the bias gives an idea about the distance to the true $\langle O \rangle$.

Another method to analyse an observable is the *jackknife*. One starts again with a dataset of size N, with $\hat{O}$ the observable calculated on the original set. From the original dataset, construct N subsets by removing the nth entry, $n = 1, \ldots, N$, from the original dataset, and calculate the observable O_n for each set, with the error:

$$\sigma^2 \equiv \frac{N-1}{N}\sum_{n-1}^{N}(O_n - \hat{O})^2. \tag{3.24}$$

The bias can be calculated via

$$\tilde{O} \equiv \frac{1}{N}\sum_{n=1}^{N} O_n, \tag{3.25}$$

leading to $\hat{O} - (N-1)(\tilde{O} - \hat{O})$ as the unbiased estimator of $\langle O \rangle$.

It is also possible to combine the statistical bootstrap and the jackknife. To do this, first, the data gets organised in blocks, and then subsets are constructed by the removal of blocks instead of single values. This is actually a necessity when working with binned data, since in that case it is already organised in blocks.

This can also be generalised to composite observables. The observables are calculated on the same data, where the same measurements are discarded for all observables. If autocorrelation is to be considered, the binning has to have the same size for each observable, so it is important to always use the largest bin size to then evaluate the quantities on the same sample. When all observables are calculated, one then builds up the original observable out of the calculated ones. An example for this are the skewness and kurtosis, to be discussed in more detail in Section 5.2.1:

$$B_n(O) = \frac{\langle (O - \langle O \rangle)^n \rangle}{\langle (O - \langle O \rangle)^2 \rangle^{n/2}}. \tag{3.26}$$

3.2.2 Reweighting

From our simulations, since the simulation costs are so high, we only get very few data points of the inverse gauge coupling β, which are not incredibly close to each other, because we have to scan a wider area to include the phase transition in the parameter space of the simulations. To find β_c, those few simulated β values are not enough though, they only give a very rough picture about the location of the phase transition. Therefore, we use *reweighting*, a technique which makes it possible to get a good interpolation between Monte Carlo results at different couplings. This means we can use it to interpolate between our measurements that were done at different β values, as long as the distance between those is not too far. For a more in depth explanation than we are going to give in this work, refer to [45].

Reweighting was introduced by Ferrenberg and Swendsen [46, 47]. The first reweighting technique was the *single histogram reweighting*, which can only be used when one has one point in parameter space. In general we have multiple points though, therefore we use *multiple histogram reweighting*, also called *Ferrenberg-Swendsen reweighting* or just reweighting. With this technique it is possible to reweight multiple points in parameter space.

To explain reweighting, the partition function is expressed via an integration over all possible values for the systems total energy:

$$\begin{aligned} Z(\kappa) \equiv \int \mathcal{D}[\Phi]\, e^{-\kappa \mathcal{S}[\Phi]} &= \int \mathrm{d}E \int \mathcal{D}[\Phi]\, \delta(E - \mathcal{S}[\Phi]) e^{-\kappa \mathcal{S}[\Phi]} \\ &= \int \mathrm{d}E \rho(E) e^{-\kappa E} \quad \text{with} \quad \rho(E) = \int \mathcal{D}[\Phi]\, \delta(E - \mathcal{S}[\Phi]). \end{aligned} \tag{3.27}$$

This can be generalised to multi-histogram reweighting by generating the energy distribution density $\rho(E)$ from simulation results at multiple couplings. It is possible, for any value of κ, to calculate $Z(\kappa)$ and its derivatives if $\rho(E)$ is obtained and when one knows the energy distribution to an arbitrary precision. Because this can not be achieved with simulations, the overlap of the distributions of different couplings is crucial for computing Z.

With β the inverse gauge coupling, one can see from

$$\begin{aligned}&\left\langle \frac{e^{-\mathcal{S}_{\mathrm{g}}[\beta',U]}\det[D(\mu',U)]}{e^{-\mathcal{S}_{\mathrm{g}}[\beta,U]}\det[D(\mu,U)]}\right\rangle_{\beta,\mu} \\ =&\frac{1}{Z(\beta,\mu)}\int \mathcal{D}[U]\, e^{-\mathcal{S}_{\mathrm{g}}[\beta',U]}\det[D(\mu',U)] = \frac{Z(\beta',\mu')}{Z(\beta,\mu)},\end{aligned} \tag{3.28}$$

that it is possible to determine $Z(\beta',\mu')$ from results evaluated at β and μ with the reweighting factor chosen as the deviation of $\det[D(\mu)]$ from $\det[D(0)]$:

$$Z(\beta',\mu') = Z(\beta,\mu)\left\langle \frac{e^{-\mathcal{S}_{\mathrm{g}}[\beta',U]}\det[D(\mu',U)]}{e^{-\mathcal{S}_{\mathrm{g}}[\beta,U]}\det[D(\mu,U)]}\right\rangle_{\beta,\mu}. \tag{3.29}$$

An observable can be then calculated as

$$\langle O\rangle_{(\beta,\kappa,\mu)} = \frac{\left\langle O e^{\mathcal{S}'_{\mathrm{g}}-\mathcal{S}_{\mathrm{g}}}\frac{\det D(\kappa,\mu)}{\det D(\kappa',\mu')}\right\rangle_{(\beta',\kappa',\mu')}}{\left\langle e^{\mathcal{S}'_{\mathrm{g}}-\mathcal{S}_{\mathrm{g}}}\frac{\det D(\kappa,\mu)}{\det D(\kappa',\mu')}\right\rangle_{(\beta',\kappa',\mu')}}. \tag{3.30}$$

The observable O at κ,β,μ is therefore now expressed via the ensemble at κ',β',μ'. An important part of the reweighting process is ensuring that the overlap between the two ensembles is large enough, because the statistical reliabilty gets lesser with a smaller overlap.

In our case, the determinant vanishes, leaving only $e^{\mathcal{S}'_{\mathrm{g}}-\mathcal{S}_{\mathrm{g}}}$ in the formula, because we have $\mu = 0$ and we reweight at a single κ, so $\kappa = \kappa'$, therefore we only reweight for β and we need to run simulations around β_c in order to find the phase transition.

Reweighting in Practice

Here, we want to discuss how to perform reweighting in practice, using the multiple histogram approach, and how to get an error on the reweighted observable.

For multiple histogram reweighting, we will need simulation results at not too far from each other parameters $\{\beta_i\}$ to interpolate between. To begin, one has simulation data at different $\{\beta_i\}$, where an observable was measured at every trajectory, leading to n measurements. In the following, these measurements will be identified by the indices i,j,k. $E_s(\beta_i) = \mathcal{S}_{\mathrm{g}}/\beta$ is the β-independent conjugated quantity to β.

The partition function at every β_k that was simulated is then given as

$$Z(\beta_k) = \sum_{i,s}\frac{1}{\sum_j n_j Z^{-1}(\beta_j)e^{(\beta_k-\beta_j)E_s(\beta_i)}}, \tag{3.31}$$

from which also follows that

$$Z(\beta) = \sum_{i,s}\frac{1}{\sum_j n_j Z^{-1}(\beta_j)e^{(\beta-\beta_j)E_s(\beta_i)}}. \tag{3.32}$$

The value of the observable at the reweighed β is then described through

$$\langle O(\beta)\rangle = \frac{1}{Z(\beta)} \sum_{i,s} \frac{O_s(\beta_i)}{\sum_j n_j Z^{-1}(\beta_j) e^{(\beta-\beta_j)E_s(\beta_i)}}. \tag{3.33}$$

Since it is not possible to get the distribution of O at the reweighted β, the standard methods for error calculation can't be used, but it is still possible to use the statistical bootstrap and jackknife.

When using the statistical bootstrap, the data is not binned beforehand and the autocorrelation, which depends on the observable and β, gets removed during the resampling procedure. For the observable $O(\beta_i)$ one first calculates the bin size and then randomly selects a single data point per bin and uses this uncorrelated set of data in the reweighting routine, obtaining N_{boot} values of $O^B(\beta)$ from which an error can be calculated.

Using the jackknife, one needs to decorrelate the data via binning. One then always leaves out one entry from bulk of all datasets to obtain $O_i^K(\beta)$, for every data point i over all datasets.

The last concept to discuss for reweighting is the overlap of the histograms, which we already mentioned earlier. For reweighting to work, the simulation parameters

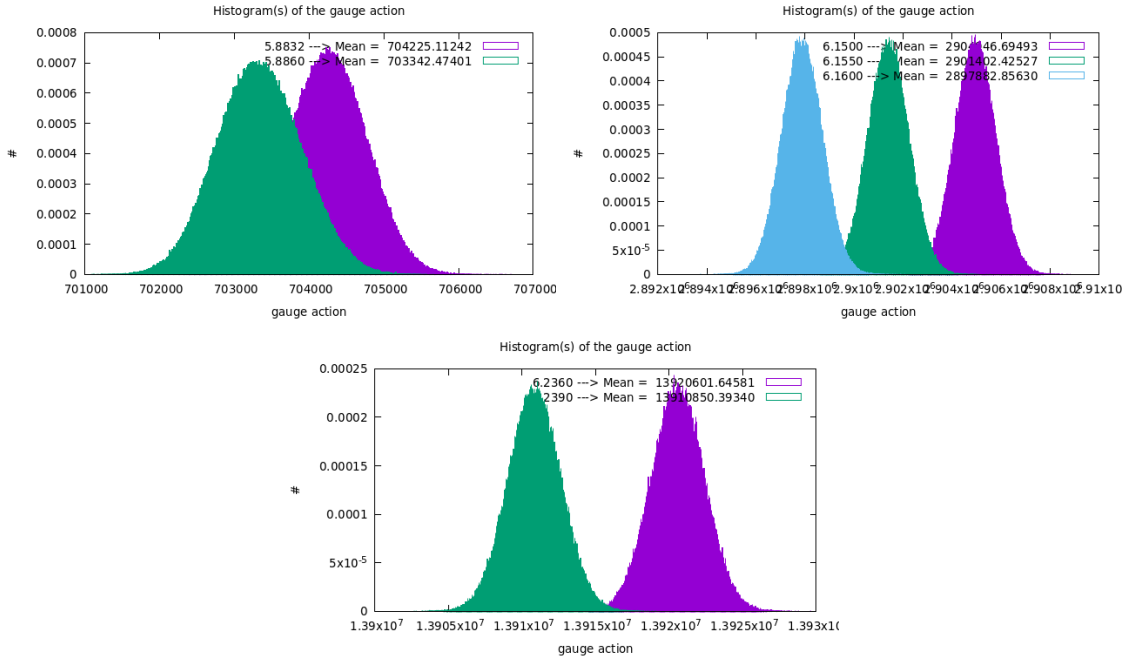

Figure 3.1: A few examples of histograms with different amount of overlap generated by a script used in our analysis. The left histogram at $N_\tau = 6$, $N_\mathrm{s} = 36$, $\kappa = 0.085$ has the most overlap, the difference between the simulated β values is 0.0028. The right histogram at $N_\tau = 10$, $N_\mathrm{s} = 50$, $\kappa = 0.12$ has already less overlap, the difference between the simulated β values is 0.0050. The lower, middle histogram at $N_\tau = 12$, $N_\mathrm{s} = 80$, $\kappa = 0.13$ has almost no overlap, the difference between the simulated β values is 0.0030. This shows, that the amount of overlap depends not only on the distance between the β values at which we reweight, but also on the other parameters N_τ, N_s, κ.

have to be close enough to each other to have a certain overlap between the different values of the parameters of the generated ensembles. The histograms for every simulated β of $P = \mathcal{S}_\mathrm{g}/\beta$ can be plotted together, making it possible to graphically check the amount of overlap, an example can be found in Figure 3.1. On the left, the histograms overlap a good amount, but when moving to the right, the overlap gets lesser. Since the accuracy of the interpolation decreases with decreasing overlap, it is important to make sure that the simulations take place at β values that are close enough to each other. This gets more crucial with increasing volumes, since the overlap is decreasing with increasing N_s, even if all other parameters are identical, because the distribution $\mathcal{S}_\mathrm{g}/\beta$ approaches a δ-function when going to infinite volume.

3.2.3 Pion Masses and Scale Setting

For our analysis, we will also need the pion mass and the lattice spacing, therefore we need to perform a scale setting procedure and collect correlators to calculate the pion mass using the Wilson flow. These two topics are combined into one chapter, because they use the same configurations obtained via zero temperature simulations, which need to be run separately from the other simulations.

But before going into the details of the simulations, we want to discuss the theory behind determining hadron masses, also called *hadron spectroscopy*. First, the hadron interpolators $O, \bar{O}$ need to be identified, so that particle states can be annihilated and created via the Hilbert space operators $\hat{O}, \hat{O}^\dagger$. The meson correlators are then written as

$$\langle O(n_t)\bar{O}(0)\rangle, \tag{3.34}$$

with n_t between $0 \leq n_t \leq N_\tau$. The pion has the form

$$O_{\pi^0}(n) = \frac{1}{\sqrt{2}}(\bar{u}(n)\gamma_5 u(n) - \bar{d}(n)\gamma_5 d(n)), \tag{3.35}$$

with u and d denoting the up and down quark respectively. This leads to the correlator

$$\begin{aligned}\langle O_\pi(n)\bar{O}_\pi(m)\rangle_F &= -\operatorname{Tr}\left[(D^{-1}(n|m))^\dagger\gamma_5^2 D^{-1}(n|m)\gamma_5^2\right] \\ &= \sum_{\beta_0,b_0}\left(-\sum_{\alpha,a}|D^{-1}(n|0)_{\substack{\alpha\beta_0\\ ab_0}}|^2\right),\end{aligned} \tag{3.36}$$

where the index F denotes that the expectation value is the fermionic expectation value which factorizes like $\langle\cdots\rangle_F = \langle\cdots\rangle_u\langle\cdots\rangle_d$ regarding the flavours. In the last step, $\gamma_5 = \mathbb{1}$ was inserted and the point source at $m = m_0 = 0$ was used.

Another component needed is the expression for the expectation value of an observable:

$$\begin{aligned}&\langle O_2(n_t)O_1(0)\rangle = \\ &\frac{1}{Z}\int \mathcal{D}[\psi,\bar{\psi}]\mathcal{D}U\, e^{\mathcal{S}_\mathrm{f}[\psi,\bar{\psi},U]-\mathcal{S}_\mathrm{g}[U]}O_2[\psi(n_t),\bar{\psi}(n_t),U(n_t)]O_1[\psi(0),\bar{\psi}(0),U(0)].\end{aligned} \tag{3.37}$$

In the zero temperature limit and using the above equation, the correlator can be rewritten as

$$\lim_{N_\tau \to \infty} \langle \tilde{O}(\mathbf{0}, n_t) \bar{O}(\mathbf{0}, 0) \rangle = Z^{-1} \operatorname{Tr} \left[e^{-(N_\tau - n_t) a \hat{H}} \hat{O} e^{-n_t a \hat{H}} \hat{O}^\dagger \right], \tag{3.38}$$

which can also be written as

$$C(n_t) \equiv \lim_{N_\tau \to \infty} \langle \tilde{O}(\mathbf{0}, n_t) \bar{O}(\mathbf{0}, 0) \rangle = \sum_n |\langle 0 | \hat{O} | n \rangle|^2 e^{-a n_t E_n}. \tag{3.39}$$

The effective mass is then defined as

$$m_{eff}(n_t + \frac{1}{2}) = \ln \frac{C(n_t)}{C(n_t + 1)}. \tag{3.40}$$

The effective mass becomes constant when $C(n_t)$ is dominated by the ground state energy, making it possible to read off the effective mass at the plateau at $m_{eff} = E_0$.

Now, let's discuss the process of finding the pion mass as it is done in our work, which was implemented in [48]. Since we simulate at zero temperature, we choose $N_\tau = 32$ and $N_\mathrm{s} = 16$ to satisfy $N_\tau > N_\mathrm{s}$, as was discussed in Section 2.6. The parameter κ is the same as for the simulation that we want the additional information on, and $\beta = \beta_c$ of this simulation. On the data received from these simulations, eight quark correlators per configuration are calculated, all at random positions for the source so the fluctuations can average out. The pion mass in lattice units is then calculated using the inverter of CL²QCD and a script that extracts the mass out of the inverter results. Afterwards, one can plot Eq. (3.40), and from the plateau, the effective mass can be extracted.

It is also necessary to perform the scale setting procedure to get the pion mass in physical units. The technique used in this work is the *Wilson flow* [49], with the w_0 scale from [50]:

$$w_0 = 0.1775(18)\mathrm{fm}. \tag{3.41}$$

To set the scale, $(w_0/a)^{latt}$ is calculated on the lattice, with a calculated via:

$$a = \frac{w_0}{(w_0/a)^{latt}}. \tag{3.42}$$

The error is calculated via error propagation.

3.3 LQCD Softwares

In this section, we want to give a quick overview of the code bases used in this work.

CL²QCD

CL²QCD [51] is a simulation code for lattice QCD, its development started in about 2011 in the working group of Owe Philipsen, with version 1.0 released in 2018. The code performs Monte Carlo simulations and was used for the majority of simulations in this work. For more detailed information about the code, its structure and

performance, have a look at [52, 53, 54, 55]. CL^{2}QCD is based on OpenCL, which allows the code to run on CPUs and also on GPUs. The inclusion of CPUs is useful, because they are more widely available, but the option to run on GPUs is a useful feature for lattice QCD simulations because they are mostly limited by memory bandwidth, while GPUs have a high memory bandwidth. Also, lattice QCD functions are local, making them well-suited for parallel computing.

CL^{2}QCD has five executables [51]:

- *su3heatbath*: Heatbath algorithm for $SU(3)$ Pure Gauge Theory, creates gauge field configurations
- *hmc*: Hybrid Monte Carlo algorithm for $N_\mathrm{f} = 2$ (Twisted Mass) Wilson fermions, creates gauge field configurations
- *rhmc*: Rational Hybrid Monte Carlo algorithm for staggered fermions, creates gauge field configurations
- *inverter*: Uses previously created gauge field configurations to measure fermion observables
- *gaugeobservable*: Uses previously created gauge field configurations to measure gauge observables

In this thesis, the gauge configurations were produced with the *hmc*, and the *inverter* was used in the process of obtaining the pion mass. The simulations using CL^{2}QCD were mainly run on the cluster L-CSC at GSI at Darmstadt [56] on AMD GPUs. Some of the older simulations used were run on the LOEWE-CSC cluster from Frankfurt [57], which was decommissioned in 2019 and also used AMD cards. A handful of pion mass simulations were performed at the Goethe-HLR cluster in Frankfurt, the successor of LOEWE-CSC, where the simulations also ran on AMD GPU cards.

openQCD-FASTSUM

Since in the beginnings of the Goethe-HLR cluster only Intel CPUs were available, we wanted to use a code optimised to run on CPUs instead of CL^{2}QCD, because even though it can run on CPUs, it is not optimised for them. We therefore decided to use the well-known code openQCD, [58] or rather openQCD-FASTSUM [59], an extension build on openQCD 1.6. openQCD was developed by Martin Lüscher and Stefan Schaefer, also containing contributions by other people. Jonas Rylund Glesaaen and Benjamin Jäger developed openQCD-FASTSUM.

In principle, openQCD-FASTSUM supports anisotropic actions and stout smearings, features we did not need, we rather used it because it has the Polyakov loop included, a feature not present in openQCD 1.6.

The code contains a multitude of features [60, 61]:

- For the molecular dynamics step, the user can choose from leapfrog, 2nd order Omelyan-Mryglod-Folk (OMF) and 4th order OMF elementary integrators, which can be nested in any combination

- For twisted mass fermions, for any number of factors, twisted-mass Hasenbusch frequency splitting can be used with or without even-odd preconditioning
- Reweighting of the twisted-mass determinant is possible
- For the molecular dynamics trajectories, a chronological solver and deflation acceleration can be used
- Every pseudo-fermion action and each force component can use its own, particularly configured solver (CGNE, MSCG, SAP+GCR, deflated SAP+GCR)

There are also different simulation and measurement programs, which all parallelise in 0,1,2,3 or 4 dimensions, [62]:

- *qcd1*: Simulates QCD with a Hybrid Monte Carlo algorithm
- *ym1*: Simulates $SU(3)$ (Pure) Gauge Theory using a Hybrid Monte Carlo program
- *ms1*: Reweighting factors can be measured
- *ms2*: The spectral range of the hermitian Dirac operator can be calculated
- *ms3*: Use for the calculation of Wilson-flow observables
- *ms4*: Quark propagators can be calculated

BaHaMAS

All our simulations were run with the help of BaHaMAS (**Ba**sh **Ha**ndler to **M**onitor and **A**dministrate **S**imulations) [63, 64], which is a tool for monitoring and administering the dozens of simulations run in this group. It is a command-line operated bash program operating on a defined folder structure containing information about the simulation parameters κ, N_τ and N_s, which is optimised for the use with CL^{2}QCD and openQCD-FASTSUM and furthermore supports the use of slurm, a job scheduler used on many computer clusters.

One of the main features of BaHaMAS is the administration and submission of jobs, either to thermalise from cold or an existing configuration, starting a new job from a thermalised configuration or continuing any of these jobs. For this feature to work, the *betas* file has to be filled out, containing information about the β values to run, their seeds, the number of trajectories to be achieved, and further information like the estimated running time per trajectory and the number of integration steps to tune the acceptance rate. From this information, BaHaMAS produces an input file for the code and a job script and, if it is a new simulation, also a new folder to save all files of the simulation, and finally submits the job.

The other main feature of BaHaMAS is the monitoring of simulations. For all simulations run on the cluster by the user, it shows the current status, the acquired number of trajectories, the time per trajectory and further colour-coded columns which illustrate if the simulations are running without issues. These columns include the acceptance rate, with the colours green, yellow and red, as well as maxSpikeDS/s,

the maximum distance of the Hamiltonian to the mean in standard deviations for any trajectory and maxSpikeDP/s, which is the same but for the plaquette. If any column turns red, it indicates that the simulation is not running right and the user can investigate what exactly caused this behaviour.

PLASMA and the Fitting GUI

The data obtained from the simulations still needs to be analysed, reweighted and fitted. To analyse and reweight the data, we are using PLASMA (Python Library for Automatized Statistics Management and Analysis), developed by Christopher Pinke and maintained by Francesca Cuteri and Alessandro Sciarra. It is currently being refactored by Reinhold Kaiser and David Palao and will be available in the future under [65]. PLASMA has a multitude of options to choose from concerning the observables that can be analysed and the techniques for analysing the data. When reweighting the data, it also extracts β_c, giving an easily available input for the final fitting procedure, which is explained in more detail in Section 5.2.

This fitting procedure is performed with the Python Fitting GUI [66], created by Reinhold Kaiser. The tool displays the results from our simulations and the procedures in PLASMA, giving the opportunity to interactively tune the fit from which the critical mass will result. It is used to exclude different data points and it also lets the user choose from the many available fit functions: Polynomial fit up to fifth order, were all but the first order can be in- or excluded and rescaled, a General Logistic Fit of Type 1,2,3 and 4 and the option to flip it and a Gompertz fit that can be flipped. With all of these, the correction term explained in Section 4.1 can be turned off and on as well.

Chapter 4

Phase Transitions on the Lattice

This chapter focuses on phase transitions and their connections to symmetries, since the goal of this work is to better understand the deconfinement phase transition of lattice QCD. Afterwards, we are going to discuss Landau theory, the QCD phase diagram and the Columbia plot, the main interest of this work. This chapter is mainly based on [22, 23, 29, 31, 67, 68, 69].

4.1 Phase Transitions in Statistical Mechanics

4.1.1 Theory of Phase Transitions

First, we want to give a short introduction to the general theory of phase transitions. For a more detailed look into the theory of phase transitions, phase diagrams, critical exponents and scaling laws, refer to [70, 71, 67].

A *phase transition* is associated with a change in symmetry, also called *symmetry breaking*, and its order depends on the way and "amount" the symmetry is broken. It also implies that the free energy of the system and its derivatives experience non-analyticities. To observe a phase transition taking place, one uses its *order parameter*, a quantity that on one side of the phase transition is zero and non-zero at the other side. For our simulations we have to keep in mind, that phase transitions can strictly speaking only take place in the infinite volume limit, which is also called the thermodynamic limit, where $V \to \infty$ [72, 73], therefore we will have to perform a finite size scaling analysis.

The three different orders of phase transitions are:

▷ **First order phase transitions:**

After Landau, a first order phase transition takes place when the symmetry and the probability distribution of the system undergo an abrupt change, while at the point of the transition, both phases coexist.

In a more modern definition, a first order phase transition is identified through the absorption or release of latent heat. This means that when the system arrives at the transition temperature, the temperature of the system stays constant while the latent heat is added or released. At this point, the two

phases of the system are coexisting. The discontinuous jump of the order parameter from zero to a non-zero value is also connected to the latent heat.

▷ **Second order phase transitions:**

After Landau, a second order phase transition is defined by the abrupt (dis-) appearance of a number of symmetry elements with only a slight change in the probability distribution of the system.

In the modern approach, at a second order phase transition only the first derivative of the order parameter has a discontinuity and not the order parameter itself. Also, the susceptibility is diverging, the correlation length is infinite and correlations are decaying following power laws.

A line of first order phase transitions ends in a second order endpoint. We will observe this when discussing the QCD phase diagram and the Columbia plot in Section 4.3 and Section 4.4.

▷ **Crossover:**

Crossovers are strictly speaking not true phase transitions and are not as firmly defined as the other orders of phase transitions. A crossover is a rapid change of the system where the order parameter equivalent is changed, but without discontinuities, singularities and divergences in the quantities like the susceptibility, but even though it does not diverge, it reaches a maximum. A crossover is also not associated with a change in the symmetry of the system.

The different phases of matter separated by phase transitions can be depicted in a *phase diagram*. A phase diagram typically shows two thermodynamic quantities plotted against each other, most of the time, the temperature is included. In general, it shows the quantities that are of importance to the understanding of the phase structure, sometimes it is necessary to look at multiple phase diagrams to get a full picture. Typical quantities are, other than the temperature: pressure, density or chemical potential.

A phase diagram usually includes lines of phase transition, also called *phase boundaries*, which separate regions of different phases. Phase boundaries can go to arbitrarily high values, going through the whole phase diagram, or end at fixed values which are called *end points*. In that case, there has to exist an analytical path from one phase to the other, without going through a real phase transition. Phase boundaries are typically either lines of first or second order phase transitions. They can either stay disconnected or cross each other, which results in further special points. For example, a triple point arises where three first order lines meet and a first order line and a second order line meet in a tricritical point.

4.1.2 Universality Classes and Critical Exponents

Another important aspect of phase transitions are universality classes and critical exponents. A group of phenomena with the same set of critical exponents is called a *universality class*. There are three common characteristics which make systems members of the same universality class. These are the symmetry group of the

Hamiltonian, the dimensionality and whether or not their force is short-ranged. As an example, QCD and the 3D-Ising model are, in a certain parameter range, members of the same universality class. This already shows the great benefit of universality classes is to make it possible to study simpler models in order to draw conclusion on the more complicated model one actually wants to study.

Near the critical temperature T_c of the phase transition, certain quantities behave according to power laws, with the exponents of these power laws called *critical exponents*. These critical exponents are also shared by phenomena behaving according to the same universality class. The critical exponents α, β, γ, δ, ν, η are all related to different quantities and are mainly expressed via the reduced temperature $t = \frac{T-T_c}{T_c}$):

- The specific heat: $C_V \sim |t|^{-\alpha}$
- The order parameter: $L \sim |t|^{\beta}$
- The susceptibility: $\chi_t \sim |t|^{-\gamma}$
- The shape of the critical isotherm: $H \sim L^{\delta}$
- The correlation length: $\xi \sim |t|^{-\nu}$
- The correlation function: $G(r) \sim r^{-(d-2+\eta)}$

Table 4.1 shows the relevant critical exponents for our analysis.

	Crossover	1st order	2nd order Z_2
B_4	3	1	1.604
ν	-	1/3	0.6301(4)
γ	-	1	1.2372(5)
α	-	-	0.110(1)

Table 4.1: Values of the kurtosis and of the relevant critical exponents at the transition [74].

4.1.3 Scaling Laws

Scaling of the Free Energy

In 1974, K.G. Wilson developed the Renormalisation Group (RG) [75], building on the work of Widom [76] and Kadanoff [77]. Kadanoff proposed that a diverging correlation length implies a connection between the length scale of the order parameter and the coupling constants of an effective Hamiltonian. On this, Widom built his scaling laws. Scaling the length by $a \to la$, where a is the lattice spacing, the singular part of the free energy density behaves like

$$f_s(t_l, h_l) = l^d f_s(t, h), \tag{4.1}$$

with t the reduced temperature, h the reduced field and d the spatial dimension of the system. The two reduced parameters behave like

$$t_l = tl^{y_t},\ h_l = hl^{y_h};\ \ y_t, y_h > 0. \tag{4.2}$$

The exponents y_t, y_h can be determined through the renormalisation group theory by Wilson [75]. It is possible to conclude on the critical exponent ν in terms of y_t and y_h from the behaviour of the correlation length under n transformations $\xi(t) = l^n \xi(tl^{ny_t})$:

$$\nu = \frac{1}{y_t}. \tag{4.3}$$

Other critical exponents follow from other quantities, like from the free energy density:

$$\frac{d}{y_t} = 2 - \alpha,\ \beta = \frac{d - y_h}{y_t},\ \gamma = \frac{d - 2y_h}{y_t},\ \delta = \frac{y_h}{d - y_h}\ \eta = d + 2 - 2y_h. \tag{4.4}$$

After the calculation of y_t and y_h using the renormalisation-group approach, it is then possible to calculate the critical exponents.

Scaling of QCD

In [78], it was proposed to study the dynamics and universal critical behaviour of QCD in the vicinity of the second order endpoint with a Hamiltonian constructed out of energy-like $\mathcal{E}$ and magnetisation-like $\mathcal{M}$ operators coupling to the scaling fields t and h:

$$\mathcal{H}_{eff}(t, h) = t\mathcal{E} + h\mathcal{M}. \tag{4.5}$$

As expected, the singular part of the free energy scales like

$$f_s(t, h) = l^{-d} f_s(l^{y_t} t, l^{y_h} h), \tag{4.6}$$

where the spatial extent of the lattice in units of the inverse temperature is given by the dimensionless scale $l = LT = N_\mathrm{s}/N_\tau$. The operators of the QCD Lagrangian ($\bar{\psi}\psi$, $\mathcal{S}_\mathrm{g}$,...) are expected to be mixtures of $\mathcal{E}$ and $\mathcal{M}$, because all global symmetries of the QCD Lagrangian are explicitly broken for finite values of the quark mass. An implication from this is that the couplings β, m_q are mixtures of the scaling fields t and h.

Scaling of the Kurtosis

Later, we also need to derive scaling relations for the kurtosis, the fourth generalised cumulant, which is built from the moments of fluctuations of the order parameter O:

$$B_n(O) = \frac{\langle (O - \langle O \rangle)^n \rangle}{\langle (O - \langle O \rangle)^2 \rangle^{\frac{n}{2}}}. \tag{4.7}$$

The kurtosis B_4, which is closely related to the Binder cumulant [79], will help us with the identification of the order of the phase transition, because its value at critical temperature indicates the order of the phase transition. Another important

variable is the third generalised cumulant, the skewness B_3, which helps with identifying the location of the phase transition, since it is expected to vanish at phase transition. More details can be found in Section 5.2.1.

The derivation of the scaling relations of the kurtosis follows [80] and was developed in [81], where this is also discussed in more detail on page 135.

The following notation will be used:

$$\frac{\partial^n}{\partial h^n} F(t,h) = F^{(n)}(t,h). \tag{4.8}$$

Because the kurtosis is constructed from fluctuations δO, first we express it via derivatives of the free energy. From [80], the expression of kurtosis in terms of derivatives with respect to h is given for magnetisation-like operators $\mathcal{M}$:

$$B_4(t,0) = \frac{F^{(4)}(t,h)|_{h=0}}{\left[F^{(2)}(t,h)|_{h=0}\right]^2} = \frac{N_\mathrm{s}^{4y_h} F^{(4)}(tN_\mathrm{s}^{y_t})}{\left[N_\mathrm{s}^{2y_h} F^{(2)}(tN_\mathrm{s}^{y_t})^2\right]} = \frac{F^{(4)}(tN_\mathrm{s}^{y_t})}{\left[F^{(2)}(tN_\mathrm{s}^{y_t})\right]^2}. \tag{4.9}$$

Here, N_s is used as a scaling factor. Next, B_4 is expanded around $t = 0$:

$$B_4(t,0,N_\tau) = \frac{F^{(4)}(0)}{\left(\left(F^{(2)}(0)\right)\right)^2} + AtN_\mathrm{s}^{1/\nu} + \mathcal{O}(t^2 N_\mathrm{s}^{2/\nu}), \tag{4.10}$$

where $y_t = 1/\nu$ was used. The first term is independent of the lattice specifications, because it is the only one to survive at the critical temperature $t = 0$, which is therefore implied to be the value B_4 of its universality class. This can be written as:

$$B_4(t,0,N_\mathrm{s}) = B_4(t,0,\infty) + AtN_\mathrm{s}^{1/\nu} + \mathcal{O}(N_\mathrm{s}^{2/\nu}). \tag{4.11}$$

Our simulation data can be fitted to this, with A to be determined from the fit and $B_4(t,0,\infty)$ and ν known from universality. This is a finite size scaling analysis for a magnetisation-like operator, but the QCD observables are mixtures of energy-like and magnetisation-like operators, for which holds:

$$O = c_M \mathcal{M} + c_E \mathcal{E} \to c_M \frac{\partial}{\partial h} + c_E \frac{\partial}{\partial t}. \tag{4.12}$$

Therefore, we will need two derivatives instead of the one derivative from Eq. (4.8):

$$\frac{\partial^n}{\partial t^n}\frac{\partial^m}{\partial h^m} F(t,h) = F^{(nm)}(t,h). \tag{4.13}$$

Considering these derivatives, the kurtosis can be expressed as

$$\begin{aligned} B_4(t,0,N_\tau) &= \frac{\left(c_M \frac{\partial}{\partial h} + c_E \frac{\partial}{\partial t}\right)^4 F(t,h,N_\mathrm{s}^{-1})|_{h=0}}{\left[\left(c_M \frac{\partial}{\partial h} + c_E \frac{\partial}{\partial t}\right)^2 F(t,h,N_\mathrm{s}^{-1})|_{h=0}\right]^2} \\ &= \frac{F^{(04)}(tN_\mathrm{s}^{y_t})}{\left[F^{(02)}(tN_\mathrm{s}^{y_t})\right]^2}\left[1 + BN_\mathrm{s}^{y_t - y_h} + \mathcal{O}\left(N_\mathrm{s}^{2(y_t-y_h)}\right)\right]. \end{aligned} \tag{4.14}$$

Expanding around $t = 0$ again leads to an additional *correction term*, which can be written as:

$$B_4(t,0,N_\mathrm{s}) = \left(B_4(t,0,\infty) + AtN_\mathrm{s}^{1/\nu} + \mathcal{O}(N_\mathrm{s}^{2/\nu})\right)\left(1 + BN_\mathrm{s}^{y_t-y_h} + \mathcal{O}(N_\mathrm{s}^{2(y_t-y_h)})\right). \tag{4.15}$$

This correction term makes the kurtosis volume dependent at $t = 0$. It is also only relevant for small volumes, because $y_t - y_h$ is negative for the universality class of QCD.

4.2 Landau Theory

Another way to describe phase transitions is Landau theory.

Landau theory is built on the concept that a continuous phase transition can be described by a Landau free energy. The Landau free energy, or Landau functional $\mathcal{L}$, can be described as an expansion in the order parameter η

$$\mathcal{L} = \sum_{i=0}^{\infty} a_i([K], T)\eta^i. \tag{4.16}$$

It depends on the coupling constants K and the temperature T. We will see in the following chapters that for the phase transition we are studying, $T < T_c$ is the ordered phase with $\eta = 0$ and $T > T_c$ is the disordered phase with $\eta \neq 0$. This holds in the case that we have no symmetry breaking field.

The global minimum of $\mathcal{L}(\eta)$ describes the state of the system. This means that the first derivative with respect to η has to be zero.

The Landau functional is expanded to the fourth order, because the order parameter η is assumed to be small and we expect all important physics around T_c to be described sufficiently by this order. This gives for the first derivative

$$\frac{\partial \mathcal{L}}{\partial \eta} = a_1 + 2a_2\eta + 3a_3\eta^2 + 4a_4\eta^3 = 0. \tag{4.17}$$

Since for $T < T_c$, $\eta = 0$, in order to satisfy this condition, $a_1 = 0$ needs to hold.

If we assume that the system, and therefore $\mathcal{L}$, has a symmetry in $\eta \to -\eta$, all odd labelled coefficients are zero. This leaves us with

$$\frac{\partial \mathcal{L}}{\partial \eta} = 2a_2\eta + 4a_4\eta^3 = 0, \tag{4.18}$$

which describes a second order phase transition, as can be seen when looking at the shape of the free energy, cf. Figure 4.1. The coefficients are not necessarily constants, since they have the form $a_i([K], T)$. Therefore, we need to expand them in the temperature T.

For the quartic term $a_4 > 0$ needs to hold, so $\mathcal{L}$ can't be minimized by $\eta \to \infty$. Also, the temperature dependence in the quartic term won't dominate the leading behaviour close to T_c. Therefore, we take $a_4 = a_4^0$ to be a positive constant.

The quadratic term should be expanded around the critical temperature:

$$a_2 = a_2^0 + a_2^T \frac{T - T_c}{T_c} + \mathcal{O}((T - T_c)^2). \tag{4.19}$$

Solving (4.18) for the order parameter leads to two solutions that minimise the Landau functional of a second order phase transition:

$$\eta = 0 \quad \text{or} \quad \eta = \sqrt{\frac{-a_2(T)}{2a_4}}. \tag{4.20}$$

At the point of the phase transition, $a_2 = 0$ has to hold, for $T < T_c$ we have $a_2 > 0$ and for $T > T_c$ it should be $a_2 < 0$. This can only be valid if $a_2^0 = 0$. Hence we know

that $a_2 = a_2^T \frac{T-T_c}{T_c}$, because the leading behaviour around T_c contains no contribution of the higher order terms.

It is now also possible to extend the analysis of the second order phase transition to the addition of an external field H. This leads to the Landau functional

$$\mathcal{L} = a_2^T \frac{T - T_c}{T_c} \eta^2 + a_4 \eta^4 - H\eta. \tag{4.21}$$

Here, the order parameter is coupling to the external field.

It is not as easy to minimize the order parameter in this case, because the constant term in the first derivative prevents us from rewriting the equation to a quadratic equation:

$$\frac{\partial \mathcal{L}}{\partial \eta} = 2a_2^T t\eta + 4a_4\eta^3 - H = 0, \tag{4.22}$$

with $t = \frac{T-T_c}{T_c}$. In order to understand better what happens at the phase transition, it is helpful to look at the Landau free energy and how it depends on the temperature T and the external field H, as depicted in Figure 4.1. In the middle, one sees the standard case with $H = 0$, so no external field. For $T < T_c$, $\mathcal{L}$ has a minimum at $\eta = 0$. At $T = T_c$, the minimum is still at $\eta = 0$, but the Landau functional also has zero curvature. For $T > T_c$, there are now two degenerate minima at $\eta = \pm\eta_s(T)$ instead of just one minimum. The value of n_s depends on T.

For an external field $H < 0$, $\mathcal{L}$ is tilted to the left: for $T < T_c$, the minimum is no longer at $\eta = 0$, but at some value $\eta = -\eta_s(T)$, which again depends on T. At $T = T_c$, the minimum moves further to the left and gets deeper, and the Landau functional has again zero curvature around $\eta = 0$. For $T > T_c$, again a second minimum develops, but this time the minima are not degenerate, but the minimum that was present from the beginning is moving further to the left and deeper again. The image for $H > 0$ is analogous, the only difference is that the Landau functional now tilts to the right.

It is also possible to describe a first order phase transition with Landau theory. The Landau functional for a first order transition is constructed in a similar way, but with an additional cubic term:

$$\mathcal{L} = a_2^T t\eta^2 + a_3\eta^3 + a_4\eta^4 - H\eta. \tag{4.23}$$

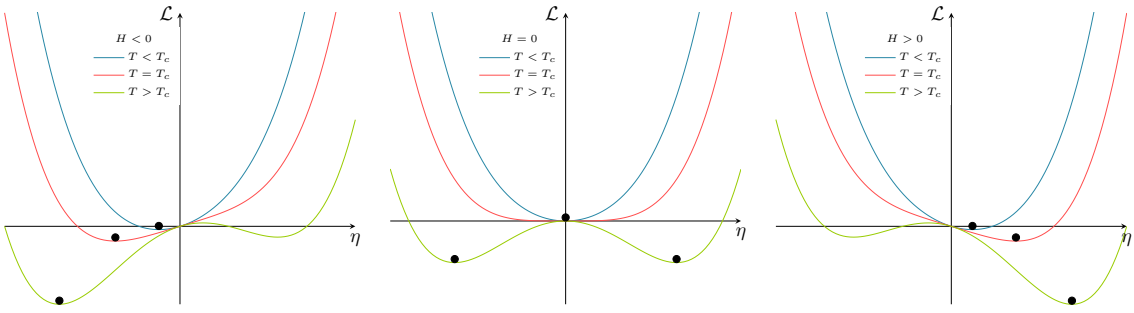

Figure 4.1: Schematic illustrations of the Landau functional for a second order phase transition for different values of T and H. The global minimum is depicted by a black dot. The left figure depicts the Landau functional for $H < 0$, the central figure for $H = 0$ and the right figure for $H > 0$. In all three plots, the temperature T gets varied from below T_c to above T_c.

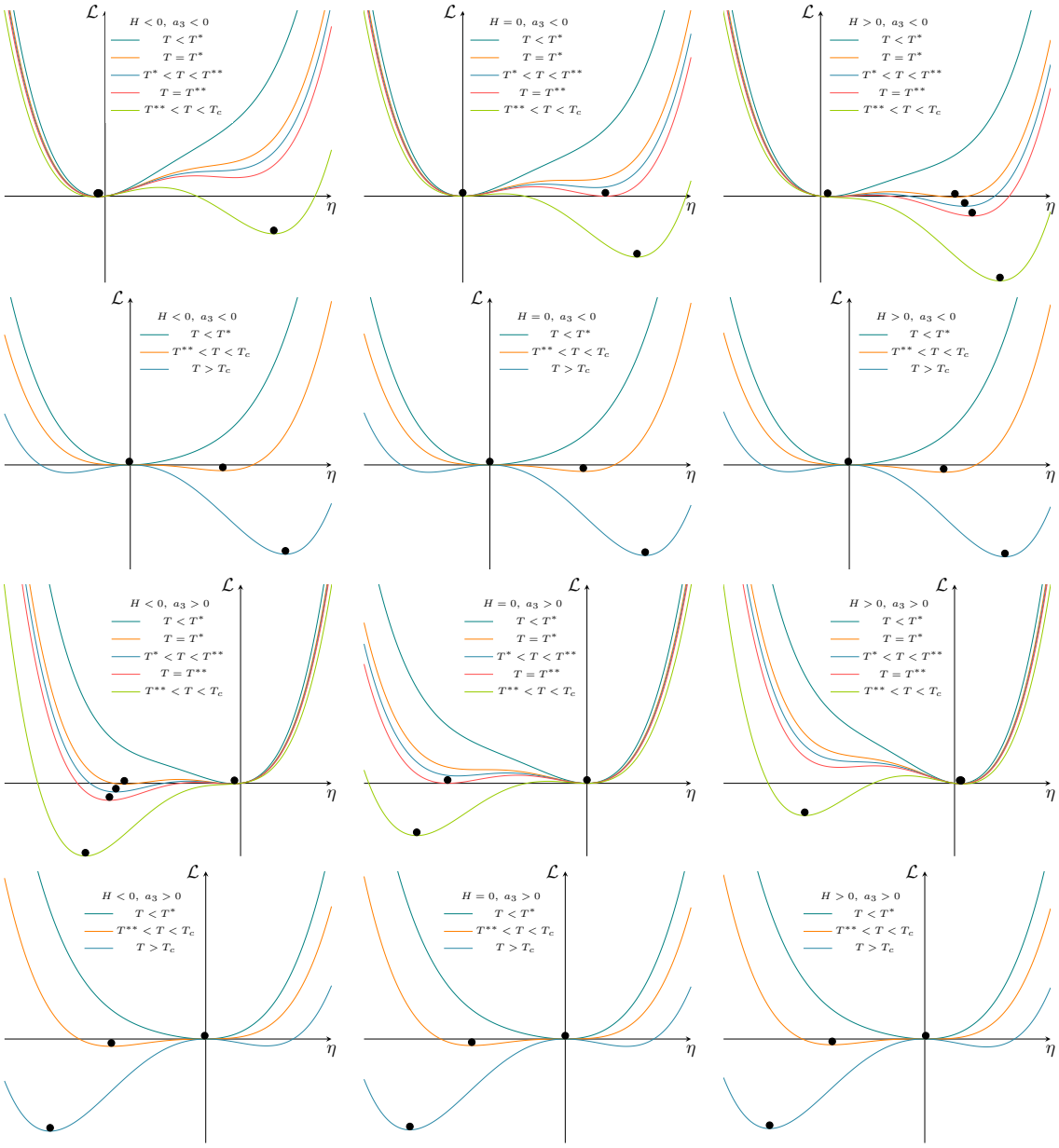

Figure 4.2: Schematic illustrations of the Landau functional for a first order phase transition for different values of T, H and a_3. The global minimum is depicted by a black dot. The left figures depict the Landau functional for $H < 0$, the central figures for $H = 0$ and the right figures for $H > 0$. The top two rows depict $\mathcal{L}$ for $a_3 < 0$ and the bottom two rows for $a_3 > 0$. The temperature T is varied from below T^* to above T_c. Since the temperature spans a large region, the plots are split up: The first and the third row have a more detailed view on the temperature changes around $T = T^{**}$, the second and fourth row show the bigger picture, going up to $T > T_c$.

We take T_c to be the temperature at which the phase transition in the second order case, so for $a_3 = 0$, would occur. We will see later, that T_c has no relevance in a first order phase transition, like we expect from the fact that a first order phase transition

involves latent heat, which leads to a mixing of the phases. We also assume that a_3 is constant.

Again, taking the derivative, setting it to zero and solving for η only yields a reasonably short solution for $H = 0$

$$\eta = 0 \quad \text{or} \quad \eta = \frac{-3a_3 \pm \sqrt{9a_3^2 - 32a_4 a_2^T t}}{8a_4}. \tag{4.24}$$

The second solution is only real for

$$9a_3^2 - 32a_4 a_2^T t > 0, \text{ so } t > t^* \equiv \frac{9a_3^2}{32a_4 a_2^T}, \tag{4.25}$$

which is a temperature smaller than T_c, since a_2^T is negative and therefore t^* is also negative.

Again, it is helpful to look at qualitative figures of $\mathcal{L}$ vs η to see how the additional cubic term influences the developments of the minima. This is depicted in Figure 4.2.

For temperatures $T < T^*$, $\mathcal{L}$ has only one minimum at $\eta = 0$, the system is in the disordered phase.

At $T = T^*$, a second minimum evolves. At this point, the minimum at $\eta = 0$ is still the global one and the new minimum is only a local minimum. Here, the ordered phase is metastable.

At the new transition temperature $T^{**} > T^*$, the minima are both at $\mathcal{L} = 0$, so they are both the global minimum. Here, the disordered and the ordered phase are coexisting.

When further increasing T, so that $T > T^{**}$, the second minimum decreases further and becomes the global minimum. The ordered phase is stable now and the disordered phase metastable.

If we increase T further, so that $T > T_c$, with T_c the temperature at which the second order phase transition would occur, the minimum at $\eta = 0$ is now a local maximum, as a new minimum develops at $\eta < 0$ for $a_3 < 0$ or at $\eta > 0$ for $a_3 > 0$, so at the opposite sign as the global minimum. This minimum will always be only a local minimum. The global minimum stays at $\eta > 0$ for $a_3 < 0$ or $\eta < 0$ for $a_3 > 0$ and the ordered phase stable, so no phase transition occurs at $T = T_c$.

We can calculate T^{**}, since we know the necessary conditions:

$$\mathcal{L}(\eta) = 0 \quad \text{and} \quad \frac{\partial \mathcal{L}(\eta)}{\partial \eta} = 0, \quad \text{with} \quad \eta \neq 0 \tag{4.26}$$

Solving these equations for t and η leads to

$$t = t^{**} = \frac{a_3^2}{4a_4 a_2^T}, \quad \eta = \eta^{**} = -\frac{a_3}{2a_4}. \tag{4.27}$$

Adding an external field H tilts the curves, like it also does in the second order case. This shifts the minima significantly, the Landau functional is a lot more sensitive to the external field H than it was for the second order phase transition. Since a_3 can be positive or negative, we depicted both possibilities.

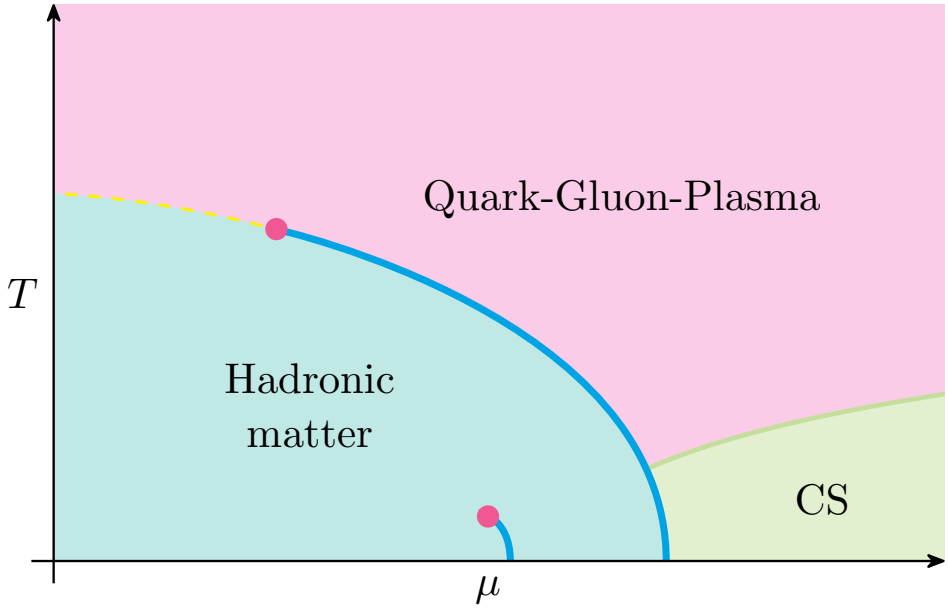

Figure 4.3: Schematic illustration of the QCD phase diagram in the $T-\mu$-plane for $N_\mathrm{f} = 2+1$ flavour QCD. The colour conventions for the phase transitions are the following: Yellow indicates a crossover, blue a first order transition, pink a second order endpoint and green indicates that the order of the phase transition is still open to discussion.

4.3 The QCD Phase diagram

The structure of the QCD phase diagram has been studied for decades, but still only few facts are known about it. The reason for this is, that experimentally it can only be studied in particle colliders and all tools for theoretical investigations have their difficulties. More information is provided in Chapter 1. Most of the information on the QCD phase diagram stems from calculations, simulations and approximations, but there are also parts that are only known from symmetry arguments.

The phase diagram, depicted in Figure 4.3, has the temperature T on the y-axis and the baryochemical potential μ on the x-axis. The upper half of the QCD phase diagram shows the quark-gluon plasma, which is the deconfined phase because of asymptotic freedom, which is also chirally symmetric, so the chiral condensate vanishes $\langle\bar{\psi}\psi\rangle = 0$. At $\mu = 0$, the critical temperature T_c was found to be $T_c = 150-170$ MeV [82]. In this transition, the hadrons get broken up and a gas consisting of quarks, gluons, electrons and further particles, which condenses to a QGP, gets created. Here, also the chiral symmetry is broken, $\langle\bar{\psi}\psi\rangle \neq 0$. In the lower left, at vanishing temperatures and chemical potentials, there is a vacuum, which, at small temperatures and chemical potentials, turns into a gas of hadrons which, when further increasing the chemical potential to $\mu = 900$ MeV, transitions into nuclear matter, which turns into ordinary atomic matters at chemical potentials larger than this critical chemical potential. The phase boundary separating the hadronic matter from the QGP is a crossover at high temperatures and small chemical potentials,

because the chiral symmetry is explicitly broken by the mass term. This has been checked for $\mu = 0$ with lattice QCD [28] to be indeed at $T_c \approx 150 - 170$ MeV. When lowering the temperature and increasing the chemical potential, the phase transition is suggested from lattice QCD to turn into one of the first order type phase transition [83, 84], leading to a second order endpoint between the first order phase transition and the crossover. When going to very high chemical potentials, there might be a transition to colour superconducting matter [85, 86, 87]. Other phases might also exist, but about their existence even less is known.

Theoretical investigations of the QCD phase diagram mostly focus on three quarks only, using a degenerate up and down quark and a strange quark, because this makes the calculations easier and still gives a good approximation since the dynamics of heavy quarks are negligible. The investigation of different regions needs different approaches, around $\mu = 0$ lattice QCD is used because this region can't be investigated with perturbative methods, but when going to finite chemical potentials, the sign problem hinders the usage of lattice QCD. Lattice QCD also has the problem of discretisation effects, which influence the position of the endpoints [88]. In those regions, it is then best to use other techniques, like effective models that have the same symmetries as QCD and belong to its universality class, but these only work around critical points.

4.4 The Columbia Plot

A different way to depict the QCD phase diagram is the *Columbia plot*, which was first developed in 1990 [89]. The classic version of it can be seen in Figure 4.4, with an alternative scenario depicted in Figure 4.5. The colour scheme of the figures is identical to the one in Figure 4.3. Yellow represents a crossover, blue indicates a first order phase transition and pink depicts a second order Z_2 transition. The brown line shows a line of triple points and lilac portrays a $O(4)$ transition.

The Columbia plot is not a phase diagram, because it does not show different phases and is depicted entirely at $T = T_c$ and $\mu = 0$. Instead, it shows how the order of the phase transition changes with the three lightest quark masses, where we assume degenerate up and down quarks because they are about 30 times lighter than the strange quark. If one wanted to add temperature as a third axis, below the Columbia plot one would have hadronic matter and above the quark-gluon plasma.

The vertical axis of the Columbia plot contains the strange quark mass, the horizontal axis contains the degenerate up and down quark mass. Both masses go from zero to ∞, where they decouple from the theory, the heavier quarks are therefore all assumed to have $m_q = \infty$. This also establishes the information about the number of flavours N_f. At the right, $N_\mathrm{f} = 1$ means that the up and down quarks are decoupled from the theory. The same happens at the top with the strange quark, where $N_\mathrm{f} = 2$, but additionally the up and down quark are degenerate. On the diagonal, all three quark masses are degenerate, leading to $N_\mathrm{f} = 3$. Everywhere else, including the physical point, as is to be expected from the QCD phase diagram, the strange quark has a mass different from the light quarks, leading to $N_\mathrm{f} = 2 + 1$ flavours.

From a phase and symmetry standpoint, the Columbia plot shows the chiral

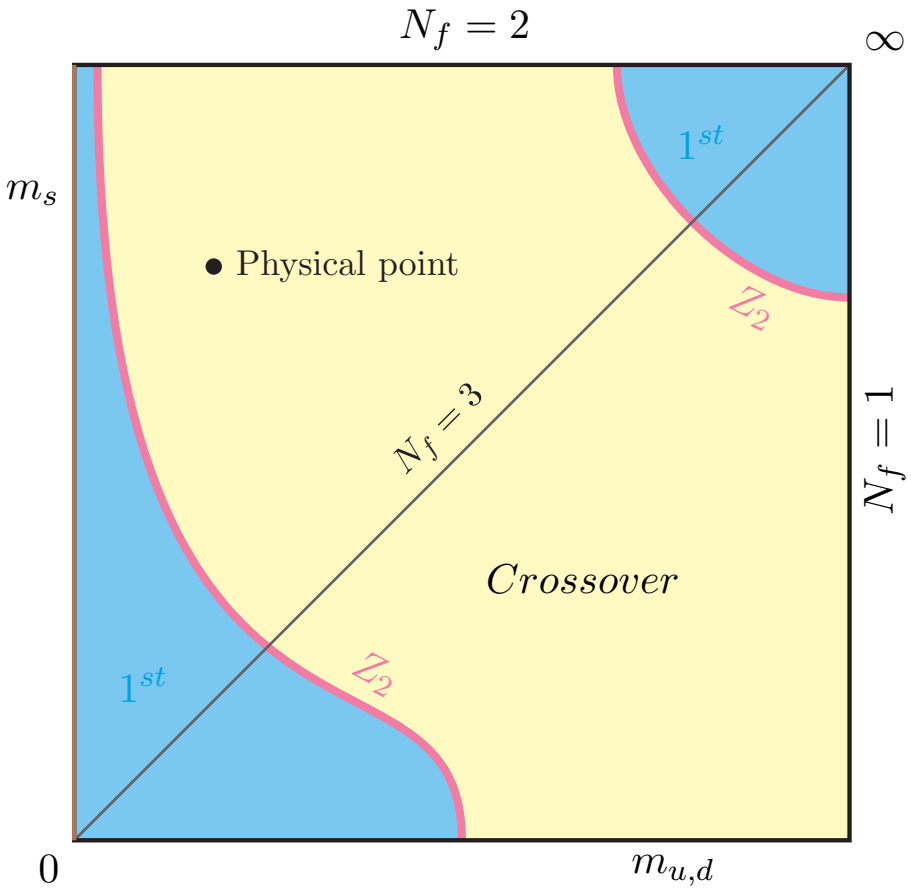

Figure 4.4: The Columbia plot. Shown is a classic first order scenario, where the first order region in the light quark region is expanding up to $m_s \to \infty$.

transition in the lower left corner, which is therefore also called the chiral corner, and the deconfinement transition in the upper right corner, the deconfinement region.

The transition at low masses, at the right edge of the Columbia plot with $N_\mathrm{f} = 1$, is a crossover, since no symmetry breaking can occur, because all symmetries at this point are just phase factors [90]. In the chiral corner, were all quark masses are small, the phase transition is of a first order type, bordered by a Z_2 line, which shape is not yet concluded on. When $m_q = 0$ for all three flavours, the chiral symmetry can break spontaneously, leading to a first order phase transition. In Figure 4.4, a line of first order triple transitions take place at the left edge of this region. There, three phases are coexisting, one high temperature phase where the chiral symmetry is in place with $\langle\bar{\psi}\psi\rangle = 0$ and two low temperature, chirally-broken phases with $\langle\bar{\psi}\psi\rangle \neq 0$, where the two phases have different signs. At the bottom edge though, there are no tricritical points because the chiral symmetry can't exist for only one massless quark, which is also the reason for the crossover region in the right corner. When going to small, but finite masses, the chiral condensate is not a true order parameter anymore, because the masses explicitly break the symmetry, weakening

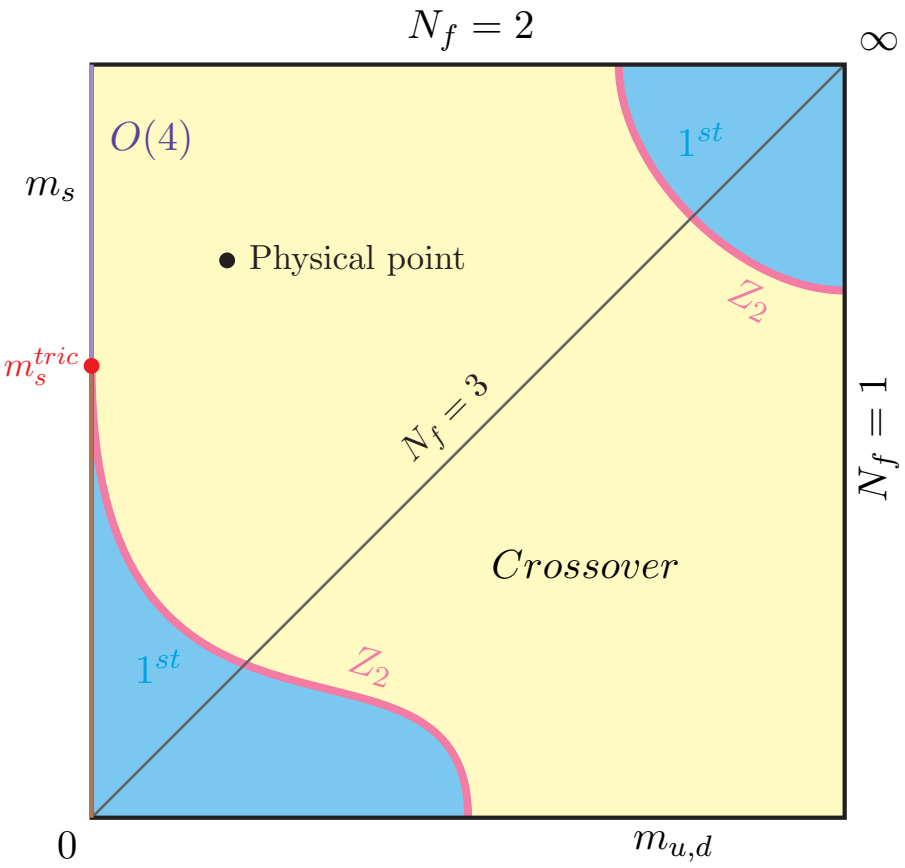

Figure 4.5: The Columbia plot. Shown is a classic second order scenario, where the first order region in the light quark region is ending at a finite value of m_s on a tricritical point.

the first order phase transition until it ends in a Z_2 line, after which it turns into a crossover. Moving further on the $N_\mathrm{f} = 3$ line, the crossover persists for most of the Columbia plot until it ends in another Z_2 line, followed by a first order region extending until the quenched limit $m_q \to \infty$ is reached. This is the deconfinement region, which we will analyse for $N_\mathrm{f} = 2$ in this thesis, investigating the location of the $N_\mathrm{f} = 2$ Z_2 point. Qualitatively, the curvature of the deconfinement first order region is known from simulations, which are comparatively easy to run in this region. At infinite masses the transition takes place through a spontaneous breaking of the centre symmetry, which we discussed in Section 2.7. Lowering the quark masses to finite values, it is possible to interpret them as an external field which explicitly breaks the centre symmetry, weakening the first order phase transition until it ends in the Z_2 line, vanishing into the crossover.

The left edge of the Columbia plot is also of great interest, though not relevant for this work. The situation there is not clear, because simulations are very expensive and multiple scenarios are possible. In both scenarios depicted here, starting at a low mass for the strange quark and $m_{u,d} = 0$, is a line of tricritical points and at

$m_{u,d}$ small a first order phase transition. When increasing m_s, the first order phase transition and the line of tricritical points might persist until $m_s = \infty$, as depicted in Figure 4.4, or the first order phase transition might end in a line of $O(4)$ points as depicted in Figure 4.5. In [91] it is even suggested that the $O(4)$ line extends down to 0, so that there is no first order chiral region at all and the left axis consists entirely of $O(4)$ points.

Overall, the structure of the Columbia plot is not yet set in stone, a status about current investigations can be found in [92]. The Z_2 lines for $N_\mathrm{f} = 3$ were found, but are not yet reaching a proven value, but a trend is visible where finer lattices and improved actions are lowering the critical mass. It was also observed that studies with Wilson fermions result in heavier masses than studies with staggered fermions [93].

Other than straightly simulating the Columbia plot, it can also be investigated via imaginary chemical potential, analysing the Roberge-Weiss symmetry while avoiding the sign problem. From these results it is possible to extrapolate to $\mu = 0$ and learn about the usual Columbia plot this way. It is also possible to simulate at non-integer N_f [91], then extend these results into the chiral limit where the surface has to end in a tricritical line and analyse it via tricritical scaling relations.

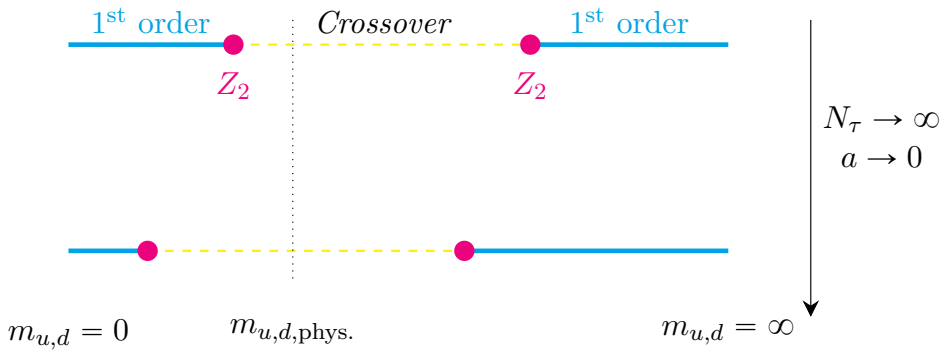

Figure 4.6: Partially taken from [94]. This figure shows the qualitative shift of the Z_2 point when the lattice spacing is being decreased.

Another difficulty regarding the Columbia plot are discretisation effects: the Z_2 lines shift with decreasing lattice spacing [95], which is depicted in Figure 4.6. With the simulations, we want to reach a continuum result, letting $a \to 0$ so the systematic error, which stems from the discretisation of the theory, can be removed, but going to finer lattices influences the phase structure, shifting the position of the Z_2 lines.

Depending on the fermion discretisation, the result for the mass m_{Z_2} gets a systematic error of order a, getting closer to the real value when simulating finer lattices, but still the mass will only reach the true value at $a = 0$. For Wilson fermions, this error is linear in a:

$$m_{Z_2}(a) = m_{Z_2}(0) + \sum_{i=1}^{\infty} c_k a^k. \tag{4.28}$$

It is feasible to assume that only the leading order of the error $\mathcal{O}(a)$ gives a significant contribution, so that only the sign of c_1 has an influence on the direction of the shift between $m_{Z_2}(a)$ and $m_{Z_2}(0)$, dictating if the first order phase is shrinking or growing when going to finer lattices. From lattice studies, it can be assumed that the sign of c_1 is positive, making the deconfinement first order region grow and the chiral first order region shrink with increasing lattice size [96, 97, 82].

Chapter 5

Finding κ_{Z_2}

We will begin this chapter with a discussion about how our simulations where run, going into a discussion about the analyses using standardised moments and Landau theory, and the results from these methods.

5.1 Running the Lattice Simulations

Here, we want to discuss the simulations that were run. We used unimproved Wilson fermions, so that unphysical modifications of the phase structure can be ruled out. We also want to be able to control the phase transition as a function of the lattice spacing a to study cut-off effects on the pion mass at the Z_2 point quantitatively. The simulations were controlled, in addition to the temporal extent N_τ and the spatial extent N_s, via two parameters: The hopping parameter $\kappa = (2(am_0^{(f)} + 4))^{-1}$ is used to control the mass and the lattice coupling β controls the temperature $T = (a(\beta)N_\tau)^{-1}$. During the simulations, we measured at every trajectory.

When simulating, we first focussed on one N_τ, where we simulated at $N_\tau \in \{6, 8, 10, 12\}$, where the smallest N_τ was simulated first. For every N_τ, the goal is to find the mass κ_{Z_2} at Z_2. Therefore simulations at different κ are run, making it possible to scan for κ_{Z_2}. Per κ, different volumes N_s were run, using aspect ratios in the range of $N_\mathrm{s}/N_\tau \in [3, 6]$ and for $N_\tau = 8$ and $N_\tau = 12$ one simulation at $N_\mathrm{s} = 80$. This is done to make a finite size analysis possible to handle the finite volume effects. For every combination of N_τ, κ and N_s, simulations at two to four β values were run, so we can scan for the critical temperature of the phase transition β_c. Finally, for multiple reasons that we will explain in a short while, every β value gets simulated by two to four Markov chains with different starting seeds.

Simulations with CI^{2}QCD were thermalised from Hot with 1k trajectories for one β, followed by a thermalisation from Conf, meaning it starts from the last configuration of the thermalisation from Hot, with 4k trajectories at every β to be simulated, most of the time using just one chain. For simulations with openQCD-FASTSUM the same process was followed, only with 9k trajectories in the thermalisation from Conf instead of 4k trajectories. These trajectories of the thermalisation phase are afterwards discarded from the analysis. When this thermalisation procedure is finished, the real simulations are started at all the β values that were thermalised from Conf, using two or four chains for each. During the simulations, the Polyakov loop

and the Plaquette get measured at every trajectory. We also tuned the acceptance rate to stay between 75% and 85%. Almost all simulations were performed using CL^{2}QCD, only the simulations for $N_\tau = 8$, $N_\mathrm{s} = 80$ and for $N_\tau = 12$, excluding $N_\mathrm{s} = 36, 48$ were performed using openQCD-FASTSUM. Over all chains, for every β, 56k to 800k trajectories were accumulated. The goal was to reach at least 50 independent events per β, but that was not always reached for the highest aspect ratios, the details can be found in Table A.1, Table A.2 and Table A.3.

The simulations for measuring the mass and lattice spacing for a defined κ were run at $N_\tau = 32$, $N_\mathrm{s} = 16$, as a consequence of the constraint $N_\tau > N_\mathrm{s}$ for zero temperature simulations. To minimise the finite size effects, the simulations were run at β_c of the largest N_s, only when the quality of this simulation was not sufficient, β_c of the next smaller N_s was chosen. It was also necessary to obtain the mass and lattice spacing for κ_{Z_2}, but since there were no previous simulations at this point directly, $\beta_\mathrm{c}(\kappa_{Z_2})$ was reached by an interpolation described in Section 5.3.2. The simulation procedure was close to the one described before, the thermalisation process for the mass simulations was identical to the one described before. Mostly, 4 chains were simulated, only for simulations at the Goethe-HLR 8 chains were run because the GPUs there have 8 cores per node, meaning that the simulation of 8 chains came at no additional cost. 10k trajectories were accumulated per chain and every 50th configuration was saved, leading to either 800 or 1600 configurations to determine the pion mass and perform the scale setting on.

Now it is time to discuss why we use multiple Markov chains. The first reason is simple, since one chain has to run continuously, the simulations can run for months, sometimes even years, therefore running multiple chains helps to accumulate the necessary statistics a lot faster, halving or even quartering the real time needed, since all chains can run in parallel, as long as there is enough space on the cluster. It is still important though to let every chain run for a long enough time so that every chain observes multiple events after accounting for the autocorrelation time, because the chains will be simply appended to each other for the data analysis and the breaks between the chains should not influence the results. The breaks might indicate that the simulation stayed longer or shorter in one phase than it actually did. Because each break influences the autocorrelation time, the number of breaks must be much lower than the number of events. Another reason to use multiple chains is to control the statistical error better. With multiple chains it is very unlikely that more than one chain will go on a statistically unlikely path, which avoids reaching a false conclusion. It is also easier to ensure the statistics are sufficient when using multiple chains. To make use if this, the skewness had to be compatible within at most 3 standard deviations between all chains before the runs were stopped, Figure 5.1 depicts an example of this. The standard deviation n_σ used to monitor this criterion is defined using the expectation value $\langle O \rangle_i$ of the observable O with the statistical error σ_i, where i denotes the different Markov chains:

$$n_\sigma = \max_{i<j} \left(\frac{|\langle O \rangle_i - \langle O \rangle_j|}{\sqrt{\sigma_i^2 + \sigma_j^2}} \right). \tag{5.1}$$

This criterion is also fulfilled at very small statistics due to the large statistical error,

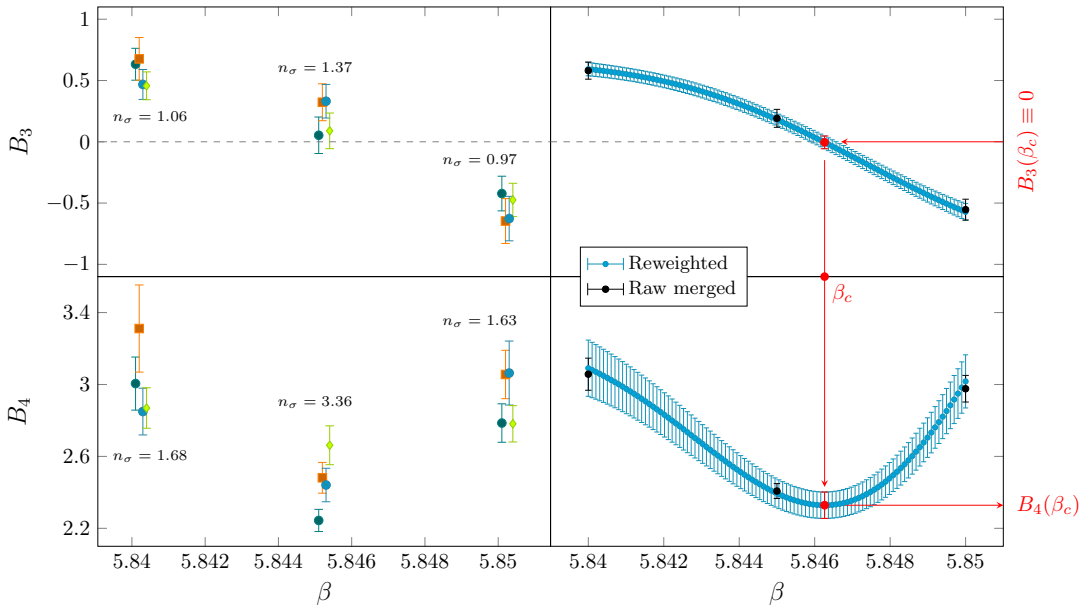

Figure 5.1: Taken from [94]. Examples of the data analysis of the skewness B_3 (top) and of the kurtosis B_4 (bottom). All examples are depicted at $\kappa = 0.1100$ on a 6×36^3 lattice. Depicted are the different Markov chains (left), with a slight horizontal shift added to improve visibility. n_σ describes the difference between the maximally incompatible pair in standard deviations. The right side shows the merged raw and the reweighted data for both observables, with β_c and $B_4(\beta_c)$ marked in red.

therefore it was also almost always demanded that for the smallest and largest β, the skewness B_3 has to be incompatible with zero at 1 standard deviation. This ensures small enough errors so that the data points can be allocated unambiguously either below or above zero. When these criteria were met, the chains were combined, an example of this are the black data points depicted on the right side of Figure 5.1.

5.1.1 Autocorrelation Time Analysis

Now, we want to discuss the impact of the autocorrelation time on our simulation strategy. The theory about the autocorrelation time τ_{int} was discussed in Section 3.2. Qualitatively speaking, the autocorrelation time parametrises the memory of the dynamics of the system, which depend strongly on the order of the phase transition the system is experiencing.

When one is far away from the first order phase transition that the system with a finite volume will undergo, the system stays in its phase with some given autocorrelation time τ_{int}. The probability distribution will then take on an approximately Gaussian shape, while the order parameter is fluctuating around its mean value. Increasing the temperature until the system is close to the critical temperature β_c, both phases of the system will start to be explored. The order parameter will therefore fluctuate around the mean of one phase, then it jumps into the other phase

and fluctuates around that phases mean. This leads to a two-peak structure in the probability distribution, that will shift into another approximate Gaussian when the system is deep into the second phase. Because a potential barrier growing with volume exponentially suppresses the tunnelling between two phases, the fluctuations in one phase are faster than the fluctuations between two phases [98]. The dynamics therefore occur on a larger timescale, leading to a much longer-term memory of the system. This also leads to an increase in the autocorrelation time τ_{int}, because it is connected with the average tunnelling rate taking place between two phases, which in turn means that it is necessary to simulate a sufficient number of tunnelling events for a reliable estimate of τ_{int}.

With a system undergoing a crossover transition, the distribution is always showing an approximate Gaussian shape, even close to and at β_{c}, only the variance is increasing slightly. Since the order parameter does not fluctuate between the two phases the way it does for a first order phase transition, the autocorrelation time τ_{int} is expected to be small for a crossover. In a system with a second order phase transition, critical slowing down is an important factor, leading to an increase in τ_{int} because of the maximum in the correlation length at the phase transition.

The results for the autocorrelation time were obtained with the Γ-method [44] via a Python script for the Skewness B_3 and the Kurtosis B_4, like it was discussed in Section 3.2. Table A.2 and Table A.3 give an overview of τ_{int} for B_3 and B_4. To obtain the autocorrelation time, an average over the simulated β was performed. Also, the binning procedure was used to retrieve the number of statistically independent events.

Figure 5.2 confirms our understanding of the connection between the autocorrelation time and the order of the phase transition. Both figures show the autocorrelation time of the skewness for the simulated β which is the closest to β_{c}. Figure 5.2(a) shows, for $N_\tau = 8$, the autocorrelation time as a function of N_{s} and κ. κ_{Z_2} is marked with a dashed line. For all volumes, the maximum of the autocorrelation time is around κ_{Z_2}, which displays that we have indeed critical slowing down close to the second order phase transition. The peak would be expected to be sharper if the simulations were run directly at κ_{Z_2} and β_{c} This figure also shows, very drastically, the increase of the autocorrelation time with growing volume N_{s}. Figure 5.2(b) depicts the autocorrelation time for varying N_τ with a fixed aspect ratio $N_{\text{s}}/N_\tau = 6$. Because κ_{Z_2} varies with N_τ, the x-axis shows $\kappa - \kappa_{Z_2}$, so that the second order phase transition takes place at 0. Again, around the critical region, an increase of τ_{int} can be observed, as well as an increase with increasing N_τ, which is consistent with Figure 5.2(a).

These observations about the autocorrelation time help us with the practical organisation of our simulations. The β values to simulate at need to have a sufficiently narrow spacing between them for the reweighting procedure, but they still need to keep a large enough distance from each other, so β_{c} can be pinned down using as few simulations as possible. It is therefore necessary to monitor and analyse the running simulations on a regular basis, so that simulations too far away from β_{c} can be stopped early on and new simulations can be started in their place without wasting computing time. This process takes longer on finer lattices, because those need simulations at larger N_{s} for increasing N_τ, with β values that need to be closer

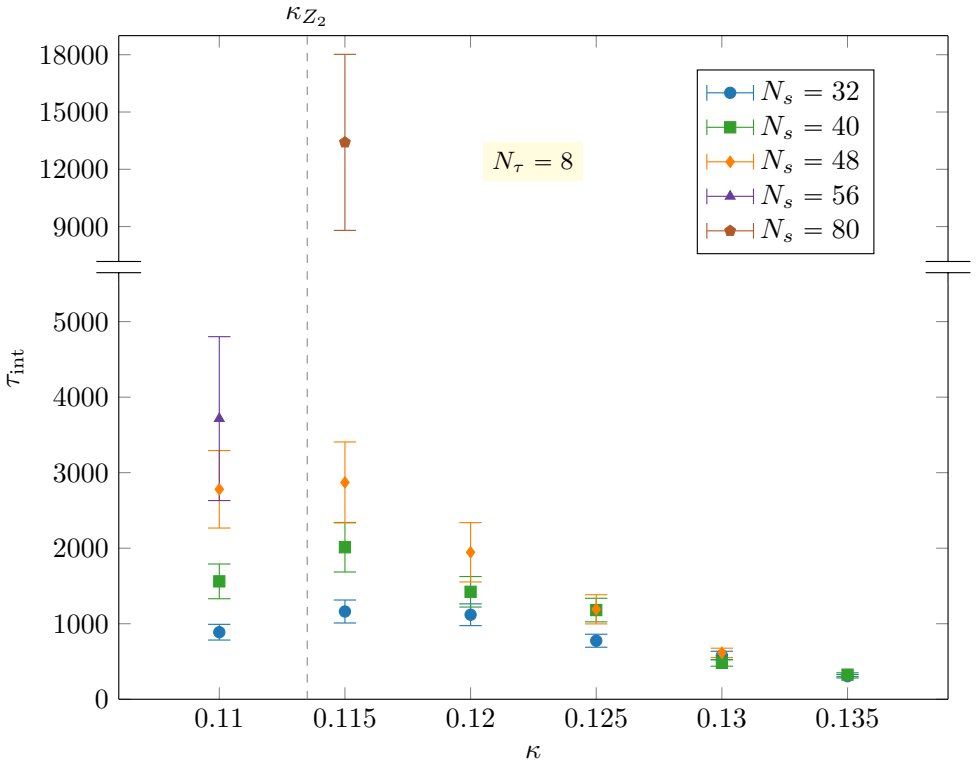

(a) Fixed N_τ.

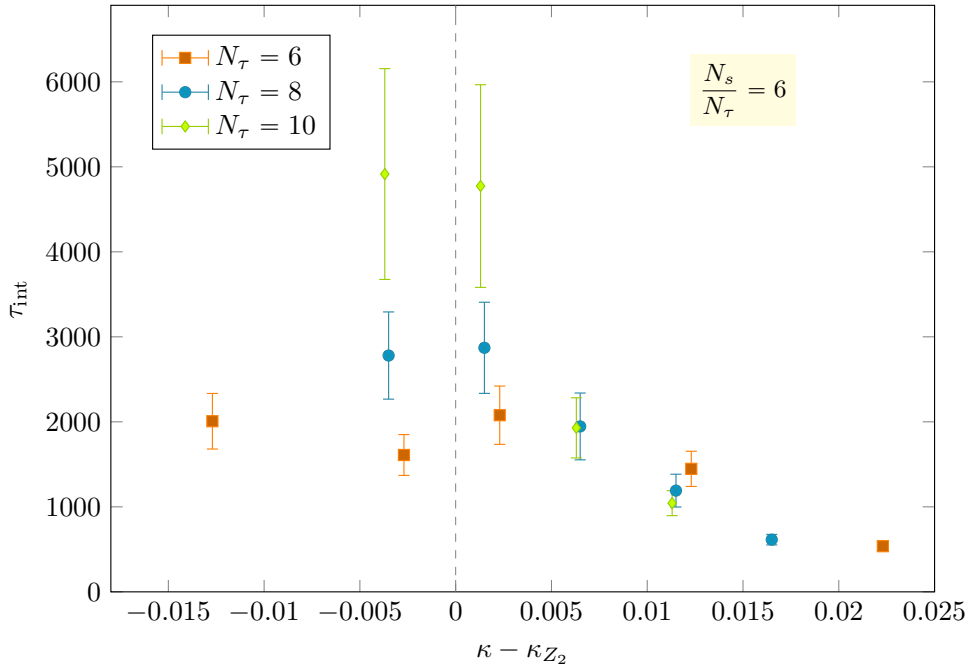

(b) Fixed aspect ratio.

Figure 5.2: Taken from [94]. Shows the integrated autocorrelation time τ_{int} of the order parameter for the skewness at different values of κ. To stay as close to the phase transition as possible, τ_{int} is depicted for the simulated β which was the nearest to β_c. In (a), the spatial volume is varied and N_τ is kept fixed. The dashed line represents κ_{Z_2}. In (b), N_τ is varied and the aspect ratio is fixed. τ_{int} is plotted against $\kappa - \kappa_{Z_2}$.

to each other with increasing N_τ and more needed statistics with increasing N_τ and N_s, as follows from finite size effects, the needed overlap of the histograms discussed in Figure 3.1 and this study of the autocorrelation times. This shows how difficult it can be to reach sufficient statistics for our studies, a painful example for this is $N_\tau = 12$ with aspect ratio 5, which is a low aspect ratio even for the smaller N_τ, but for $N_\tau = 12$ these simulations led to only 20 independent events, even though the statistics are comparable to other simulations at lower N_τ.

5.2 Finding κ_{Z_2} via Standardised Moments

This chapter describes how we obtain the critical mass κ_{Z_2} using the standardised moments and the results of this process, which have been published up to $N_\tau = 10$ in [94]. We describe the fitting procedure, the results of this, and the results stemming from the calculation of the pion mass and lattice spacing.

5.2.1 Using the Skewness and Kurtosis to find κ_{Z_2}

Skewness and Kurtosis

The first step for finding κ_{Z_2} is to pin down the phase transition, which means finding β_c, for every κ. To detect the phase transition, we use the inverse lattice gauge coupling β to control the temperature and observe our order parameter, the Polyakov loop L at each β. Since we are not in the infinite volume limit, the Polyakov loop is not a true order parameter, so we need to use some method other than simply looking at the value of the order parameter to identify the phase transition.

Instead, we observe the skewness B_3 and kurtosis B_4, the third and fourth generalised moment, which are both built from the fluctuations of the order parameter. The generalised moments are written, with the Polyakov loop $|L|$ as the order parameter, as:

$$B_n(|L|) = \frac{\langle(|L| - \langle|L|\rangle)^n\rangle}{\langle(|L| - \langle|L|\rangle)^2\rangle^{n/2}}. \tag{5.2}$$

The third moment, $n = 3$, which is the skewness, indicates how much a distribution is skewed, a positive skewness means the distribution is skewed to the right and a negative skewness describes a distribution skewed to the left. The skewness is expected to vanish at the phase transition, because both phases are populated equally, making the distribution symmetric. One has to be careful though, as the skewness is also zero far away from the phase transition, since the distribution takes the shape of a Gaussian there, even though in this case, the shape of the skewness should look different than around the phase transition.

The kurtosis is the fourth moment, $n = 4$, which is related to the Binder cumulant [79], they only differ by an additive factor of 3 by which the kurtosis is larger than the Binder cumulant. The kurtosis shows the amount of weight in the tails of distributions, having a minimum at the critical temperature. It also contains information about the order of the phase transition, because its minimum value depends on the universality class of the transition. Table 4.1 shows this for the three types of phase transitions relevant for this thesis. These characteristic values

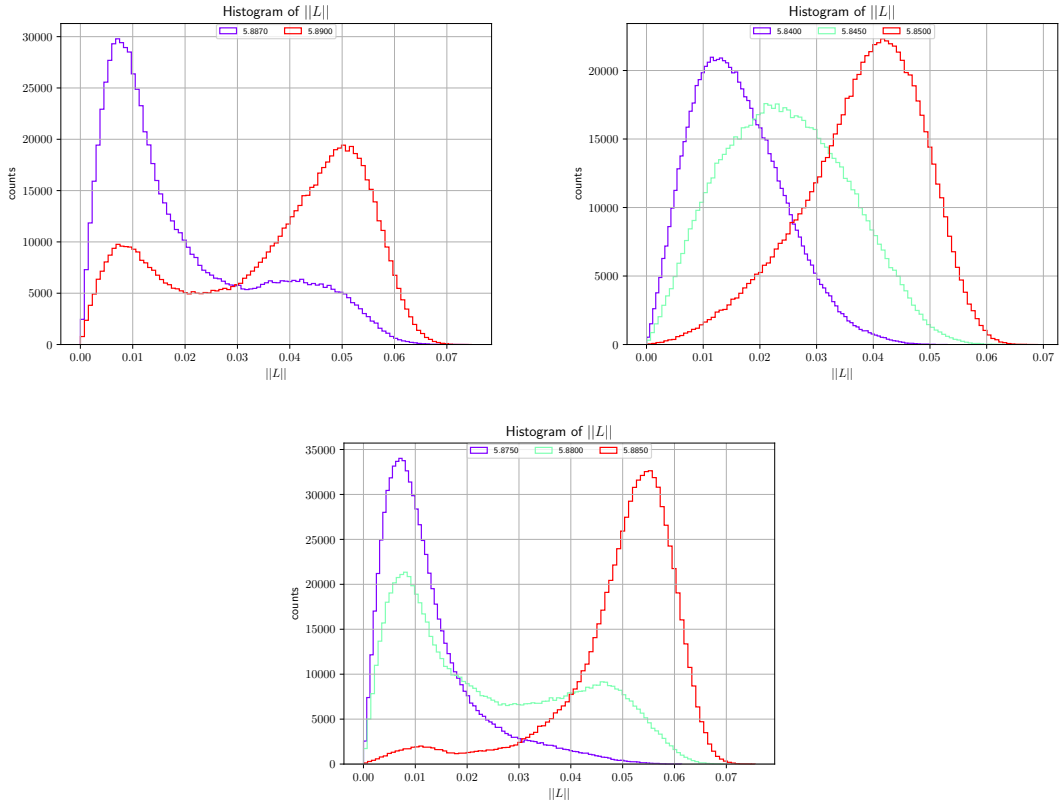

Figure 5.3: Example of histograms generated by PLASMA. All three are depicted for $N_\tau = 6$, $N_\mathrm{s} = 36$, the different colours denote different β values. The upper left one is in the first order region at $\kappa = 0.075$, the lower middle one is close to κ_{Z_2} at $\kappa = 0.09$ and the upper right one is in the crossover phase at $\kappa = 0.11$. One can see how the distribution changes with the order of the phase transition.

make it very suitable to use for extracting the order of the phase transition from our simulations.

A good way to check visually if one is close to the phase transition or so far away that the skewness turned zero again is to look at the histograms, examples of which can be seen in Figure 5.3. When simulating at β values far to the left and to the right of the critical temperature β_c, both distributions have a Gaussian-like shape but are distinguished by the position on the x-axis of their mean. The distribution at β_c has its centre in the middle of these peaks.

At a first order phase transition at $\beta = \beta_\mathrm{c}$, the distribution has a characteristic two-peak structure in the histogram. In a crossover, the Gaussian-like distribution is simply placed in the middle of the two peaks but doesn't change its shape. At the second order phase transition, at κ_{Z_2}, the histogram at β_c takes on a plateau shape, which shows the transition from first order to crossover. Knowing the different shapes around β_c for the different orders of phase transition therefore helps to visually confirm that one is simulating around β_c.

Finding the phase transition and its order

When finding the phase transition, we first find β_c by reweighting the results and then using $B_3(\beta_c) = 0$ to pin it down exactly. The kurtosis is also reweighted, to get an accurate value for $B_4(\beta_c)$. This will not be exactly the same as the values from universality though, because we are not in the thermodynamic limit, rather they will overshoot for the first order phase transition and undershoot for the crossover.

The kurtosis is an analytic curve on finite volumes, which with increasing volume approaches a step function, because this is the form of the kurtosis in the thermodynamic limit. From universality it is implied that the kurtosis is, close to κ_{Z_2}, a function of only the scaling variable

$$x = (\kappa - \kappa_{Z_2}) N_s^{1/\nu}. \tag{5.3}$$

This is used when expanding the kurtosis in a Taylor series around $\kappa = \kappa_{Z_2}$, which can be truncated after the linear term for sufficiently large volumes:

$$B_4(\beta_c, \kappa, N_s) = B_4(\beta_c, \kappa_{Z_2}, \infty) + a_1 x + \mathcal{O}(x^2). \tag{5.4}$$

This is the linear function we fit the results $B_4(\beta_c, \kappa, N_s)$ obtained from reweighting to, so that the data points for every N_s form a separate line, which are all forced to intersect at κ_{Z_2}. This holds only for asymptotically large volumes, which we cannot assume for all our simulations. From the autocorrelation study done before, as well as from [99] and [100], it is known that the higher volumes can be prohibitively expensive to attain, especially as for the heavy mass region the required aspect ratios are even higher because the regular, non-divergent contributions to the fluctuations are growing there, forming a need for larger volumes so the diverging terms can dominate. Therefore, we need to consider leading finite volume corrections, which were explained in Section 4.1, resulting in the fit function

$$B_4(\beta_c, \kappa, N_s) = [B_4(\beta_c, \kappa_{Z_2}, \infty) + a_1 x + \mathcal{O}(x^2)] \times [1 + B N_s^{(\alpha-\gamma)/2\nu}], \tag{5.5}$$

where B is a non-universal fit parameter. With this fit function, the kurtosis function is no longer linear and the curves of the different volumes N_s are no longer intersecting at one point, but intersect pairwise, a qualitative example is given in Figure 5.4.

An alternative way to fit would be to correct the finite volume effects by leaving the critical exponents B_4 and ν as free parameters, but this way, information about universality would be lost. Also, because the kurtosis lines would still intersect at a single point, this would not guarantee a proper extraction of κ_{Z_2}.

Performing the kurtosis fits

Here, we will explain the theory behind the actual fitting procedure, the execution will be discussed in Section 5.2.2, which contain the results.

An important point is the fit quality, which we measure with two parameters, the reduced chi-square $\chi^2_{\text{d.o.f}}$ and the Q-parameter, which, when a Gaussian noise in the data is assumed, describes the probability of receiving a chi-square larger than $\chi^2_{\text{d.o.f}}$. An optimal fit has $\chi^2_{\text{d.o.f}} \approx 1$ and $Q \approx 50\%$. Further constraints exist for the

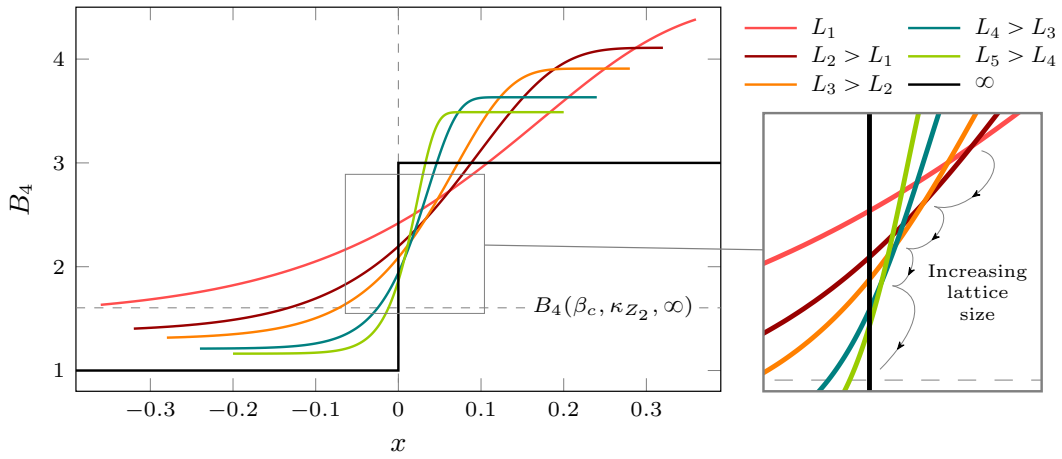

Figure 5.4: Taken from [94]. Shown is the qualitative behaviour of the kurtosis B_4 when the leading finite size correction, Eq. (5.5), is used instead of Eq. (5.4), because of small spatial volumes. The kurtosis at κ_{Z_2} is shifted to larger values and, with growing volumes, approaches the universal value. The enlarged visual on the right side makes clear that the volumes do not cross in one point anymore and shows the convergence of the pairwise intersections for to $B_4(\beta_c, \kappa_{Z_2}, \infty)$ when approaching the thermodynamic limit.

fit parameters, a_1 has to be positive because the fit function has to monotonically increase.

If the finite size effects are negligible, we expect that Eq. (5.4) and Eq. (5.5) give both fits of good quality, with B compatible with zero and κ_{Z_2} consistent between both fits. The strategy is therefore to perform fits with both methods, then compare them and to isolate the leading terms. This is done by successively excluding points, starting from the smallest volume of the fit, until B is compatible with zero. Then, the other fit parameters are checked for consistency between the fits. It is very important to not exclude points without a strategy, because this can lead to overfitting. It is also important to include as many points as possible into the fit, because this decreases the biases that single kurtosis points might have due to statistical and locally limited systematic errors.

We also observed that the fit quality is increased when κ values deep in the first order region are excluded all together. There are multiple reasons for this phenomenon. Firstly, the volume dependent exponential suppression of tunnelling between the phases in the first order region makes it difficult to determine these points accurately. Additionally, the kurtosis curve is not symmetric around the inflection point κ_{Z_2}, complicating a linear fit, because the universal value for the first order region and the crossover region don't have the same distance to the universal value of the Z_2 point. Also, Table 5.1 shows that for the smallest κ values, the masses rise very quickly, making it necessary to use higher order terms in the Taylor series expansion in both brackets of Eq. (5.5), because of the larger finite size corrections and the larger distance from the critical point. This means that the number of fit parameters would need to be increased, making it harder to draw a conclusion from the fit. It is still of highest importance to include at least one κ

reliably in the first order region in the fit, not doing this allows biases into the fit. An easy way to check this visually is to observe the ordering of the points regarding N_s. In the first order region, the data point for the highest N_s has the lowest B_4 value, while the data point for the lowest N_s is the highest B_4 value. In the crossover region, this is reversed.

To summarize, we first simulate at different β values for the different κ, N_s and N_τ, taking the histograms as a first inclination if we are in the right region and accumulating statistics on these. The resulting skewness and kurtosis are then reweighted, β_c is extracted where the skewness $B_3 = 0$ and the kurtosis at the phase transition $B_4(\beta_\mathrm{c}, \kappa, N_\mathrm{s})$ is obtained. These kurtosis values are then fitted to extract κ_{Z_2} for every N_τ. This will be discussed in the following four sections for every N_τ we simulated at.

5.2.2 Results of the Kurtosis Fits

$N_\tau = 6$

We are starting the discussion about the results with the smallest N_τ, which was already started and mostly finished by Christopher Czaban [81], but for this work and [94], we cleaned up the data and reran a few simulations to bring the statistics to a better point. The data quality is therefore very good, as can be seen in Table A.1.

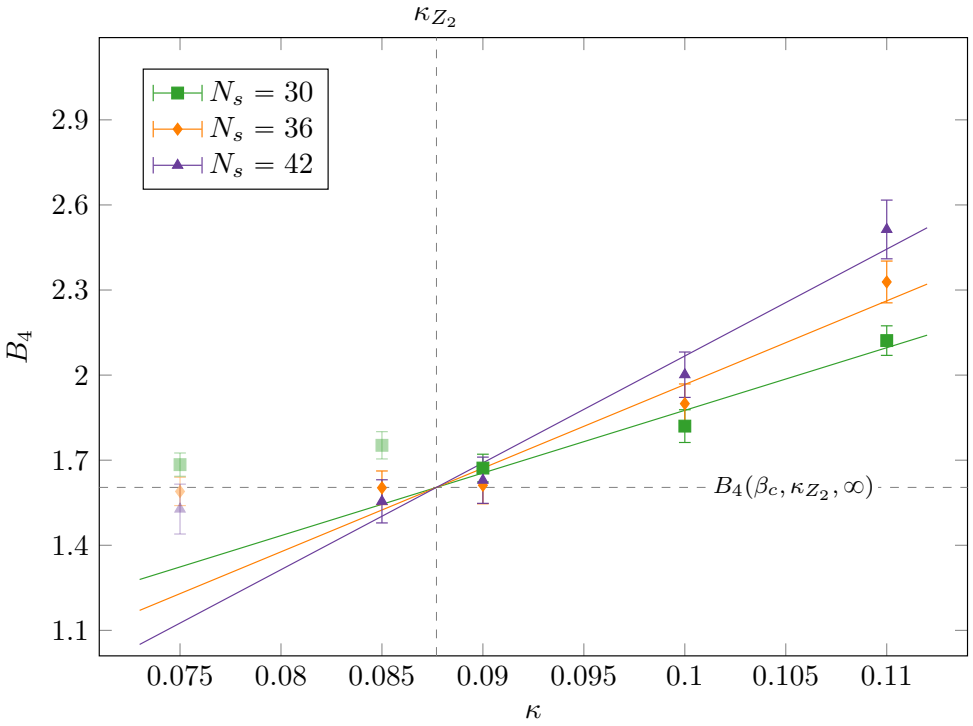

Figure 5.5: Taken from [94]. Final B_4 fit for $N_\tau = 6$. Depicted is fit $e.6.1$, which is marked with a blue background in Figure 5.6. The shaded points have been excluded from the fit.

Fit label	Included/Excluded κ per N_s	κ_{Z_2}	a_1	B	$\chi^2_{\text{d.o.f}}$	NDF	Q[%]
	0.075 0.085 0.09 0.1 0.11						
	30 ✗ ✗ ✓ ✓ ✓						
e.6.1	36 ✗ ✓ ✓ ✓ ✓	0.0877(9)	0.100(7)	–	0.87	9	55
i.6.1	42 ✗ ✓ ✓ ✓ ✓	0.0878(21)	0.099(9)	0.1(9)	0.98	8	45
	0.075 0.085 0.09 0.1 0.11						
	30 ✗ ✗ ✓ ✓ ✓						
e.6.2	36 ✗ ✗ ✓ ✓ ✓	0.0895(11)	0.112(10)	–	0.49	7	85
i.6.2	42 ✗ ✗ ✓ ✓ ✓	0.0902(22)	0.110(11)	0.3(9)	0.54	6	78
	0.075 0.085 0.09 0.1 0.11						
	30 ✗ ✗ ✓ ✓ ✓						
e.6.3	36 ✓ ✓ ✓ ✓ ✓	0.0828(11)	0.072(5)	–	3.33	11	0
i.6.3	42 ✓ ✓ ✓ ✓ ✓	0.0839(27)	0.070(6)	0.4(9)	3.65	10	0
	0.075 0.085 0.09 0.1 0.11						
	30 ✗ ✗ ✗ ✗ ✗						
e.6.4	36 ✗ ✓ ✓ ✓ ✓	0.0876(10)	0.099(9)	–	1.09	6	37
i.6.4	42 ✗ ✓ ✓ ✓ ✓	0.089(4)	0.097(12)	0.6(2.2)	1.29	5	26

Figure 5.6: Partially taken from [94]. Overview over the results of the final fits, presenting the effect of excluding different data points for $N_\tau = 6$. The labelling of the fits takes the form $x.y.z$. x describes the fit ansatz, taking the values $x = e$ for fits according to Eq. (5.4), leading to $B =$ " $-$ ", which *exclude* the correction term, and $x = i$ when the correction term is *included*, performing the fits according to Eq. (5.5). y shows the value of N_τ. z is counting, and therefore distinguishing, the different fits. $z = 1$ represents the best fit we chose as the final one, which is also indicated by the blue background. The second column contains subtables which show the exclusion pattern of the data points. For every κ (columns) at the different N_s values (rows) it is marked, which points have been included (✓) or excluded (✗).

After running the new simulation, we also reperformed the fits originally performed by Christopher Czaban, leading to different results. We found the critical mass to be at $\kappa_{Z_2}(N_\tau = 6) = 0.0877(9)$, which corresponds to the fit marked in blue in Figure 5.6, which is also shown in Figure 5.5, whereas in [81], the critical mass was found to be $\kappa_{Z_2}(N_\tau = 6) = 0.0939(14)$.

Figure 5.6 shows a selection of different fits, with and without using the correction term, for varying combinations of excluded points.

The first fits, *e*.6.1 and *i*.6.1, exclude all volumes for $\kappa = 0.075$, because from the ordering of the points, which can be seen in Figure 5.5, it is indicated that $\kappa = 0.085$ is already in the first order region and $\kappa = 0.075$ already lies quite deep in the first order region, so including it could hurt the fit quality. The reasons for this were discussed in Section 5.2.1. We also excluded the second smallest $\kappa = 0.085$ for the smallest volume $N_\text{s} = 30$ to increase the fit quality, following our main strategy.

Both fits received with this fit strategy, with and without using the correction term, agree very well with each other, the two results for κ_{Z_2} being nearly identical. Also, B is very much compatible with zero and is overall very small.

The second fits, $e.6.2$ and $i.6.2$, additionally exclude all volumes for $\kappa = 0.85$, just so we can see what happens when all points that are reliably in the first order region are excluded. Both κ_{Z_2} agree with each other within error bounds, but not as closely as in the first fits. The overall fit result is about 0.002 higher than from the first fits, B still agrees with zero, but the fit has an overall worse quality.

In the third fits, $e.6.3$ and $i.6.3$, only $\kappa = 0.075$ an $\kappa = 0.085$ were excluded for $N_\mathrm{s} = 30$, demonstrating our main fitting procedure by itself. The resulting κ_{Z_2} values are about 0.004 smaller than in the first fit and differ quite a bit, but still agree with each other within error bounds and B is compatible with zero. The overall fit quality is very bad though, showcasing that excluding all but one κ in the first order region can lead to a better fit quality.

The last fits, $e.6.4$ and $i.6.4$, have the same exclusion pattern like the first fits, but they exclude all $N_\mathrm{s} = 30$, to push our main strategy a bit more by excluding more of the κ values at small volumes. The precision of the fit including the correction term suffered, the result is one digit less precise, which also increases the error on κ_{Z_2} enormously. A reason might be that the number of degrees of freedom is quite small for this fit. The overall fit quality is not too bad though, but the decline of the precision is concerning.

Concluding, B is fully controlled in all fits, indicating that the simulated volumes are large enough to control finite size effects. Overall, the best fit is the first one, and since B is compatible with zero and therefore fully controlled, we chose the linear fit as our final result.

$N_\tau = 8$

For $N_\tau = 8$ the simulation process was identical to $N_\tau = 6$, the simulations were mostly finished by Christopher Czaban [81] and polished for this work. The critical mass found here lies at $\kappa_{Z_2}(N_\tau = 8) = 0.1135(8)$, as shown in Figure 5.7 and Figure 5.8, whereas the critical mass from [81] has the value $\kappa_{Z_2}(N_\tau = 8) = 0.1167(12)$.

The exclusion pattern of the first fits $e.8.1$ and $i.8.1$ looks a bit counter-intuitive at a first glance, since we excluded the smallest $\kappa = 0.11$, but not for the highest volume $N_\mathrm{s} = 56$, since we still need at least one point in the first order region. Including $\kappa = 0.11$ for $N_\mathrm{s} = \{40, 48\}$ gives a very bad fit though, making it necessary to exclude these points, even if this doesn't follow our usual pattern. The results for κ_{Z_2} are identical for both the exclusion and inclusion of the correction term, only the error changing a bit, also B is equal to zero. The fit quality is also good, so even if the exclusion pattern might seem odd, the fit is of excellent quality.

In the second fits, $e.8.2$ and $i.8.2$, for $\kappa = 0.11, 0.115$, all volumes were excluded, just as $\kappa = 0.12$ for $N_\mathrm{s} = 32$. The resulting κ_{Z_2} are close to each other, B is compatible with zero and the overall fit quality is good.

The third fits, $e.8.3$ and $i.8.3$, simply have $N_\mathrm{s} = 32$ excluded for all κ, because we wanted a fit including most volumes for $\kappa = 0.11$ and this fit was the only one with a decent, but still far from good, quality. The κ_{Z_2} values differ a lot from each other and B is not compatible with zero, making it a bad fit overall.

Fit label	Included/Excluded κ per N_s	κ_{Z_2}	a_1	B	$\chi^2_{\text{d.o.f}}$	NDF	Q[%]
	0.11 0.115 0.12 0.125 0.13 0.135 32 ✗ ✗ ✓ ✓ ✓ ✓ 40 ✗ ✓ ✓ ✓ ✓ ✓ 48 ✗ ✓ ✓ ✓ ✓ · 56 ✓ · · · · · 80 · ✓ · · · ·						
e.8.1		0.1135(8)	0.140(9)	–	1.05	13	39
i.8.1		0.1135(11)	0.140(14)	0.0(9)	1.14	12	32
	0.11 0.115 0.12 0.125 0.13 0.135 32 ✗ ✗ ✗ ✓ ✓ ✓ 40 ✗ ✗ ✓ ✓ ✓ ✓ 48 ✗ ✗ ✓ ✓ ✓ · 56 ✗ · · · · · 80 · ✗ · · · ·						
e.8.2		0.1163(11)	0.170(15)	–	0.88	8	53
i.8.2		0.1160(14)	0.174(21)	−0.3(1.1)	0.99	7	43
	0.11 0.115 0.12 0.125 0.13 0.135 32 ✗ ✗ ✗ ✗ ✗ ✗ 40 ✓ ✓ ✓ ✓ ✓ ✓ 48 ✓ ✓ ✓ ✓ ✓ · 56 ✓ · · · · · 80 · ✓ · · · ·						
e.8.3		0.1108(8)	0.110(9)	–	1.49	11	13
i.8.3		0.1136(24)	0.099(12)	2.4(1.9)	1.47	10	14
	0.11 0.115 0.12 0.125 0.13 0.135 32 ✗ ✗ ✗ ✗ ✗ ✗ 40 ✗ ✓ ✓ ✓ ✓ ✓ 48 ✗ ✓ ✓ ✓ ✓ · 56 ✗ · · · · · 80 · ✓ · · · ·						
e.8.4		0.1133(10)	0.134(12)	–	0.71	8	68
i.8.4		0.1131(21)	0.137(20)	−0.3(2.1)	0.81	7	58

Figure 5.7: Partially taken from [94]. Overview over the results of the final fits, presenting the effect of excluding different data points for $N_\tau = 8$. The labelling of the fits takes the form $x.y.z$. x describes the fit ansatz, taking the values $x = e$ for fits according to Eq. (5.4), leading to $B =$ " $-$ ", which *exclude* the correction term, and $x = i$ when the correction term is *included*, performing the fits according to Eq. (5.5). y shows the value of N_τ. z is counting, and therefore distinguishing, the different fits. $z = 1$ represents the best fit we chose as the final one, which is also indicated by the blue background. The second column contains subtables which show the exclusion pattern of the data points. For every κ (columns) at the different N_s values (rows) it is marked, which points have been included (✓) or excluded (✗). A gray cells shows that at this point, no simulation was performed.

The last fits, *e*.8.4 and *i*.8.4, exclude $\kappa = 0.11$ and $N_s = 32$ completely. Both κ_{Z_2} agree quite well with each other, B is compatible with zero and the overall quality is also fine, but not as good as in the first and second fits.

From the fit quality, it is hard to decide between the first and second fits, but we decided on the first fits, because the second fits exclude all points in the first order

region, making them very unreliable. Since $B = 0$, we picked the linear fit excluding the correction term, which can be seen in Figure 5.8.

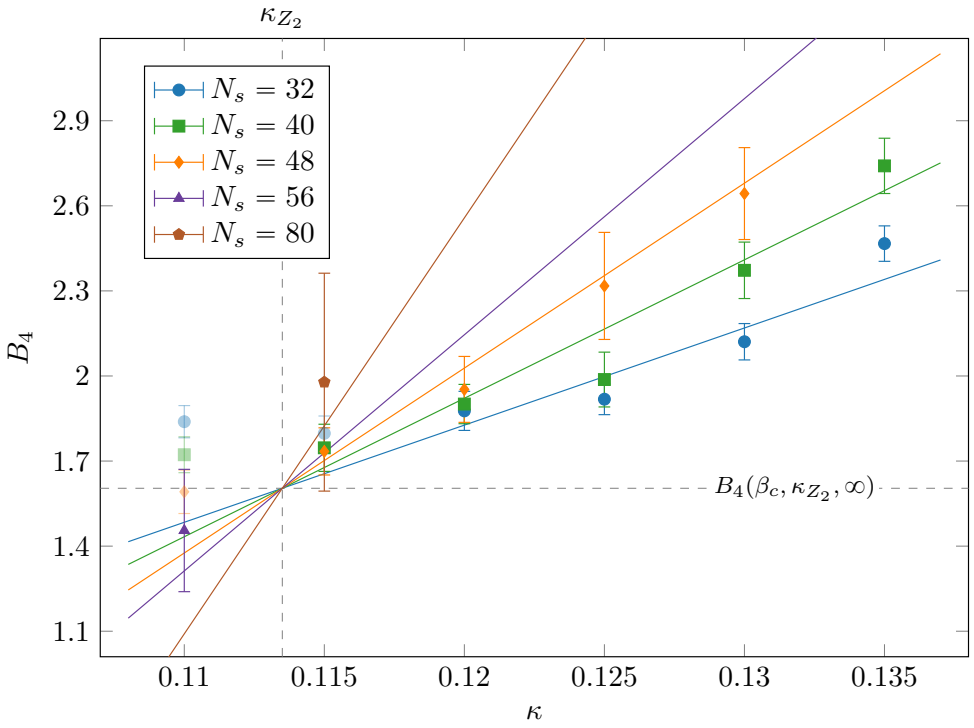

Figure 5.8: Taken from [94]. Final B_4 fit for $N_\tau = 8$. Depicted is fit e.8.1, which is marked with a blue background in Figure 5.7. The shaded points have been excluded from the fit.

$N_\tau = 10$

The $N_\tau = 10$ simulations were again started by Christopher Czaban [81], but did not achieve high enough volumes. Therefore, a significant amount of time was spent on running additional simulations for $N_\tau = 10$ and finishing up the ones already started. We found a critical mass of $\kappa_{Z_2}(N_\tau = 10) = 0.1237(21)$, which is also depicted in Figure 5.9 and Figure 5.10, whereas the preliminary studies in [81] gave a critical mass of $\kappa_{Z_2}(N_\tau = 10) = 0.1229(10)$. The statistics for $N_\tau = 10$ are not as high as we would have wished for because of the increasing simulation time, but are still sufficient to reach an adequate conclusion on κ_{Z_2}.

In the first fits, e.10.1 and i.10.1, we only excluded two points from the smallest physical volume, following our main strategy. The resulting κ_{Z_2} don't agree too well with each other, the one using the correction term being significantly higher than the one without. Also B is not compatible with zero anymore, but the overall fit quality is not great, but still fine.

The second fits, e.10.2 and i.10.2, additionally exclude all of $\kappa = 0.12$ to check if this would exclude all points in the first order region. The κ_{Z_2} are higher than in

Fit label	Included/Excluded κ per N_s	κ_{Z_2}	a_1	B	$\chi^2_{\text{d.o.f}}$	NDF	Q[%]
$e.10.1$	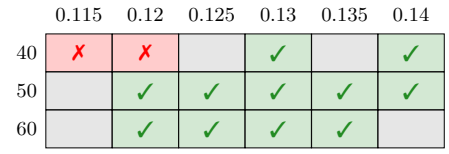	0.1214(12)	0.109(14)	–	1.36	9	20
$i.10.1$		0.1237(21)	0.091(17)	3.0(2.1)	1.25	8	26
$e.10.2$	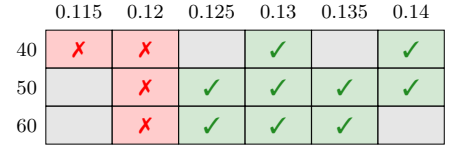	0.1244(11)	0.147(19)	–	0.59	7	77
$i.10.2$		0.1260(17)	0.127(23)	2.7(2.2)	0.41	6	87
$e.10.3$	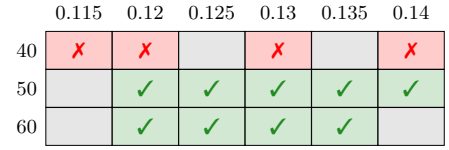	0.1205(17)	0.089(16)	–	1.05	7	39
$i.10.3$		0.124(5)	0.077(20)	4(6)	1.11	6	35
$e.10.4$	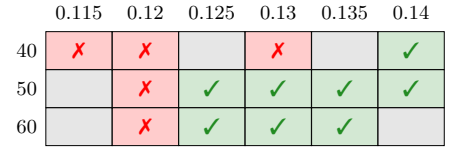	0.1246(11)	0.148(19)	–	0.64	6	70
$i.10.4$		0.1269(23)	0.113(29)	5(4)	0.38	5	86

Figure 5.9: Partially taken from [94]. Overview over the results of the final fits, presenting the effect of excluding different data points for $N_\tau = 10$. The labelling of the fits takes the form $x.y.z$. x describes the fit ansatz, taking the values $x = e$ for fits according to Eq. (5.4), leading to $B =$ " $-$ ", which *exclude* the correction term, and $x = i$ when the correction term is *included*, performing the fits according to Eq. (5.5). y shows the value of N_τ. z is counting, and therefore distinguishing, the different fits. $z = 1$ represents the best fit we chose as the final one, which is also indicated by the blue background. The second column contains subtables which show the exclusion pattern of the data points. For every κ (columns) at the different N_s values (rows) it is marked, which points have been included (✓) or excluded (✗). A gray cells shows that at this point, no simulation was performed.

the first fits, but paint a similar picture as in the first fits, also with B not being compatible with zero. The fit quality is again not good, but good enough.

In the third fits, $e.10.3$ and $i.10.3$, only $N_\text{s} = 40$ is excluded, leading to an improved fit quality. The precision of κ_{Z_2} for the fit including the correction term is down to three digits, telling on a difficult fit, it is also much higher than κ_{Z_2} without the correction term. B is surprisingly compatible with zero, though.

The fourth fits, $e.10.4$ and $i.10.4$, are nearly identical with the second fits, only $\kappa = 0.13$ for $N_\text{s} = 40$ is additionally excluded. The results for κ_{Z_2} resemble the results of the second fits, B is also not compatible with zero, but the fit quality seems to be increased.

The fit including the correction term always producing a higher κ_{Z_2} than the ones without the correction term, coupled with the fact that B is mostly not compatible with zero, hints at us not simulating at large enough aspect ratios. We therefore

need to consider the correction term to obtain an accurate fit result, which lead to us picking the first fit including the correction term as our final result, which can also be seen in Figure 5.10.

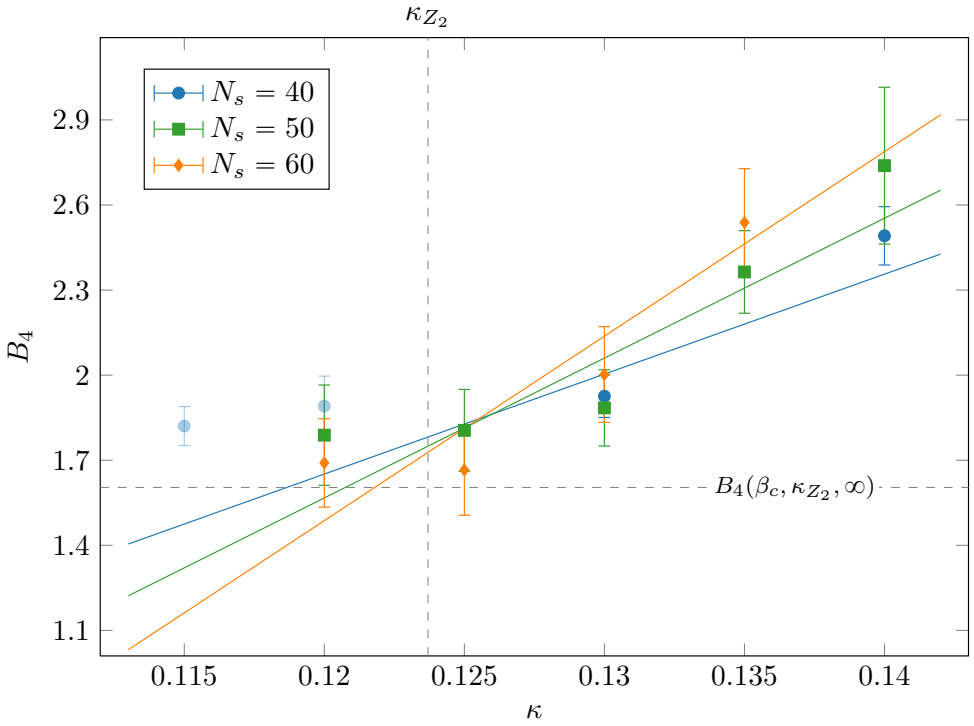

Figure 5.10: Taken from [94]. Final B_4 fit for $N_\tau = 10$. Depicted is fit i.10.1, which is marked with a blue background in Figure 5.9. The shaded points have been excluded from the fit.

$N_\tau = 12$

The simulations for $N_\tau = 12$ were started in the scope of this work with the help of Alessandro Sciarra and Francesca Cuteri, who also ran simulations due to the constraints on the number of computation nodes that could be used by one person on the clusters. The simulations could not be finished though because of the high computational effort. At least the existing simulations need to be brought to higher statistics, also simulations at more κ values for the already simulated N_s should be run to reasonably corner κ_{Z_2}. These results are therefore preliminary and the fit quality is not at the desired level yet, indicators being the low number of degrees of freedom over all fits and the precision of only three digits for all resulting κ_{Z_2} values. From Figure 5.12 one can see that our preliminary result for $N_\tau = 12$ is $\kappa_{Z_2}(N_\tau = 10) = 0.124(7)$, which is also depicted at Figure 5.11.

In the first fits, e.12.1 and i.12.1, points were excluded solely on the basis of data quality, excluding $N_\mathrm{s} = 36$ and $N_\mathrm{s} = 48$, which we could not do in the subsequent fits, because not enough points to be fit would have been left over in that case. The

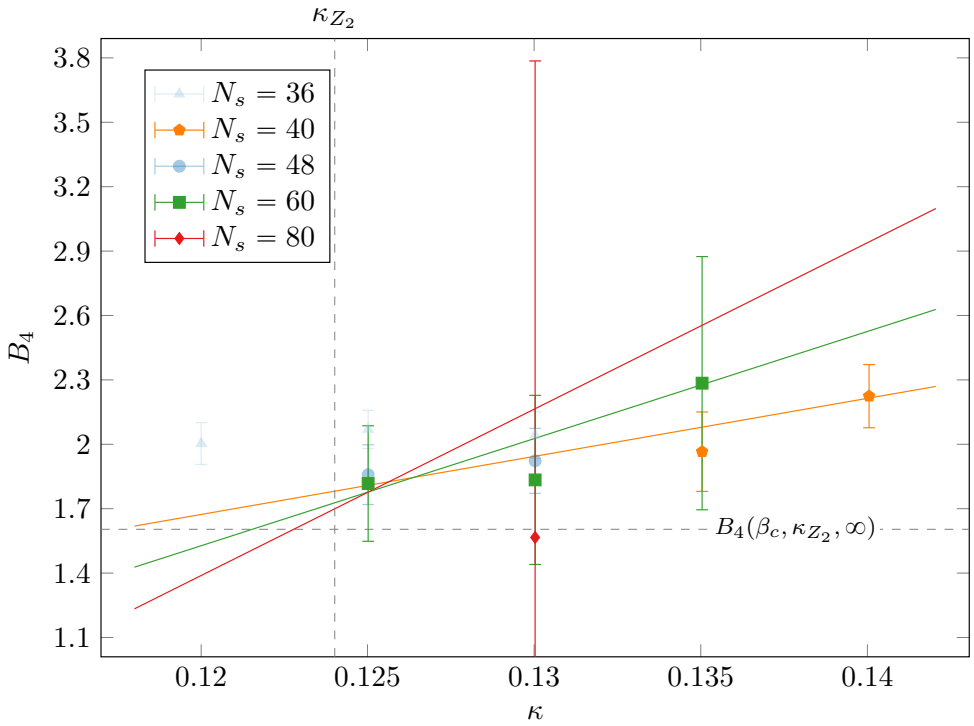

Figure 5.11: Final B_4 fit for $N_\tau = 12$. Depicted is fit i.12.1, which is marked with a blue background in Figure 5.12. The shaded points have been excluded from the fit.

resulting κ_{Z_2} are quite close to each other, B also being compatible with zero. The fit quality is not the best though.

The second fits, e.12.2 and i.12.2, only exclude the smallest volume $N_\mathrm{s} = 36$. The two κ_{Z_2} values differ a great amount, but B is still compatible with zero and the fit quality is comparable to the first fits.

In the third fits, e.12.3 and i.12.3, we only excluded $\kappa = 0.12$ and $\kappa = 0.125$ for $N_\mathrm{s} = 36$. Here, the resulting κ_{Z_2} differ even more than in the second fit, nearly spanning a the range 0.01, which is nearly as large as the difference between $\kappa_{Z_2}(N_\tau = 8)$ and $\kappa_{Z_2}(N_\tau = 10)$. B is also not compatible with zero, the overall fit quality is not worse than for the other fits though.

The last fits, e.12.4 and i.12.4, excluded all of $N_\mathrm{s} = 36$ and $\kappa = 0.135$ for $N_\mathrm{s} = 40$, so completely following the main strategy of excluding the smallest physical volumes. The κ_{Z_2} differ a lot again, but B is compatible with zero again. The fit quality is also comparable to the other fits.

It is evident that the inclusion of the correction term has a large effect on the resulting κ_{Z_2}, differing a lot from the results of the linear fits. Because of this, and because we also decided for the fit including the correction term for $N_\tau = 10$, where the situation was still better than here, we also opt for a fit including the correction term as a final result. All fits are not to be trusted, because we possibly would need to include one data point at $\kappa = 0.12$ to have a point reliably in the first order region, which was not possible. In the end, we chose the first fit, depicted in Figure 5.11,

because there, both results are at least somewhat close to each other, indicating a better fit quality than for the other fits.

Fit label	Included/Excluded κ per N_s	κ_{Z_2}	a_1	B	$\chi^2_{\text{d.o.f}}$	NDF	Q[%]
$e.12.1$	0.12 0.125 0.13 0.135 0.14 36 ✗ ✗ ✗ 40 ✓ ✓ 48 ✗ ✗ 60 ✓ ✓ ✓ 80 ✓	0.123(4)	0.10(4)	–	0.17	4	95
$i.12.1$		0.124(7)	0.07(8)	3(8)	0.19	3	90
$e.12.2$	0.12 0.125 0.13 0.135 0.14 36 ✗ ✗ ✗ 40 ✓ ✓ 48 ✓ ✓ 60 ✓ ✓ ✓ 80 ✓	0.120(4)	0.08(3)	–	0.24	6	96
$i.12.2$		0.125(10)	0.05(4)	5(6)	0.16	5	98
$e.12.3$	0.12 0.125 0.13 0.135 0.14 36 ✗ ✗ ✓ 40 ✓ ✓ 48 ✓ ✓ 60 ✓ ✓ ✓ 80 ✓	0.119(4)	0.08(3)	–	0.66	7	71
$i.12.3$		0.128(9)	0.04(3)	6(3)	0.14	6	99
$e.12.4$	0.12 0.125 0.13 0.135 0.14 36 ✗ ✗ ✗ 40 ✗ ✓ 48 ✓ ✓ 60 ✓ ✓ ✓ 80 ✓	0.121(4)	0.08(3)	–	0.27	5	93
$i.12.4$		0.128(13)	0.04(4)	6(7)	0.09	4	99

Figure 5.12: Overview over the results of the final fits, presenting the effect of excluding different data points for $N_\tau = 12$. The labelling of the fits takes the form $x.y.z$. x describes the fit ansatz, taking the values $x = e$ for fits according to Eq. (5.4), leading to $B =$ " $-$ ", which *exclude* the correction term, and $x = i$ when the correction term is *included*, performing the fits according to Eq. (5.5). y shows the value of N_τ. z is counting, and therefore distinguishing, the different fits. $z = 1$ represents the best fit we chose as the final one, which is also indicated by the blue background. The second column contains subtables which show the exclusion pattern of the data points. For every κ (columns) at the different N_s values (rows) it is marked, which points have been included (✓) or excluded (✗). A gray cells shows that at this point, no simulation was performed.

5.2.3 Lattice Spacing and Pion Masses

The last step is now to calculate the physical mass and lattice spacing for these masses to plot the critical mass as a function of the lattice spacing. This is shown in Figure 5.13. For $N_\tau = 12$, we did not precisely measure κ_{Z_2} and therefore only included $\kappa = 0.125$ in Figure 5.13, because we don't have a clear result for κ_{Z_2} yet, the precision of the result is not even up to our standards. Also, the mass simulations for $N_\tau = 12$ were taking quite a long time, so it was hard to justify using so many resources for a very much preliminary result.

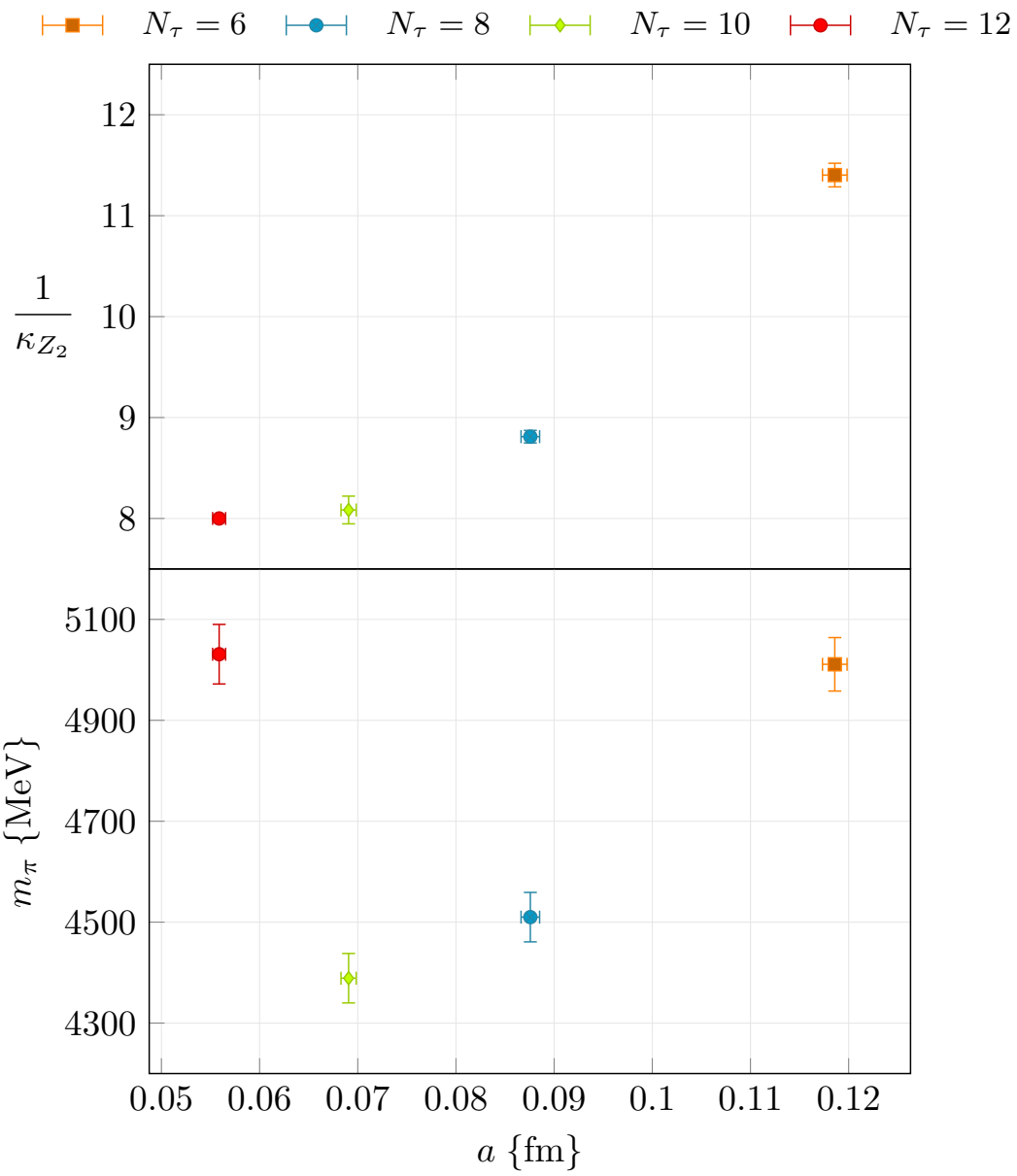

Figure 5.13: Taken from [94]. Top: The four κ_{Z_2} at the different lattice spacings. Bottom: The four pion masses corresponding to the κ_{Z_2}.

N_τ	κ	β_c	$a\,m_\pi$	$a\,\{\text{fm}\}$	$m_\pi\,\{\text{GeV}\}$	$T_c\,\{\text{MeV}\}$
6	0.075	5.8893	3.4722(2)	0.1181(12)	5.80(6)	279(3)
	0.085	5.8845	3.1073(2)	0.1185(12)	5.17(5)	277(3)
	0.0877	5.8821	3.0111(2)	0.1186(13)	5.01(5)	277(3)
	0.09	5.8798	2.9306(2)	0.1191(13)	4.86(5)	276(3)
	0.1	5.8676	2.5810(2)	0.1203(13)	4.24(4)	273(3)
	0.11	5.8462	2.2383(2)	0.1232(14)	3.58(4)	267(3)
8	0.11	6.0306	2.1298(2)	0.0872(9)	4.82(5)	283(3)
	0.1135	6.0222	2.0017(2)	0.0876(9)	4.51(5)	282(3)
	0.115	6.0180	1.9471(2)	0.0887(9)	4.33(5)	278(3)
	0.12	6.0009	1.7645(2)	0.0893(10)	3.90(4)	276(3)
	0.125	5.9776	1.5814(2)	0.0906(10)	3.44(4)	272(3)
	0.13	5.9464	1.3996(3)	0.0926(10)	2.98(3)	266(3)
	0.135	5.9026	1.2212(3)	0.0953(10)	2.53(3)	259(3)
10	0.115	6.1682	1.8724(2)	0.0680(8)	5.43(6)	290(3)
	0.12	6.1543	1.6802(2)	0.0688(8)	4.82(5)	287(3)
	0.1237	6.1414	1.5361(2)	0.0691(8)	4.39(5)	286(3)
	0.125	6.1356	1.4858(2)	0.0694(8)	4.23(5)	284(3)
	0.13	6.1027	1.2930(2)	0.0712(8)	3.58(4)	277(3)
	0.135	6.0576	1.0999(4)	0.0720(8)	3.01(3)	274(3)
	0.14	5.9902	0.9143(4)	0.0761(8)	2.37(3)	259(3)
12	0.125	6.2603	1.4247(2)	0.0559(7)	5.03(6)	294(3)
	0.13	6.2367	1.2189(3)	0.0551(7)	4.37(6)	299(4)

Table 5.1: Taken from [94]. Results of the simulations performed for the pion mass and scale setting procedure, all simulations took place on 32×16^3 lattices. For $N_\tau = \{6, 8, 10\}$, 800 independent configurations were obtained, whereas for $N_\tau = 12$ we obtained 1600 independent configurations. For a more complete overview, we also included the results for β_c, T_c, a and m_π in this table. β_c for κ_{Z_2} was obtained via an interpolation of the β_c values for the simulated κ at each N_τ. For $N_\tau = 12$, the simulations are not complete yet. Therefore, we only performed the pion mass and scale setting simulations for selected κ values. Also, κ_{Z_2} is still not known yet, but we marked $\kappa = 0.125$ in light gray, because it looks close to the real one from both the simulations and, as we see in 5.3.3, the Landau analysis.

Table 5.1 shows the different κ values, including κ_{Z_2}, β_c for each κ, the pion mass am_π on the lattice, as well as the lattice spacing a and the pion mass m_π in physical units. It also shows the critical temperature T_c for each κ, which, for the critical mass κ_{Z_2}, rises with N_τ over all four N_τ. This can also be observed with staggered fermions [101].

From Figure 5.13 and Table 5.1, one can see that the pion mass for $N_\tau = 12$ at

$\kappa = 0.125$, around the suspected κ_{Z_2}, is still high in contrast to the other N_τ. One would expect the pion mass at κ_{Z_2} to drop with increasing N_τ, but this is not the case here, even though $\kappa = 0.125$ is a bit higher than our resulting $\kappa_{Z_2} = 0.124$, meaning that either this pattern is changing, making it important to calculate the mass at a β_c obtained from higher N_s, to have a result closer to the thermodynamic limit, or this could also mean that κ_{Z_2} is not concluded yet, making it unnecessary to calculate the pion mass at a more precise κ. The need for more simulations at higher N_s before concluding on $N_\tau = 12$ also is apparent from Table A.1, where one can see that for $\kappa = 0.125$, β_c is changing in a very unusual, non-monotonic pattern between the different volumes, indicating a need for simulations at higher aspect ratios to conclude reliably on β_c, which would then lead to a better estimate of the pion mass, since they only depend on κ and $\beta_c(\kappa, N_\tau)$, making them very sensitive to β_c.

The mass calculations themselves were not as good as we would have hoped for, the plateau was barely visible in most of them, the situation worsening with increasing N_τ. For $N_\tau = 6$, $\kappa = 0.9$ we performed one simulation at $N_\tau = 64$ instead of $N_\tau = 32$ to test if more steps would increase the plateau, but the calculation runs into problems with the numerical precision of the calculated correlators, rendering the results useless after a certain point. To find the plateau more indirectly, we tried using different fitting functions, like a multi-exponential fit, but the fits were generally overfitted and ran into local solutions, leading to worse results as with using the last two points of the fit as the plateau.

The upper figure of Figure 5.13 depicts the inverse of our final results for κ_{Z_2} as a function of the lattice spacing, the lower figure shows the same but instead of the inverse of κ_{Z_2}. It depicts the pion mass, leading to a result that gives feeling for the physical scales involved and is comparable with other approaches. Both figures are a bit skewed by the inclusion of $\kappa_{Z_2} = 0.125$ for $N_\tau = 12$. For the upper figure, one would expect 8 as the continuum result, because of $\kappa = \frac{1}{2am+4}$. The inclusion of $N_\tau = 12$ indicates a closeness to this value that is not well-founded. $\kappa_{Z_2}(N_\tau = 12)$ might turn out to be smaller than $\kappa_{Z_2} = 0.125$, distancing it from the continuum value of 8. Even if this is the case, κ_{Z_2} might approach $\kappa_{Z_2}(a = 0)$ non-linearly, dropping below 8 at some N_τ, approaching the continuum limit from below. The lower figure might be skewed by the unusual high value for $m_\pi(N_\tau = 12)$, surpassing even $m_\pi(N_\tau = 6)$, going against the trend of the fully simulated N_τ. Comparing our results up to $N_\tau = 10$ with [81], p. 120 shows, that a similar effect was observable when $N_\tau = 10$ was in a preliminary stage, there $m_\pi = 4.5\,\mathrm{GeV}$, and here $m_\pi = 4.4\,\mathrm{GeV}$, even though in this work, κ_{Z_2} is estimated higher than in [81], which should lead to a higher m_π. It is not clear where the effect stems from, it might be related to the simulations at higher N_s, potentially leading to a more precise measurement of β_c, which has a huge impact on the mass calculations. This is a good sign regarding $N_\tau = 12$, since we expect to simulate at higher N_s and also that κ_{Z_2} will be lower than $\kappa = 0.125$, for which we calculated the mass.

Another difficulty with the overall results is, that strong cut-off effects are apparent from Figure 5.13, since the behaviour of the masses is non-linear. Since the critical mass on the lattice contains additional, polynomial error terms which depend on the lattice spacing, see Eq. (4.28), a smaller lattice spacing a leads to a

more linear behaviour of the masses.

Also, the results for the pion mass are not necessarily reliable, because $am_\pi > 1$ everywhere close to κ_{Z_2}, even for $N_\tau = 12$, meaning the pion mass is too large to be extracted in a meaningful way, which is also described as "the pion falling through the lattice", which happens because the spatial extent of the pion is smaller than the lattice spacing. This might be circumvented with heavy quark effective theory methods [102], though.

Our results are consistent with results obtained from staggered fermions [103] though, albeit only $N_\tau = 8$ was fully simulated there, resulting at approximately $m_\pi^{Z_2} \in [3.82, 4.48]$ GeV.

Overall, it is obvious that at least $N_\tau = 12$ needs to be completed, and possibly even $N_\tau = 14$ or more finer lattices need to be simulated, before the continuum extrapolation can be achieved. Excluding the unfinished $N_\tau = 12$, it is at least apparent that the critical pion mass is significantly reducing when increasing N_τ. An attempted linear extrapolation from the last two points at $N_\tau = 8$ and $N_\tau = 10$ leads to approximately 4 GeV. The remaining systematic error can be estimated as $\approx 20\%$ using double the shift to the extrapolated value.

5.3 Finding κ_{Z_2} via Landau Theory

To gain an even deeper understanding of the dynamics of the deconfinement transition, we want to describe its phase boundary through a Landau functional. Ultimately, we want to find out if it is possible to find the critical mass separating the first order phase transition from the crossover transition with help of this Landau functional for finer lattice spacings than the simulated ones we already obtained.

Here, we only lay the foundation for this though. The scope of this section is to see if it is possible to find a Landau theory for every N_τ and to show that it is possible to confirm the results for the critical mass κ_{Z_2} from the finite size scaling analysis using this Landau theory.

5.3.1 Building the Landau Functional

Our goal is to find a Landau functional to describe the phase boundary, which is shown exemplary for our data points at $N_\tau = 6$ in Figure 5.14.

The Landau functional we want to build has to contain the information on the location of κ_{Z_2} by construction. We therefore want to investigate if it is possible to extract κ_{Z_2} from our simulation data through Landau theory. It is also of interest to investigate if this can be done for higher N_τ, where we don't have found κ_{Z_2} yet.

To start constructing $\mathcal{L}$, we have to keep in mind how the phase boundary is structured. In our data, we have one or two points in the first order phase, below κ_{Z_2}. At κ_{Z_2}, the critical end point is a second order transition. We don't have simulation data at this value. Above κ_{Z_2}, where most of our simulated data falls, the phase transition is a crossover, which isn't usually treated with classical Landau theory and which we also won't include in our Landau functional. Therefore, we want to concentrate our efforts on the leftmost points. One would expect though,

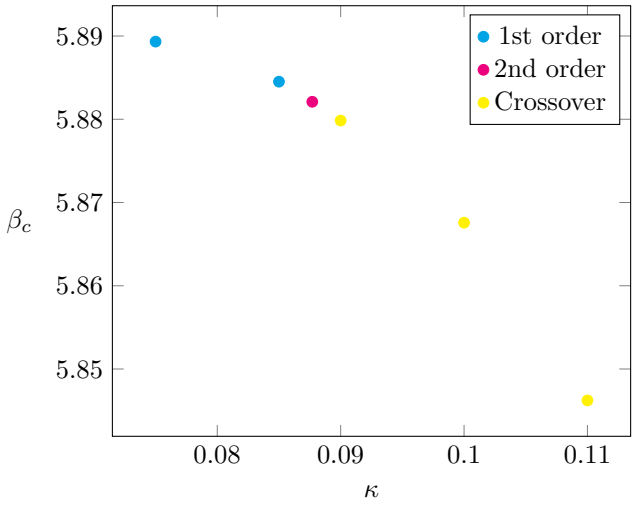

Figure 5.14: Depicted is β_c depending on κ at $N_\tau = 6$. β_{Z_2}, the point at the second order endpoint, has been interpolated and not simulated like the other points.

that at the critical temperature of a crossover, the Landau functional will have a simple minimum, that is not flat as in the second order phase transition.

The first challenge is to construct $\mathcal{L}$ in a way that it can describe a first order and a second order phase transition in equal measure.

Therefore, we start with a Landau functional for a first order phase transition. Since the centre symmetry is explicitly broken by dynamical fermions, we also include a symmetry breaking field $H = (2\kappa)^{N_\tau}$ into $\mathcal{L}$:

$$\mathcal{L} = a_2(\beta,\kappa)\eta^2 + a_3(\beta,\kappa)\eta^3 + a_4(\beta,\kappa)\eta^4 - H\eta. \tag{5.6}$$

We replaced the temperature T with the inverse lattice gauge coupling β to make $\mathcal{L}$ conform with our theory. We also included the hopping parameter κ so that we have a Landau functional for the phase boundary and not only for one mass.

The order parameter is linked to the Polyakov loop L and takes the form:

$$\boldsymbol{\eta} = L + L^* = 2\mathrm{Re}(L);\ \boldsymbol{\eta^2} = LL^* = |L|^2;\ \boldsymbol{\eta^3} = L^3 + L^{*3};\ \boldsymbol{\eta^4} = L^2L^{*2} = |L|^4. \tag{5.7}$$

The next step is to define the coefficients a_i. To take care of the dependence on κ and β, we expand them in both variables, which is analogous to the derivation in [104]:

$$a_i(\beta,\kappa) = a_i^0 + a_i^\beta \frac{\beta - \beta_{Z_2}}{\beta_{Z_2}} + a_i^\kappa \frac{\kappa - \kappa_{Z_2}}{\kappa_{Z_2}}. \tag{5.8}$$

We then need to think about which of these nine terms should be kept and which need to be zero.

We know from Section 4.2 that at $\kappa = \kappa_{Z_2},\ \beta = \beta_{Z_2}$, the second order endpoint, the Landau functional needs to have the form

$$\mathcal{L} = a_4^0\eta^4 - H\eta. \tag{5.9}$$

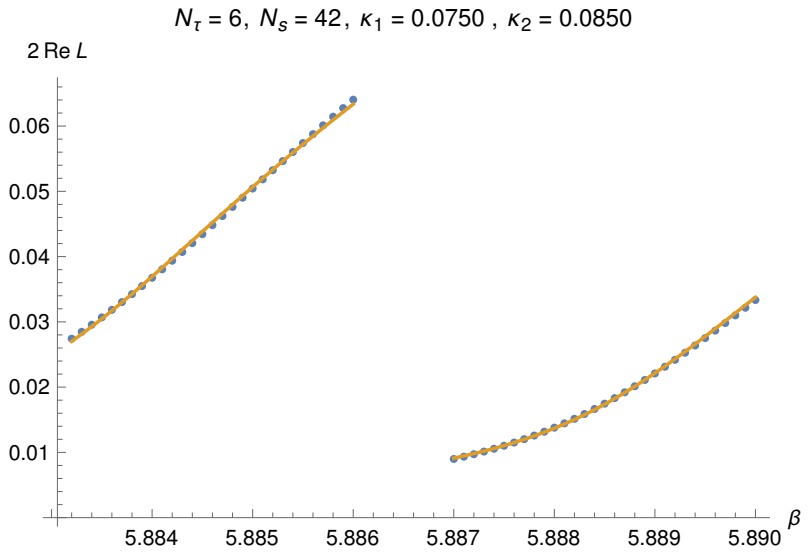

Figure 5.15: Fitting for the Landau coefficients and κ_{Z_2} at $N_\tau = 6$, $N_\mathrm{s} = 42$, $\kappa = 0.0750$ and $\kappa = 0.0850$. The variables that are fitted for are the coefficients a_2^β, a_2^κ, a_3^κ, a_4^0 and κ.

From this, we can trivially conclude that $a_2^0 = a_3^0 = 0$ and $a_4^0 \neq 0$.

We can also make the same assumption as in Section 4.2 and set $a_4^\beta = 0$, because the temperature dependence won't have a large impact close to β_{Z_2}.

It is not clear though, if it is also feasible to assume $a_3^\beta = 0$ and $a_4^\kappa = 0$, we therefore investigated both possibilities, $a_3^\beta = 0$; $a_4^\kappa = 0$ and $a_3^\beta \neq 0$; $a_4^\kappa \neq 0$.

This leaves us with two possibilities for the Landau functional:

$$\mathcal{L}_{short} = \left(a_2^\beta \frac{\beta - \beta_{Z_2}}{\beta_{Z_2}} + a_2^\kappa \frac{\kappa - \kappa_{Z_2}}{\kappa_{Z_2}}\right)\eta^2 + \left(a_3^\kappa \frac{\kappa - \kappa_{Z_2}}{\kappa_{Z_2}}\right)\eta^3 + a_4^0\eta^4 - H\eta \tag{5.10}$$

and

$$\begin{aligned}\mathcal{L}_{long} = &\left(a_2^\beta \frac{\beta - \beta_{Z_2}}{\beta_{Z_2}} + a_2^\kappa \frac{\kappa - \kappa_{Z_2}}{\kappa_{Z_2}}\right)\eta^2 + \left(a_3^\beta \frac{\beta - \beta_{Z_2}}{\beta_{Z_2}} + a_3^\kappa \frac{\kappa - \kappa_{Z_2}}{\kappa_{Z_2}}\right)\eta^3 \\ &+ \left(a_4^0 + a_4^\kappa \frac{\kappa - \kappa_{Z_2}}{\kappa_{Z_2}}\right)\eta^4 - H\eta.\end{aligned} \tag{5.11}$$

Be aware, that with the long Landau functional, the result should be a mix between the $a_3 < 0$ and $a_3 > 0$ plot, because we introduced a temperature dependence here, which leads to a switch of the behaviour at a certain temperature.

5.3.2 Fitting the Landau Functional

Now that we have our Landau theory, it is time to relate it to our data.

From our simulations, we have the data for the real part of the Polyakov loop $\mathrm{Re}(L)$. Referring to (5.7), we can see that we thus should be able to connect our simulation data with our Landau theory through the order parameter.

Since we only have the data at two or three values of β, we used reweighting to add more points, with a step size of 0.0001. This data of $\mathrm{Re}(L)$ then only needs to be multiplied by two in order to correspond to the order parameter of our Landau theory (5.7).

We know from Section 4.2, that the physical state of the system is described through a global minimum of $\mathcal{L}$:

$$\frac{\partial \mathcal{L}}{\partial \eta} = 0. \tag{5.12}$$

This equation can be solved for η, as it was done in (4.20) and (4.24). Since $\eta = 2\mathrm{Re}(L)$, we can then relate this to our data.

Solving (5.12) for our Landau functional is far from trivial, because it is a cubic equation. Hence, we used Mathematica to solve this equation and fit for κ_{Z_2}.

We receive an expression for $\eta(\beta, \beta_{Z_2} = \beta_{\mathrm{c}}(\kappa_{Z_2}), \kappa, \kappa_{Z_2}, \{a_i^x\})$, where κ is fixed from our simulation data, β will be the x-value of the fit and the coefficients a_i^x and κ_{Z_2} will be obtained from the fit.

Since β_{Z_2} and κ_{Z_2} are connected to each other, as can be seen in Figure 5.14, we want to express β_{Z_2} in terms of κ_{Z_2}, so we only have to fit for κ_{Z_2} and not for β_{Z_2}, in order to avoid fitting for heavily correlated coefficients. To do this, we perform a polynomial fit for the $\beta_{\mathrm{c}}(\kappa_{Z_2})$ data, which leads to the following fit functions for the different N_τ:

$$\beta_{c;N_\tau=6}(\kappa_{Z_2}) = 6.05751 - 6.61346\kappa_{Z_2} + 91.7678\kappa_{Z_2}^2 - 446.404\kappa_{Z_2}^3, \tag{5.13}$$
$$\beta_{c;N_\tau=8}(\kappa_{Z_2}) = 8.55088 - 70.6240\kappa_{Z_2} + 679.051\kappa_{Z_2}^2 - 2230.00\kappa_{Z_2}^3, \tag{5.14}$$
$$\beta_{c;N_\tau=10}(\kappa_{Z_2}) = 15.7286 - 250.052\kappa_{Z_2} + 2196.71\kappa_{Z_2}^2 - 6482.00\kappa_{Z_2}^3, \tag{5.15}$$
$$\beta_{c;N_\tau=12}(\kappa_{Z_2}) = 2.56896 + 35.9185\kappa_{Z_2} + 153.095\kappa_{Z_2}^2 - 1633.58\kappa_{Z_2}^3. \tag{5.16}$$

We performed this polynomial fit for β_{c} only for the data of the highest N_{s}, only for $N_\tau = 10$ we used $N_{\mathrm{s}} = 50$, because the data points are of a better quality than for $N_{\mathrm{s}} = 60$. Since we assume that we are in the infinite volume limit, the N_{s} dependence of the $\beta_{\mathrm{c}}(\kappa)$ data should not matter, even though we fit for multiple N_{s} in our $\eta(\beta)$ fits.

With an expression for β_{Z_2} at hand, we can fit for our order parameter η. Fitting the data points is not the easiest task. The fits depend very much on the initial values of the fit parameters, which can make it hard to even find a good fit.

One way we try to solve this is fitting for multiple κ values at once. An example of such a fit can be found in Figure 5.15. It shows how we are scanning through the phase boundary.

For all our fits, we only fit combinations of the three leftmost κ values, because we are still fitting to a first order Landau functional and we therefore try to stay as close as possible to the first order phase with the κ values we fit for. We also include a combination of three and not only two κ values, to make sure that the results are stable. Because of the way our simulations where set up regarding the ranges in the first order and crossover region, this means that we definitely include at least one, if not two, points in the crossover region in our fits.

Fitting with the two rightmost κ values also gives us an idea if this method would work when using data where we don't know the position of κ_{Z_2} from the

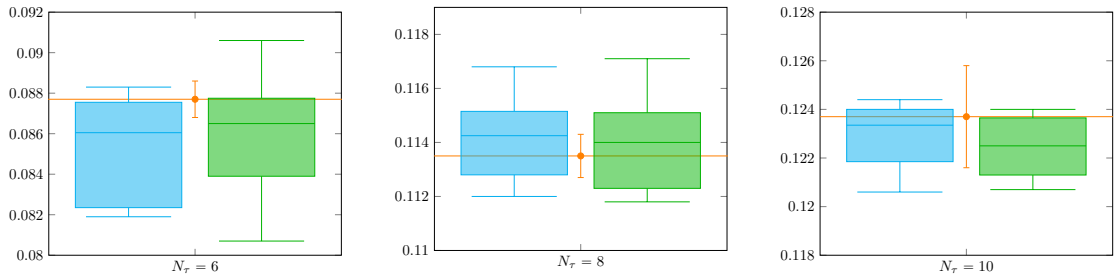

Figure 5.16: Boxplots for the Landau results. The orange data point in the middle is the result from the kurtosis analysis. The blue boxplot on the left side of each plot contains the κ_{Z_2} values from the *short* fits, the green boxplot on the right side of each plot contains the κ_{Z_2} values from the *long* fits.

kurtosis analysis yet, since there we might unknowingly use κ values farther away than expected from the first order phase to fit for κ_{Z_2}.

We also have a few conditions on what an acceptable fit is, even though these criteria are quite loose, since this is only a first exploratory study and not meant to give finalised results, so the fitting procedure is not refined enough yet for that purpose. Firstly, the relative error of κ_{Z_2} has to be smaller than 100% and a real number, to ensure that the fit itself is real. We also tried to keep the results close to the known values of κ_{Z_2} and close to each other, since our main goal is to find the Landau theory and not κ_{Z_2}, so it makes sense to focus on that first. Finally, we try to keep $\chi^2_{\text{d.o.f}} < 2$, which is already not optimal, but if this is not possible, we will still be using the fits. This was only the case for $N_\tau = 8$, $N_\text{s} = 48$ in the fit with three κ values, where we chose a fit with $\chi^2_{\text{d.o.f}} > 2$ that still provided results close to the other κ_{Z_2} values, since our main goal is to find the Landau theory around κ_{Z_2} and not necessarily κ_{Z_2} itself.

5.3.3 Results of the Landau Fits

The κ_{Z_2} results from the fits can be found in Table 5.2. The fit parameters referring to $\mathcal{L}_{short}$ have the subscript *short* and the fit parameters referring to $\mathcal{L}_{long}$ have the subscript *long*. In Table A.4, the other fit parameters for the $\mathcal{L}_{short}$-fit and in Table A.6, the other fit parameters of the $\mathcal{L}_{long}$-fit can be found. The corresponding initial values can be found in Table A.8. Table A.9 shows how many data points we cut off on the left and on the right of our data, in order to fit close enough to β_{Z_2}. This was not done in a systematic way, we just looked at the data and tried to keep the curve mostly linear.

When looking at the fits including three κ values, one has to keep in mind that it is hard to fit three κ-values at the same time and the curves almost never perfectly fit all of them.

One has to be very careful with all fits, because the model is a very complicated nonlinear fit model, which makes the fitting procedure very difficult and the results unreliable [105], especially since we found the fits by hand. Implementing a numeric way of finding the best initial values for the fits would have been too much work, since we only wanted to gain a first impression of the theory. The fits tend to

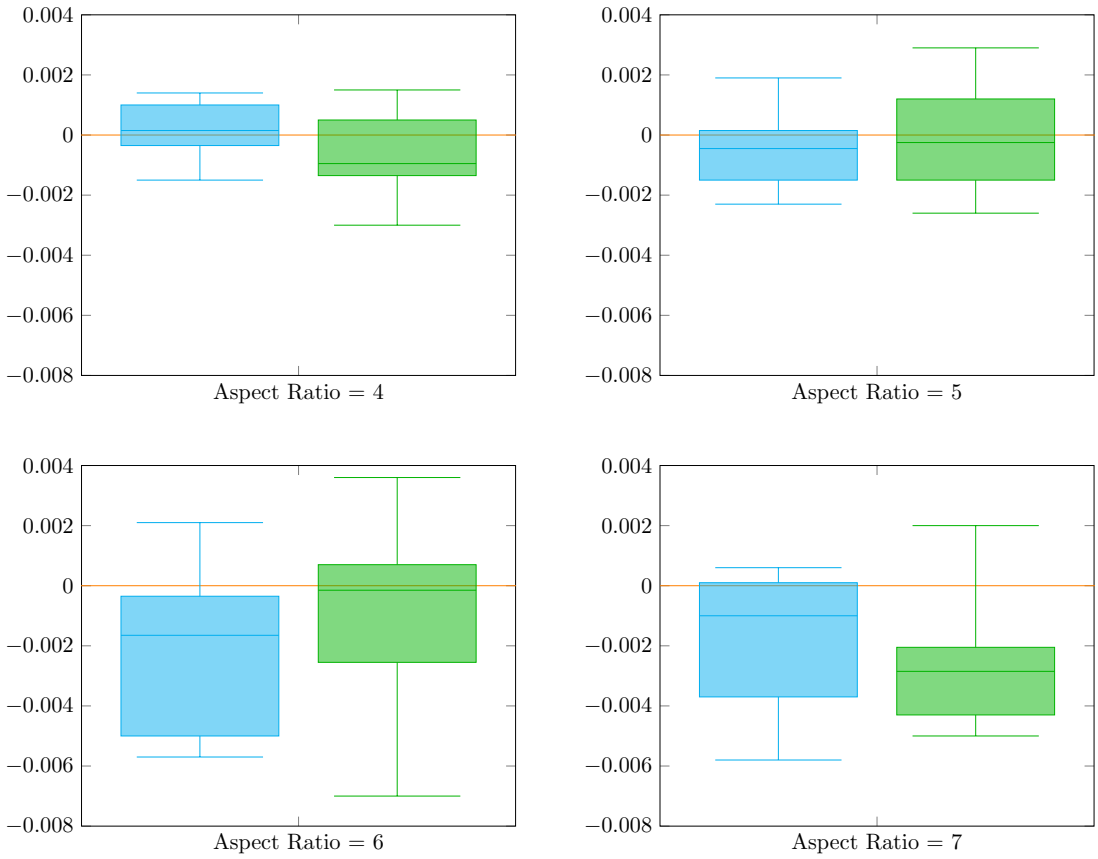

Figure 5.17: Boxplots for the Landau results. The orange line in the middle shows the relative critical mass $\kappa_{Z_2} - \kappa_{Z_2} = 0$. The blue boxplot on the left side of each plot contains the relative κ_{Z_2} values $\kappa_{Z_2;Landau} - \kappa_{Z_2}$ from the *short* fits, the green boxplot on the left side of each plot contains the same from the *long* fits. Aspect ratio 7 is included, but one should be careful, because there we only have four fit results, whereas for the other aspect ratios we had at least eight.

run into local minima, which don't necessarily give the right results. Therefore, we sometimes had to fit around those minima, which made the procedure even more difficult. This also means that these nonlinear fits give a rather rough idea of the true κ_{Z_2} instead of a reliable result. This is also complicated by us fitting into the crossover with a first order Landau functional.

In this discussion, we won't pay much attention to the fitting errors on κ_{Z_2}, since they are not meaningful when working with such a convoluted nonlinear model. It was very challenging to find appropriate fits and the errors where varying vastly, depending on the initial values given to the fit, even when the results where agreeing with each other. Therefore, there is always the possibility that a better fit than the one presented here exists, one which just reduces the error but does not change the result itself. This makes an analysis of the error meaningless. Also, expressing β_{Z_2} in terms of κ_{Z_2} gave another systematic error, that we can't really account for in a trivial manner.

As a first analysis of our results, we want to compare the results for κ_{Z_2} for the $\mathcal{L}_{short}$ and $\mathcal{L}_{long}$ fits to each other and to the kurtosis results. A good way to start with the comparison is to look at Figure 5.16 and Figure 5.17. There, we prepared the data in form of boxplots to show the distribution of the results for every N_τ and every aspect ratio.

From Figure 5.16, we can see that there are small differences between all three methods, but overall they seem to agree with each other well. For $N_\tau = 6$ and $N_\tau = 10$, the Landau fits give lower results than the kurtosis fits, but for $N_\tau = 8$, this trend is reversed. Since we only have three lattice spacings, we don't know yet in which direction these trends will evolve and if there even is a trend. But at least we can safely say, that in all three cases, the Landau fits give a good idea of κ_{Z_2}, independent of the included fit parameters.

In Figure 5.17, we can see that there is quite a huge difference for the two lower and the two higher aspect ratios. Aspect ratio 4 and 5 have a much smaller spread than aspect ratios 6 and 7. One has to keep in mind though, that for aspect ratio 7, there are only 4 values per box plot. When going to higher aspect ratios, there still is a trend for values for κ_{Z_2} lower than the ones from the simulations. This could be because of the quality of the data, that is better for lower aspect ratios since they are easier to simulate.

We can also compare the other fit parameters for the $\mathcal{L}_{short}$ and $\mathcal{L}_{long}$ fit in Table A.4 and Table A.6. In Table A.4 we see that the parameters are quite consistent with each other for each N_τ, especially a_2^β is distinct for every N_τ, and the errors are manageable. This indicates that there is a universal Landau functional for every N_τ, which is exactly what we wanted to find out. In Table A.6, the errors for the additional fit parameters not present in $\mathcal{L}_{short}$ are quite large, which hints at them being redundant. In general, the errors for $\mathcal{L}_{long}$ are larger, probably because the fit function is more complicated than $\mathcal{L}_{short}$, which increases the problems of the nonlinear fit even further, but also here, at least a_2^β, a_2^κ and a_4^0 are consistent within each N_τ.

This is an inconclusive answer to the question if $\mathcal{L}_{short}$ or $\mathcal{L}_{long}$ are the better fits. $\mathcal{L}_{short}$ possibly excludes parameters, that might be significant, but $\mathcal{L}_{long}$ has errors on these parameters, that are so big that any meaning is basically lost.

It is also important to keep in mind that the $\mathcal{L}_{long}$ fits are less reliable in general, because the nonlinear fit model is a much larger function, and the parameter space is bigger. This complicates finding the right input parameters and also makes the fits less reliable, because the probability of not having found the right set of input parameters is higher. Also, the time it takes Mathematica to find a fit is significantly increased for $\mathcal{L}_{long}$, fitting for $\mathcal{L}_{short}$ takes about 2 seconds, fitting for $\mathcal{L}_{long}$ takes about 10 seconds.

When looking at Table 5.2, we can also observe that the fits with two κ values in the crossover don't seem to be outliers. This shows that this Landau fitting method would indeed also work when we don't know if we already have sufficient data in the first order phase.

Also, across the different volumes the results are quite stable. This is good, since our method is built on the fact that this Landau theory should be volume independent.

We also see that for $N_\tau = 10$, $N_\mathrm{s} = 40$, the results don't deviate much from the other volumes, which means that fitting farther into the crossover is not affecting our results. But even though the results are fine, it was quite difficult to find a good fit, so it still makes more sense to fit closer to the first order region.

We also tried fitting for the one $N_\tau = 12$ volume that had three κ values simulated. We don't have a reliable kurtosis value yet to compare it to, but the results for κ_{Z_2} are stable. They are also in line with what we would expect from the theory, they give a result of $\kappa_{Z_2} \approx 0.125$, which is slightly higher as the result for $N_\tau = 10$ and also close to the continuum value of $1/8$.

As a final result, we decided on a Landau functional for every N_τ. To be on the safe side, we chose these from the fits of $\mathcal{L}_{long}$.

For $N_\tau = 6$, we chose $N_\mathrm{s} = 36$, $\kappa \in \{0.0850, 0.0900\}$, because the errors are acceptably small and the resulting κ_{Z_2} is close to the ones from our kurtosis results:

$$\begin{aligned}\mathcal{L} = &\left(-1.151\frac{\beta - \beta_{c;N_\tau=6}(\kappa_{Z_2})}{\beta_{c;N_\tau=6}(\kappa_{Z_2})} - 0.0086\frac{\kappa - \kappa_{Z_2}}{\kappa_{Z_2}}\right)\eta^2 \\ &+ \left(-3.6235\frac{\beta - \beta_{c;N_\tau=6}(\kappa_{Z_2})}{\beta_{c;N_\tau=6}(\kappa_{Z_2})} - 0.0875\frac{\kappa - \kappa_{Z_2}}{\kappa_{Z_2}}\right)\eta^3 \\ &+ \left(0.0747 + 0.2302\frac{\kappa - \kappa_{Z_2}}{\kappa_{Z_2}}\right)\eta^4 - H\eta, \\ &\text{with } \kappa_{Z_2} = 0.0876.\end{aligned} \tag{5.17}$$

Together with the general fit results, this seems to imply that fitting around κ_{Z_2} gives better results than fitting left from it.

For $N_\tau = 8$, we chose $N_\mathrm{s} = 48$, $\kappa \in \{0.1100, 0.1150\}$, because the errors are not too big, the resulting κ_{Z_2} is close to the one from the kurtosis fits and the values of

the parameters seem to agree with the ones from the other fits quite well:

$$\begin{aligned}\mathcal{L} = &\left(-0.259\frac{\beta-\beta_{c;N_\tau=8}(\kappa_{Z_2})}{\beta_{c;N_\tau=8}(\kappa_{Z_2})} - 0.0103\frac{\kappa-\kappa_{Z_2}}{\kappa_{Z_2}}\right)\eta^2 \\ &+\left(-1.8824\frac{\beta-\beta_{c;N_\tau=8}(\kappa_{Z_2})}{\beta_{c;N_\tau=8}(\kappa_{Z_2})} - 0.096\frac{\kappa-\kappa_{Z_2}}{\kappa_{Z_2}}\right)\eta^3 \\ &+\left(0.0649 - 0.406\frac{\kappa-\kappa_{Z_2}}{\kappa_{Z_2}}\right)\eta^4 - H\eta, \\ &\text{with } \kappa_{Z_2} = 0.1118.\end{aligned} \tag{5.18}$$

For $N_\tau = 10$, we picked $N_\mathrm{s} = 50$, $\kappa \in \{0.1200, 0.1250\}$, since the errors are quite manageable and the resulting κ_{Z_2} agrees well with the kurtosis results:

$$\begin{aligned}\mathcal{L} = &\left(-0.0429\frac{\beta-\beta_{c;N_\tau=10}(\kappa_{Z_2})}{\beta_{c;N_\tau=10}(\kappa_{Z_2})} - 0.0047\frac{\kappa-\kappa_{Z_2}}{\kappa_{Z_2}}\right)\eta^2 \\ &+\left(-0.9712\frac{\beta-\beta_{c;N_\tau=10}(\kappa_{Z_2})}{\beta_{c;N_\tau=10}(\kappa_{Z_2})} + 0.0414\frac{\kappa-\kappa_{Z_2}}{\kappa_{Z_2}}\right)\eta^3 \\ &+\left(0.0524 - 2.7433\frac{\kappa-\kappa_{Z_2}}{\kappa_{Z_2}}\right)\eta^4 - H\eta, \\ &\text{with } \kappa_{Z_2} = 0.1240.\end{aligned} \tag{5.19}$$

For $N_\tau = 12$, we went with the first fit, $N_\mathrm{s} = 60$, $\kappa \in \{0.1250, 0.1300\}$, because overall, it has the smallest errors:

$$\begin{aligned}\mathcal{L} = &\left(-0.0237\frac{\beta-\beta_{c;N_\tau=12}(\kappa_{Z_2})}{\beta_{c;N_\tau=12}(\kappa_{Z_2})} - 0.0019\frac{\kappa-\kappa_{Z_2}}{\kappa_{Z_2}}\right)\eta^2 \\ &+\left(0.3955\frac{\beta-\beta_{c;N_\tau=12}(\kappa_{Z_2})}{\beta_{c;N_\tau=12}(\kappa_{Z_2})} + 0.0171\frac{\kappa-\kappa_{Z_2}}{\kappa_{Z_2}}\right)\eta^3 \\ &+\left(0.0207 + 0.4584\frac{\kappa-\kappa_{Z_2}}{\kappa_{Z_2}}\right)\eta^4 - H\eta, \\ &\text{with } \kappa_{Z_2} = 0.1253.\end{aligned} \tag{5.20}$$

The fits we chose all have two κ values, where one lies below and one above the κ_{Z_2} of the kurtosis fits. We can't say if this is universally the best way to fit, because we only have the comparison with two κ values left of κ_{Z_2} for $N_\tau = 6$. For the higher N_τ, a fit with only κ values in the first order might actually be better than the ones presented here.

N_τ	N_s	κ	$\kappa_{Z_2;short}$	$\chi^2_{\mathrm{d.o.f.};short}$	$\kappa_{Z_2;long}$	$\chi^2_{\mathrm{d.o.f.};long}$
6	30	☒☒⊡⊡⊡	0.0873(30)	0.000590881	0.0906(528)	0.020416
		☒⊡☒⊡⊡	0.0878(50)	0.0873462	0.0873(243)	0.398461
		⊡☒☒⊡⊡	0.0860(35)	0.34348	0.0876(137)	0.316989
		☒☒☒⊡⊡	0.0879(250)	0.572294	0.0901(456)	0.87784
	36	☒☒⊡⊡⊡	0.0822(74)	0.927808	0.0837(4)	0.0000640453
		☒⊡☒⊡⊡	0.0825(194)	0.506639	0.0807(11)	0.0038755
		⊡☒☒⊡⊡	0.0829(77)	0.0242505	0.0876(64)	0.276001
		☒☒☒⊡⊡	0.0820(107)	0.586643	0.0879(125)	1.99035
	42	☒☒⊡⊡⊡	0.0819(11)	0.00294119	0.0827(60)	0.0765802
		☒⊡☒⊡⊡	0.0883(4)	0.141615	0.0857(9)	0.0335453
		⊡☒☒⊡⊡	0.0873(1)	0.00326232	0.0856(18)	0.0271225
		☒☒☒⊡⊡	0.0861(111)	1.85468	0.0841(61)	0.494297
8	32	☒☒⊡⊡⊡⊡	0.1120(2)	0.000788671	0.1147(516)	0.101184
		☒⊡☒⊡⊡⊡	0.1148(103)	0.507446	0.1127(457)	1.18984
		⊡☒☒⊡⊡⊡	0.1130(7)	0.0103985	0.1121(100)	0.00669614
		☒☒☒⊡⊡⊡	0.1149(56)	0.962328	0.1150(607)	1.727
	40	☒☒⊡⊡⊡⊡	0.1122(3)	0.0105107	0.1118(66)	0.0479916
		☒⊡☒⊡⊡⊡	0.1154(20)	0.00159767	0.1124(243)	0.326357
		⊡☒☒⊡⊡⊡	0.1136(5)	0.16532	0.1122(204)	1.36681
		☒☒☒⊡⊡⊡	0.1148(27)	0.912326	0.1156(553)	1.5785
	48	☒☒⊡⊡⊡⊡	0.1126(74)	0.0208512	0.1133(508)	1.89908
		☒⊡☒⊡⊡⊡	0.1161(163)	1.54038	0.1152(744)	0.596504
		⊡☒☒⊡⊡⊡	0.1168(40)	0.00599024	0.1171(2)	0.0000260156
		☒☒☒⊡⊡⊡	0.1137(90)	2.87684	0.1147(622)	3.25116
10	40	☒⊡☒⊡⊡	0.1239(7)	0.0227489	0.1224(25)	0.0112725
		☒⊡⊡⊡☒	0.1238(5)	0.0690237	0.1226(28)	0.146099
		⊡⊡☒⊡☒	0.1235(74)	1.02609	0.1207(589)	0.737169
		☒⊡☒⊡☒	0.1244(8)	1.38894	0.1235(86)	0.875312
	50	☒☒⊡⊡⊡	0.1216(20)	0.228477	0.1240(51)	0.0501684
		☒⊡☒⊡⊡	0.1214(3)	0.125637	0.1211(27)	0.236919
		⊡☒☒⊡⊡	0.1232(13)	0.30683	0.1238(127)	0.175648
		☒☒☒⊡⊡	0.1232(17)	0.664311	0.1218(255)	0.624173
	60	☒☒⊡⊡⊡	0.1241(4)	0.00477249	0.1239(18)	0.000459945
		☒⊡☒⊡⊡	0.1206(8)	0.176576	0.1208(26)	0.0524975
		⊡☒☒⊡⊡	0.1242(7)	0.335761	0.1232(40)	0.336133
		☒☒☒⊡⊡	0.1221(30)	1.55676	0.1215(556)	1.62836
12	60	☒☒⊡	0.1247(2)	0.117196	0.1253(9)	0.090581
		☒⊡☒	0.1249(3)	0.260342	0.1248(31)	0.324404
		⊡☒☒	0.1253(22)	0.482507	0.1255(82)	0.191897
		☒☒☒	0.1246(14)	0.851503	0.1248(67)	0.70272

Table 5.2: Fit results. The subscripts show if the variable refers to fits over $\mathcal{L}_{short}$ or $\mathcal{L}_{long}$. The boxes refer to the different κ values for every N_τ, cf. Table A.9. ☒ means this κ is included in the fit, ⊡ means this κ is excluded from the fit. The reference values from the kurtosis fits are: $\kappa_{Z_2;N_\tau=6} = 0.0877$, $\kappa_{Z_2;N_\tau=8} = 0.1135$, $\kappa_{Z_2;N_\tau=10} = 0.1237$, $\kappa_{Z_2;N_\tau=12}$ is still unknown. For additional information on the fits refer to Table A.8 and Table A.9.

Chapter 6

Conclusions and Outlook

The purpose of this thesis was to get closer to determining the continuum value for the mass at the Z_2 deconfinement transition in the heavy corner of the Columbia plot at $N_\mathrm{f} = 2$. This is of interest, because it gives insights into the mechanics of the deconfinement transition, creating a connection between the critical heavy quark mass and the latent heat of the first-order pure-gauge transition. These studies can also be used to provide a test for functional renormalisation group (FRG) studies at large quark masses, because they give, in a different parameter region, a benchmark for them. Perspectively, we hope the Landau study will help us gain an even deeper understanding of the dynamics of the deconfinement transition, possibly predicting quantities like the latent heat and the approximate size of the scaling region around κ_{Z_2}.

We approached this using two different methods, both based on Hybrid Monte Carlo simulations with Wilson fermions. These simulations were carried out at progressively finer lattices at $N_\tau = \{6, 8, 10, 12\}$ in the heavy quark corner of the Columbia plot for $N_\mathrm{f} = 2$.

The first method was the usage of the standardised moments skewness and kurtosis to determine κ_{Z_2} from the simulation data. We made progress there, getting a result for $N_\tau = 10$ and starting the simulations at $N_\tau = 12$, even though these are not finished yet. Ultimately, it is very likely though, that at least $N_\tau = 14$ needs to be simulated as well in order to reach a continuum limit. Our estimate for the continuum pion mass is, according to the simulations up to $N_\tau = 10$, a critical mass of about 4 GeV.

From the autocorrelation time analysis, we also learned a lot about the growing statistical requirements with increasing N_τ, giving an alarming perspective about the higher aspect ratios and increased statistics that need to be acquired to reach a sufficient quality of the data so that it can be effectively analysed using the standardised moments.

This makes clear that, in order to reach a continuum limit using this technique, it will be necessary to finish at least $N_\tau = 12$, and probably simulate $N_\tau = 14$ as well. We also ran into problems with the extraction of the pion mass, which should be solved somehow in order to get a reliable result for the continuum limit. Both of these problems might be avoided if a different parameter than the pion mass could be used to take the continuum limit, since this seems to be the limiting factor right

now.

The second method of using Landau theory to find κ_{Z_2} is still at its very beginnings. We started developing it in the hopes of finding an approach which needs less simulated data to reach the same conclusions as the standardised moments method. In this work, we showed that it is indeed possible to pin down κ_{Z_2} with Landau theory, as well as gained an understanding about the data needed for this analysis. We also compared two different fitting functions which each other, but did not reach a conclusion yet about if the shorter Landau functional would be enough to reach reliable results. The main issue we had with this method is the very complicated fit function, which lead to very sensitive fits that ran into local minima constantly and were prone to overfitting, which made the extraction of κ_{Z_2} quite difficult.

Overall, a lot of work needs to be done before this Landau method can be used instead of the kurtosis method to extract κ_{Z_2}. First of all, it would be helpful to automatise the extraction of the best fit, which wasn't really feasible here, since the parameters space is huge and this study only wanted to get a first impression of Landau theory in connection with our lattice studies. It will also be necessary to find a way to account for the systematic error that gets introduced by expressing β_{Z_2} in terms of κ_{Z_2}, making it possible to get meaningful errors out of the fits. Another important step is to refine the fitting function, concluding on the question if the *short* or *long* fit function is the better one, as well as reducing the dependency in the input values.

When all these problems are solved, it would be desirable to expand the Landau functional in the N_τ direction, so we could get an idea about κ_{Z_2} for not yet simulated N_τ, maybe even reaching a continuum limit this way.

Appendix A

Additional Content

A.1 Notations and Conventions

In this appendix, we want to give more details about the notations and conventions used throughout this thesis.

We use natural units where $c = \hbar = k_B = 1$, therefore giving all quantities units of eV. The following relation is used to convert the values of the quantities from natural units to standard units:

$$\hbar c = 197.3\,\mathrm{fm\,MeV}. \tag{A.1}$$

Another convention we use is the Euclidean space time

$$t_E = it_M, \tag{A.2}$$

which we arrive at by rotating the theory from Minkowski space via Wick rotation. This also changes the action to

$$S_M = iS_E. \tag{A.3}$$

In Euclidean space time, the metric does not have a relative minus sign between the time and space component, changing the metric tensor from $g_{\mu\nu} = \mathrm{diag}(1, -1, -1, -1)$ in Minkowski space time to $g_{\mu\nu} = \mathrm{diag}(1, 1, 1, 1)$ in Euclidean space time. This also changes the convention of naming the space time indices to $\{1, 2, 3, 4\}$, with $\{4\}$ the time direction and $\{1, 2, 3\}$ the spatial directions. There is also no distinction between covariant and contravariant indices anymore.

The gamma matrices γ_μ, with $\mu = 1, 2, 3, 4$, are also different in Euclidean space time:

$$\gamma_1 = -i\gamma_1^M,\ \gamma_2 = -i\gamma_2^M,\ \gamma_3 = -i\gamma_3^M,\ \gamma_4 = \gamma_0^M. \tag{A.4}$$

This also changes the commutation of the gamma matrices:

$$\{\gamma_\mu, \gamma_\nu\} = 2\delta_{\mu\nu}\mathbb{1}. \tag{A.5}$$

Following from this, γ_5 has to look different in order to still anti-commute with all γ_μ and obey $\gamma_5^2 = \mathbb{1}$:

$$\gamma_5 = \gamma_1\gamma_2\gamma_3\gamma_4. \tag{A.6}$$

For all gamma matrices γ_μ with $\mu = 1, \ldots, 5$, it also holds that:

$$\gamma_\mu = \gamma_\mu^\dagger = \gamma_\mu^{-1}. \tag{A.7}$$

A.2 Simulation Statistics

N_τ	κ	β_c | Total statistics per N_s | Number of simulated β values			
		Aspect ratio 4	Aspect ratio 5	Aspect ratio 6	Aspect ratio 7
6	0.075	–	5.88884 | 1.6M | 2	5.88895 | 1.6M | 2	5.88933 | 1.6M | 2
	0.085	–	5.88407 | 1.6M | 2	5.88448 | 1.6M | 2	5.88452 | 1.6M | 2
	0.09	–	5.88097 | 2.4M | 3	5.88104 | 2.4M | 3	5.87985 | 2.4M | 3
	0.1	–	5.86865 | 1.6M | 2	5.86762 | 1.6M | 2	5.86758 | 1.6M | 2
	0.11	–	5.84677 | 1.6M | 2	5.84624 | 2.4M | 3	5.84623 | 2.4M | 3
8	0.11	6.03018 | 2.4M | 3	6.03085 | 2.4M | 3	6.03064 | 2.4M | 3	6.03139 | 1.0M | 3
	0.115	6.01892 | 2.4M | 3	6.01891 | 2.4M | 3	6.01801 | 2.4M | 3	–
	0.12	6.00366 | 1.6M | 2	6.00208 | 2.4M | 3	6.00093 | 0.9M | 2	–
	0.125	5.98070 | 2.4M | 3	5.97888 | 2.2M | 3	5.97757 | 1.4M | 3	–
	0.13	5.94928 | 2.4M | 3	5.94705 | 2.4M | 3	5.94642 | 1.6M | 2	–
	0.135	5.90492 | 2.4M | 3	5.90257 | 2.4M | 3	–	–
10	0.115	6.16818 | 1.8M | 3	–	–	–
	0.12	6.15297 | 1.8M | 3	6.15408 | 1.8M | 3	6.15434 | 1.6M | 3	–
	0.125	–	6.13558 | 1.8M | 3	6.13558 | 1.2M | 2	–
	0.13	6.10685 | 1.8M | 3	6.10524 | 1.8M | 3	6.10269 | 1.2M | 2	–
	0.135	–	6.05851 | 1.8M | 3	6.05758 | 1.6M | 4	–
	0.14	5.99361 | 1.8M | 3	5.99022 | 1.8M | 3	–	–
		Aspect Ratio 3	Aspect Ratio $3\frac{1}{3}$	Aspect Ratio 4	Aspect Ratio 5
12	0.12	6.28327 | 1.6M | 4	–	–	–
	0.125	6.26036 | 1.1M | 3	–	6.26698 | 1.4M | 4	6.26034 | 1.8M | 3
	0.13	6.23527 | 0.9M | 4	–	6.23569 | 2.0M | 4	6.23670 | 1.8M | 3
	0.135	–	6.19650 | 1.2M | 3	–	6.18890 | 1.2M | 3
	0.14	–	6.12344 | 1.8M | 3	–	–

Table A.1: Partially taken from [94]. Overview over the statistics for $N_\tau \in \{6, 8, 10, 12\}$. For $N_\tau = 8$, $N_s = 80$, $\kappa = 0.115$, three different β values were simulated, resulting in $\beta_c = 6.01708$, with an overall statistics of 2.0M. For $N_\tau = 12$, $N_s = 80$, $\kappa = 0.13$, two different β values with two chains were simulated, leading to $\beta_c = 6.2375$, and have an overall statistics of 1.2M.

A.3 Autocorrelation Time

N_τ	κ	Average $\tau_{\text{int}}(B_3) \cdot 10^{-2}$ | Average number of independent events							
		Aspect ratio 4		Aspect ratio 5		Aspect ratio 6		Aspect ratio 7	
6	0.075	–		9.8(9)	437	18.2(2.0)	222	50(9)	95
	0.085	–		10.6(1.0)	397	24(3)	187	39(6)	104
	0.09	–		14.7(1.7)	381	24(3)	243	15.7(1.9)	351
	0.1	–		9.6(9)	437	11.3(1.1)	382	10.1(1.0)	432
	0.11	–		5.1(4)	790	5.07(29)	825	4.92(28)	864
8	0.11	10.0(8)	419	17.5(1.6)	239	32(4)	139	37(6)	45
	0.115	12.1(1.0)	343	17.9(1.7)	236	31(4)	146	–	
	0.12	9.6(8)	429	16.2(1.6)	271	15.2(2.2)	158	–	
	0.125	7.5(5)	550	8.9(7)	468	12.2(1.2)	202	–	
	0.13	5.7(3)	731	6.1(4)	683	5.9(4)	677	–	
	0.135	3.08(14)	1293	3.14(14)	1273	–		–	
10	0.115	12.1(1.1)	258	–		–		–	
	0.12	13.5(1.3)	233	30(4)	109	51(9)	65	–	
	0.125	–		20.9(2.3)	147	37(7)	87	–	
	0.13	13.5(1.3)	230	21.4(2.4)	147	21.1(2.8)	138	–	
	0.135	–		8.2(6)	379	8.9(7)	213	–	
	0.14	4.07(24)	765	3.85(22)	820	–		–	
		Aspect ratio 3		Aspect ratio $3\frac{1}{3}$		Aspect ratio 4		Aspect ratio 5	
12	0.12	7.3(5)	272	–		–		–	
	0.125	7.0(6)	267	–		16.3(1.8)	113	107(28)	21
	0.13	5.9(5)	202	–		12.0(1.3)	107	92(22)	24
	0.135	–		21.4(3.8)	70	–		24.7(4.7)	62
	0.14	–		17.0(2.8)	155	–		–	

Table A.2: Partially taken from [94]. This table depicts the average of the integrated autocorrelation time τ_{int} for the skewness, which was achieved by merging the chains at the simulated β. Additionally, it shows the average of the number of independent events, which was achieved in a similar way. For $N_\tau = 8$, $N_\text{s} = 80$, $\kappa = 0.115$, we have 104(20) | 45. For $N_\tau = 12$, $N_\text{s} = 80$, $\kappa = 0.13$, we have 97(32) | 45.

N_τ	κ	Average $\tau_{\text{int}}(B_4) \cdot 10^{-2}$ | Average number of independent events							
		Aspect ratio 4		Aspect ratio 5		Aspect ratio 6		Aspect ratio 7	
6	0.075	–		3.07(17)	1313	13.7(1.4)	292	31(4)	131
	0.085	–		3.42(22)	1293	15.3(1.9)	323	30(4)	139
	0.09	–		10.8(1.4)	792	20(3)	308	8.1(5)	499
	0.1	–		4.7(3)	857	8.3(7)	540	8.5(8)	524
	0.11	–		3.18(20)	1399	3.47(17)	1216	3.41(17)	1267
8	0.11	5.0(4)	1049	9.5(8)	507	20.7(2.7)	294	31(5)	53
	0.115	6.4(5)	845	12.8(1.2)	362	17.2(2.0)	331	–	
	0.12	3.59(20)	1105	7.8(6)	592	8.1(9)	281	–	
	0.125	3.86(21)	1116	4.96(29)	739	9.4(1.0)	288	–	
	0.13	3.12(17)	1508	3.81(20)	1128	3.61(21)	1102	–	
	0.135	1.74(6)	2381	2.05(8)	1945	–		–	
10	0.115	3.41(18)	892	–		–		–	
	0.12	5.6(4)	576	21(3)	215	28(4)	103	–	
	0.125	–		12.0(1.3)	307	21(3)	165	–	
	0.13	4.7(3)	722	13.4(1.5)	261	11.9(1.3)	244	–	
	0.135	–		5.0(3)	596	5.7(4)	336	–	
	0.14	2.20(10)	1393	2.17(10)	1429	–		–	
		Aspect ratio 3		Aspect ratio $3\frac{1}{3}$		Aspect ratio 4		Aspect ratio 5	
12	0.12	2.9(2)	869	–		–		–	
	0.125	2.0(1)	955	–		7.5(9)	313	80(23)	36
	0.13	1.9(1)	584	–		6.6(6)	192	35(6)	63
	0.135	–		8.6(1.1)	169	–		16.0(2.7)	100
	0.14	–		6.2(6)	383	–		–	

Table A.3: Partially taken from [94]. This table depicts the average of the integrated autocorrelation time τ_{int} for the kurtosis, which was achieved by merging the chains at the simulated β. Additionally, it shows the average of the number of independent events, which was achieved in a similar way. For $N_\tau = 8$, $N_\text{s} = 80$, $\kappa = 0.115$, we have 82(14) | 53. For $N_\tau = 12$, $N_\text{s} = 80$, $\kappa = 0.13$, we have 43(10) | 59.

A.4 Landau Results

N_τ	N_s	κ	a_2^β	a_2^κ	a_3^κ	a_4^0
6	30	☒☒⊡⊡⊡	-0.6251(241)	-0.0069(3)	-0.0374(135)	0.1165(168)
		☒⊡☒⊡⊡	-1.0532(1537)	-0.0099(23)	-0.0482(186)	0.0977(33)
		⊡☒☒⊡⊡	-0.9807(857)	-0.0071(24)	-0.0938(216)	0.1123(267)
		☒☒☒⊡⊡	-0.9968(3674)	-0.0106(82)	-0.0332(174)	0.103(250)
	36	☒☒⊡⊡⊡	-0.9991(3158)	-0.0064(26)	-0.0115(147)	0.0438(161)
		☒⊡☒⊡⊡	-0.9291(4453)	-0.0057(57)	-0.035(157)	0.0632(216)
		⊡☒☒⊡⊡	-1.1472(1013)	-0.0089(20)	-0.0153(22)	0.0606(37)
		☒☒☒⊡⊡	-0.9147(1853)	-0.0055(26)	-0.0357(66)	0.0634(200)
	42	☒☒⊡⊡⊡	-1.4568(553)	-0.0091(5)	-0.0387(33)	0.0788(6)
		☒⊡☒⊡⊡	-1.225(395)	-0.0111(5)	-0.0126(41)	0.0335(22)
		⊡☒☒⊡⊡	-1.4899(52)	-0.018(1)	-0.0477(11)	0.0575(6)
		☒☒☒⊡⊡	-1.1572(1973)	-0.0105(40)	-0.0439(110)	0.0544(306)
8	32	☒☒⊡⊡⊡⊡	-0.2458(31)	-0.0123(1)	-0.0772(48)	0.2356(76)
		☒⊡☒⊡⊡⊡	-0.2019(62)	-0.009(35)	-0.1211(724)	0.184(1920)
		⊡☒☒⊡⊡⊡	-0.187(62)	-0.0053(4)	-0.1601(27)	0.1836(78)
		☒☒☒⊡⊡⊡	-0.1917(410)	-0.0109(13)	-0.0498(326)	0.1529(894)
	40	☒☒⊡⊡⊡⊡	-0.3571(20)	-0.0138(2)	-0.146(45)	0.1565(65)
		☒⊡☒⊡⊡⊡	-0.2559(45)	-0.0141(6)	-0.0197(6)	0.081(21)
		⊡☒☒⊡⊡⊡	-0.4602(540)	-0.029(34)	-0.0071(79)	0.1664(278)
		☒☒☒⊡⊡⊡	-0.2677(54)	-0.0128(9)	-0.1015(91)	0.1259(343)
	48	☒☒⊡⊡⊡⊡	-0.3368(675)	-0.0144(44)	-0.0412(45)	0.0741(139)
		☒⊡☒⊡⊡⊡	-0.2052(1645)	-0.0109(117)	-0.0002(150)	0.0542(930)
		⊡☒☒⊡⊡⊡	-0.3454(435)	-0.0239(25)	0.051(84)	0.0761(74)
		☒☒☒⊡⊡⊡	-0.2439(396)	-0.01(34)	-0.1081(142)	0.1004(1034)
10	40	☒⊡☒⊡⊡	-0.0394(33)	-0.0041(2)	-0.0064(90)	0.0525(155)
		☒⊡⊡⊡☒	-0.0198(14)	-0.0028(3)	-0.016(53)	0.0453(91)
		⊡⊡☒⊡☒	-0.0094(50)	-0.0003(10)	-0.0498(92)	0.1062(293)
		☒⊡☒⊡☒	-0.0161(10)	-0.0016(2)	-0.0513(31)	0.1291(208)
	50	☒☒⊡⊡⊡	-0.069(154)	-0.0048(7)	-0.0402(286)	0.0768(500)
		☒⊡☒⊡⊡	-0.0485(41)	-0.0048(4)	0.001(25)	0.0405(82)
		⊡☒☒⊡⊡	-0.0253(70)	-0.0014(10)	-0.062(55)	0.0827(148)
		☒☒☒⊡⊡	-0.024(13)	-0.0013(2)	-0.0593(30)	0.0778(208)
	60	☒☒⊡⊡⊡	-0.0724(42)	-0.0055(3)	-0.001(13)	0.0391(40)
		☒⊡☒⊡⊡	-0.0547(160)	-0.0051(16)	-0.0119(61)	0.0502(316)
		⊡☒☒⊡⊡	-0.0838(352)	-0.0099(45)	-0.0331(86)	0.084(491)
		☒☒☒⊡⊡	-0.0204(23)	-0.0007(3)	-0.0668(32)	0.0814(379)
12	60	☒☒⊡	-0.0389(145)	-0.0032(10)	-0.0301(237)	0.0905(531)
		☒⊡☒	-0.0163(80)	-0.0023(11)	-0.0056(58)	0.0583(399)
		⊡☒☒	-0.0127(277)	-0.0016(43)	-0.0345(432)	0.1286(2113)
		☒☒☒	-0.0116(222)	-0.0014(27)	-0.0337(615)	0.1458(3163)

Table A.4: Results for the fit parameters referring to Table 5.2 for $\mathcal{L}_{short}$. The parameters have the absolute error attached to them, the relative error in percent can be found in Table A.5. The boxes refer to the different κ values for every N_τ, cf. Table A.9. ☒ means, that this κ is part of the fit, ⊡ means, that this κ is not part of the fit. All results were obtained with the method "Newton".

N_τ	N_s	κ	a_2^β	a_2^κ	a_3^κ	a_4^0
6	30	⊠⊠⊡⊡⊡	3.85%	4.59%	36.03%	14.43%
		⊠⊡⊠⊡⊡	14.59%	23.34%	38.46%	3.37%
		⊡⊠⊠⊡⊡	8.73%	33.31%	22.98%	23.82%
		⊠⊠⊠⊡⊡	36.85%	77.12%	52.43%	24.3%
	36	⊠⊠⊡⊡⊡	31.61%	41.04%	127.86%	36.65%
		⊠⊡⊠⊡⊡	47.93%	99.26%	44.76%	34.15%
		⊡⊠⊠⊡⊡	8.83%	22.44%	14.24%	6.14%
		⊠⊠⊠⊡⊡	20.26%	47.5%	18.49%	31.54%
	42	⊠⊠⊡⊡⊡	3.79%	5.61%	8.42%	0.79%
		⊠⊡⊠⊡⊡	3.23%	4.11%	32.58%	6.5%
		⊡⊠⊠⊡⊡	0.35%	0.67%	2.25%	1.12%
		⊠⊠⊠⊡⊡	17.05%	38.02%	24.99%	56.33%
8	32	⊠⊠⊡⊡⊡⊡	1.27%	0.55%	6.22%	3.23%
		⊠⊡⊠⊡⊡⊡	3.08%	38.7%	59.83%	104.35%
		⊡⊠⊠⊡⊡⊡	3.32%	7.91%	1.71%	4.24%
		⊠⊠⊠⊡⊡⊡	21.4%	11.55%	65.54%	58.44%
	40	⊠⊠⊡⊡⊡⊡	0.55%	1.75%	3.06%	4.14%
		⊠⊡⊠⊡⊡⊡	1.76%	3.98%	3.21%	2.62%
		⊡⊠⊠⊡⊡⊡	11.73%	11.63%	111.87%	16.72%
		⊠⊠⊠⊡⊡⊡	2.03%	7.34%	9.%	27.22%
	48	⊠⊠⊡⊡⊡⊡	20.04%	30.35%	10.88%	18.73%
		⊠⊡⊠⊡⊡⊡	80.17%	107.04%	6074.57%	171.68%
		⊡⊠⊠⊡⊡⊡	12.59%	10.3%	16.38%	9.69%
		⊠⊠⊠⊡⊡⊡	16.24%	34.25%	13.18%	102.98%
10	40	⊠⊡⊠⊡⊡	-8.28%	5.55%	141.46%	29.59%
		⊠⊡⊡⊡⊠	7.3%	11.0%	33.04%	20.08%
		⊡⊡⊠⊡⊠	53.13%	392.97%	18.41%	27.53%
		⊠⊡⊠⊡⊠	6.47%	9.38%	6.05%	16.1%
	50	⊠⊠⊡⊡⊡	22.27%	15.56%	71.22%	65.16%
		⊠⊡⊠⊡⊡	8.54%	9.09%	244.18%	20.35%
		⊡⊠⊠⊡⊡	27.46%	72.83%	8.95%	17.9%
		⊠⊠⊠⊡⊡	5.37%	16.36%	5.%	26.77%
	60	⊠⊠⊡⊡⊡	5.79%	6.1%	123.77%	10.2%
		⊠⊡⊠⊡⊡	29.33%	30.47%	51.12%	62.97%
		⊡⊠⊠⊡⊡	42.04%	45.36%	26.11%	58.52%
		⊠⊠⊠⊡⊡	11.06%	43.95%	4.73%	46.52%
12	60	⊠⊠⊡	37.33%	33.21%	78.7%	58.7%
		⊠⊡⊠	48.88%	50.12%	104.87%	68.44%
		⊡⊠⊠	218.9%	272.34%	125.04%	164.32%
		⊠⊠⊠	191.72%	199.57%	182.33%	216.87%

Table A.5: Relative errors for the results for the fit parameters for $\mathcal{L}_{short}$ from table Table A.4 the error is written as $\frac{100\cdot\Delta a_x^y}{a_x^y}\%$. The boxes refer to the different κ values for every N_τ, cf. Table A.9. ⊠ means, that this κ is part of the fit, ⊡ means, that this κ is not part of the fit. All results were obtained with the method "Newton".

N_τ	N_s	κ	a_2^β	a_2^κ	a_3^β	a_3^κ	a_4^0	a_4^κ
6	30	☒☒⊡⊡⊡	-0.7939(17383)	-0.0087(187)	0.0595(313188)	-0.0397(6551)	0.1022(5474)	-0.2628(253685)
		☒⊡☒⊡⊡	-1.0034(4865)	-0.0093(80)	-0.1281(79182)	-0.0372(2772)	0.0875(614)	-0.1022(41714)
		⊡☒☒⊡⊡	-1.0164(5986)	-0.0077(155)	-1.7853(56409)	-0.1071(4265)	0.1086(569)	-0.1721(33088)
		☒☒☒⊡⊡	-0.9169(10407)	-0.0101(186)	-0.3068(67651)	-0.0483(2827)	0.101(651)	-0.218(18496)
	36	☒☒⊡⊡⊡	-0.9345(153)	-0.0055(1)	-2.2662(4174)	-0.0245(48)	0.0638(1)	-0.6497(186)
		☒⊡☒⊡⊡	-0.9306(198)	-0.0054(3)	2.7166(5281)	0.0138(72)	0.0725(23)	-0.4147(559)
		⊡☒☒⊡⊡	-1.151(4016)	-0.0086(77)	-3.6235(61112)	-0.0875(1021)	0.0747(574)	0.2302(6646)
		☒☒☒⊡⊡	-0.938(3216)	-0.0084(54)	-0.6493(119796)	0.0064(937)	0.0865(1514)	-0.0131(6113)
	42	☒☒⊡⊡⊡	-0.8386(3414)	-0.0089(14)	-9.2083(98175)	0.022(595)	0.0737(351)	-0.7491(6177)
		☒⊡☒⊡⊡	-1.2758(360)	-0.0108(6)	5.4713(7725)	0.0501(191)	0.0401(49)	-0.4093(2226)
		⊡☒☒⊡⊡	-1.3901(823)	-0.0158(22)	-3.6026(42525)	-0.0943(762)	0.0797(321)	-0.1413(2207)
		☒☒☒⊡⊡	-1.0763(2109)	-0.0072(25)	2.1972(17443)	-0.0314(401)	0.0802(468)	-0.5318(1912)
8	32	☒☒⊡⊡⊡⊡	-0.156(2470)	-0.0104(55)	-0.229(91221)	-0.0111(14724)	0.1617(4084)	0.8548(235382)
		☒⊡☒⊡⊡⊡	-0.2543(2520)	-0.0139(84)	-0.4247(233233)	-0.0261(16335)	0.111(6187)	0.1386(76323)
		⊡☒☒⊡⊡⊡	-0.1266(1038)	-0.0021(42)	-1.3581(7953)	-0.2237(1011)	0.1929(1320)	-0.0713(12056)
		☒☒☒⊡⊡⊡	-0.1006(2847)	-0.0082(165)	-0.4335(79402)	-0.0015(10623)	0.1413(6043)	0.4116(131273)
	40	☒☒⊡⊡⊡⊡	-0.4197(395)	-0.0181(31)	3.4703(15529)	0.1729(1294)	0.1658(1292)	-3.5076(18378)
		☒⊡☒⊡⊡⊡	-0.2345(650)	-0.0113(58)	-0.1751(102371)	-0.0624(7010)	0.1255(4884)	-0.1329(26463)
		⊡☒☒⊡⊡⊡	-0.2622(2406)	-0.0108(194)	-0.6368(129549)	-0.1805(8192)	0.1754(6692)	0.3736(37614)
		☒☒☒⊡⊡⊡	-0.1881(2676)	-0.0092(196)	-0.8883(59950)	-0.0819(4859)	0.121(3733)	-1.2017(29576)
	48	☒☒⊡⊡⊡⊡	-0.259(3347)	-0.0103(289)	-1.8824(393083)	-0.096(14761)	0.0649(3939)	-0.406(80377)
		☒⊡☒⊡⊡⊡	-0.1979(3027)	-0.0122(136)	-0.4487(56958)	0.0128(4786)	0.0451(3440)	0.1103(33621)
		⊡☒☒⊡⊡⊡	-0.2911(37)	-0.0222(2)	-1.535(627)	0.0342(59)	0.0766(6)	-1.1181(316)
		☒☒☒⊡⊡⊡	-0.2353(3397)	-0.0115(249)	-0.1983(31082)	-0.0443(2833)	0.0834(3621)	-0.6263(30373)
10	40	☒⊡☒⊡⊡	-0.0552(123)	-0.0052(7)	0.4985(13342)	0.021(2454)	0.1358(1246)	-0.7186(26209)
		☒⊡⊡⊡☒	-0.0278(159)	-0.004(29)	0.5211(9585)	0.0802(2031)	0.0597(1531)	-0.3125(22046)
		⊡⊡☒⊡☒	-0.0004(122)	0.0014(73)	-0.3504(6862)	-0.1189(4877)	0.1468(7299)	0.1947(59100)
		☒⊡☒⊡☒	-0.0209(122)	-0.0027(21)	0.2122(4588)	0.0071(759)	0.1628(3796)	-0.6654(23727)
	50	☒☒⊡⊡⊡	-0.0429(450)	-0.0047(32)	-0.9712(31300)	0.0414(2406)	0.0524(429)	-2.7433(8957)
		☒⊡☒⊡⊡	-0.06(308)	-0.0059(33)	0.6892(14585)	0.071(1910)	0.0686(997)	-0.3715(14872)
		⊡☒☒⊡⊡	-0.0397(637)	-0.0041(107)	-0.299(56388)	-0.0566(8357)	0.0908(4287)	-0.3866(44061)
		☒☒☒⊡⊡	-0.0281(242)	-0.0023(25)	0.1372(11290)	0.0089(899)	0.0983(5332)	-1.3116(40599)
	60	☒☒⊡⊡⊡	-0.0665(66)	-0.0058(3)	-0.0747(12297)	0.0696(828)	0.0392(125)	-2.1836(3692)
		☒⊡☒⊡⊡	-0.0556(145)	-0.0048(15)	-0.1797(37363)	-0.0696(4379)	0.0316(802)	1.1107(16684)
		⊡☒☒⊡⊡	0.059(233)	0.0102(48)	-4.2216(30009)	-0.706(5792)	0.0981(420)	3.0759(37821)
		☒☒☒⊡⊡	-0.002(1083)	0.0015(32)	-1.1626(11713)	-0.2136(8022)	0.1254(11511)	0.0725(154550)
12	60	☒☒⊡	-0.0237(91)	-0.0019(5)	0.3955(8815)	0.0171(1480)	0.0207(280)	0.4584(24488)
		☒⊡☒	-0.0158(794)	-0.0022(119)	-0.04(44113)	-0.0132(7517)	0.0834(6186)	-0.2074(73333)
		⊡☒☒	0.0046(130)	0.0009(13)	-0.6565(19952)	-0.115(2585)	0.0947(4173)	-0.4473(39380)
		☒☒☒	-0.0068(217)	-0.0007(28)	-0.0723(11386)	-0.0337(1979)	0.0951(6250)	-0.1237(36723)

Table A.6: Results for the fit parameters referring to Table 5.2 for $\mathcal{L}_{long}$. The parameters have the absolute error attached to them, the relative error in percent can be found in Table A.7. The boxes refer to the different κ values for every N_τ, cf. Table A.9. ☒ means, that this κ is part of the fit, ⊡ means, that this κ is not part of the fit. All results were obtained with the method "Newton".

N_τ	N_s	κ	a_2^β	a_2^κ	a_3^β	a_3^κ	a_4^0	a_4^κ
6	30	☒☒⊡⊡⊡	218.96%	214.39%	52650.1%	1649.65%	535.52%	9652.83%
		☒⊡☒⊡⊡	48.49%	86.44%	6179.2%	745.06%	70.23%	4081.59%
		⊡☒☒⊡⊡	58.9%	200.78%	315.97%	398.07%	52.44%	1922.52%
		☒☒☒⊡⊡	113.5%	184.67%	2205.22%	585.25%	64.52%	848.42%
	36	☒☒⊡⊡⊡	1.64%	2.38%	18.42%	19.81%	0.1%	2.87%
		☒⊡☒⊡⊡	2.13%	5.29%	19.44%	52.16%	3.13%	13.47%
		⊡☒☒⊡⊡	34.89%	89.62%	168.66%	116.61%	76.83%	288.68%
		☒☒☒⊡⊡	34.28%	64.57%	1844.98%	1456.1%	175.04%	4680.45%
	42	☒☒⊡⊡⊡	40.71%	15.53%	106.62%	269.7%	47.54%	82.47%
		☒⊡☒⊡⊡	2.82%	5.52%	14.12%	38.16%	12.14%	54.39%
		⊡☒☒⊡⊡	5.92%	14.17%	118.04%	80.72%	40.26%	156.26%
		☒☒☒⊡⊡	19.6%	35.25%	79.39%	127.88%	58.43%	35.96%
8	32	☒☒⊡⊡⊡⊡	158.37%	53.22%	3983.96%	13209.3%	252.57%	2753.7%
		☒⊡☒⊡⊡⊡	99.11%	60.69%	5491.45%	6249.34%	557.23%	5508.68%
		⊡☒☒⊡⊡⊡	82.%	205.69%	58.56%	45.22%	68.43%	1690.85%
		☒☒☒⊡⊡⊡	283.08%	201.27%	1831.5%	-71938.2%	427.76%	3189.28%
	40	☒☒⊡⊡⊡⊡	9.41%	16.9%	44.75%	74.82%	77.91%	52.39%
		☒⊡☒⊡⊡⊡	27.7%	50.78%	5845.49%	1123.31%	389.05%	1991.88%
		⊡☒☒⊡⊡⊡	91.74%	179.79%	2034.53%	453.81%	381.58%	1006.7%
		☒☒☒⊡⊡⊡	142.26%	212.87%	674.87%	593.65%	308.49%	246.12%
	48	☒☒⊡⊡⊡⊡	129.22%	279.25%	2088.2%	1538.19%	607.24%	1979.65%
		☒⊡☒⊡⊡⊡	152.91%	111.91%	1269.5%	3736.16%	763.07%	3048.71%
		⊡☒☒⊡⊡⊡	1.26%	1.12%	4.08%	17.3%	0.78%	2.83%
		☒☒☒⊡⊡⊡	144.4%	216.44%	1567.23%	639.63%	434.24%	484.97%
10	40	☒⊡☒⊡⊡	22.26%	13.88%	267.67%	1170.7%	91.74%	364.73%
		☒⊡⊡⊡☒	57.17%	71.21%	183.93%	253.09%	256.56%	705.58%
		⊡⊡☒⊡☒	2966.5%	515.75%	195.82%	410.18%	497.12%	3034.95%
		☒⊡☒⊡☒	58.2%	80.86%	216.24%	1061.87%	233.17%	356.56%
	50	☒☒⊡⊡⊡	104.91%	67.74%	322.27%	580.68%	81.75%	32.65%
		☒⊡☒⊡⊡	51.28%	55.39%	211.62%	268.87%	145.44%	400.31%
		⊡☒☒⊡⊡	160.32%	261.56%	1886.%	1476.91%	472.06%	1139.59%
		☒☒☒⊡⊡	86.05%	112.28%	823.15%	1006.78%	542.49%	309.53%
	60	☒☒⊡⊡⊡	9.93%	4.48%	1646.11%	118.98%	31.97%	16.91%
		☒⊡☒⊡⊡	26.06%	31.98%	2079.66%	629.34%	254.14%	150.21%
		⊡☒☒⊡⊡	39.49%	46.79%	71.08%	82.04%	42.79%	122.96%
		☒☒☒⊡⊡	5430.29%	208.71%	100.75%	375.63%	917.56%	21325.7%
12	60	☒☒⊡	38.28%	27.73%	222.86%	867.52%	135.28%	534.23%
		☒⊡☒	503.87%	551.86%	11039.1%	5713.48%	742.12%	3535.49%
		⊡☒☒	283.66%	147.5%	303.92%	224.83%	440.49%	880.47%
		☒☒☒	319.32%	387.15%	1573.78%	586.95%	657.23%	2968.71%

Table A.7: Relative errors for the results for the fit parameters for $\mathcal{L}_{short}$ from table Table A.6 the error is written as $\frac{100\cdot\Delta a_x^y}{a_x^y}\%$. The boxes refer to the different κ values for every N_τ, cf. Table A.9. ☒ means, that this κ is part of the fit, ⊡ means, that this κ is not part of the fit. All results were obtained with the method "Newton".

N_τ	N_s	κ	$a_2^\beta, a_2^\kappa, a_3^\kappa, a_4^0, \kappa_{Z_2}$	$a_2^\beta, a_2^\kappa, a_3^\beta, a_3^\kappa, a_4^0, a_4^\kappa, \kappa_{Z_2}$
6	30	☒☒⊡⊡⊡	-0.89, -0.01, -0.01, 0.075, 0.087	-0.89, -0.01, -0.08, -0.01, 0.091, -0.09, 0.087
		☒⊡☒⊡⊡	-0.89, -0.0075, -0.04, 0.075, 0.087	-0.9, -0.0075, -0.1, -0.04, 0.075, -0.1, 0.087
		⊡☒☒⊡⊡	-0.93, -0.008, -0.09, 0.1, 0.087	-0.93, -0.008, -0.1, -0.09, 0.1, -0.09, 0.087
		☒☒☒⊡⊡	-0.89, -0.01, -0.01, 0.09, 0.087	-0.89, -0.01, -0.15, -0.01, 0.09, -0.09, 0.087
	36	☒☒⊡⊡⊡	-0.95, -0.008, -0.015, 0.045, 0.084	-0.93, -0.0075, -0.1, -0.04, 0.075, -0.101, 0.089
		☒⊡☒⊡⊡	-0.95, -0.007, -0.04, 0.075, 0.085	-0.9, -0.0075, -0.1, -0.04, 0.075, -0.1, 0.087
		⊡☒☒⊡⊡	-0.9, -0.0075, -0.04, 0.075, 0.087	-0.94, -0.0075, -0.1, -0.0401, 0.075, -0.15, 0.089
		☒☒☒⊡⊡	-0.92, -0.0075, -0.04, 0.075, 0.084	-0.93, -0.008, -0.1, -0.01, 0.09, -0.09, 0.086
	42	☒☒⊡⊡⊡	-0.5, -0.009, -0.01, 0.09, 0.088	-0.9, -0.008, -0.1, -0.01, 0.06, -0.09, 0.089
		☒⊡☒⊡⊡	-0.6, -0.01, 0.05, 0.09, 0.089	-0.9, -0.008, -0.1, -0.012, 0.06, -0.4, 0.089
		⊡☒☒⊡⊡	-0.61, -0.015, -0.04, 0.04, 0.089	-1.05, -0.008, -0.1, -0.09, 0.1, -0.09, 0.089
		☒☒☒⊡⊡	-0.95, -0.008, -0.015, 0.055, 0.086	-0.95, -0.008, -0.1, -0.01, 0.09, -0.09, 0.089
8	32	☒☒⊡⊡⊡⊡	-0.05, -0.001, -0.048, 0.1, 0.113	-0.08, -0.001, -0.1, -0.047, 0.1, -0.1, 0.114
		☒⊡☒⊡⊡⊡	-0.0501, -0.0015, -0.01, 0.1, 0.115	-0.11, -0.0014, -0.15, -0.05, 0.1, 0.1, 0.114
		⊡☒☒⊡⊡⊡	-0.055, -0.001, -0.047, 0.1, 0.116	-0.1, -0.0015, -0.15, -0.15, 0.1, -0.1, 0.114
		☒☒☒⊡⊡⊡	-0.05, -0.01, -0.04, 0.2, 0.114	-0.0501, -0.0013, -0.15, -0.045, 0.1, 0.21, 0.113
	40	☒☒⊡⊡⊡⊡	-0.045, -0.0015, -0.048, 0.1, 0.116	-0.1, -0.0015, -0.15, -0.075, 0.1, -0.1, 0.112
		☒⊡☒⊡⊡⊡	-0.05, -0.0015, -0.048, 0.1, 0.116	-0.1, -0.0015, -0.151, -0.0501, 0.1, -0.101, 0.113
		⊡☒☒⊡⊡⊡	-0.05, -0.0015, -0.048, 0.1, 0.115	-0.11, -0.0015, -0.15, -0.15, 0.1, -0.1, 0.114
		☒☒☒⊡⊡⊡	-0.045, -0.0015, -0.048, 0.1, 0.114	-0.11, -0.00145, -0.14, -0.15, 0.1, -0.1, 0.114
	48	☒☒⊡⊡⊡⊡	-0.05, -0.0015, -0.01, 0.1, 0.115	-0.066, -0.0015, -0.1, -0.056, 0.099, -0.1, 0.113
		☒⊡☒⊡⊡⊡	-0.05, -0.0015, -0.01, 0.11, 0.114	-0.053, -0.0015, -0.15, -0.0055, 0.1, 0.1, 0.114
		⊡☒☒⊡⊡⊡	-0.05, -0.0015, -0.01, 0.11, 0.114	-0.047, -0.0015, -0.15, -0.055, 0.1, 0.1, 0.115
		☒☒☒⊡⊡⊡	-0.0501, -0.01, -0.04, 0.2, 0.114	-0.0505, -0.0015, -0.15, -0.045, 0.1, -0.11, 0.114
10	40	☒⊡☒⊡⊡	-0.03, -0.001, -0.01, 0.12, 0.124	-0.029, -0.004, -0.1, -0.08, 0.12, 0.11, 0.124
		☒⊡⊡⊡☒	-0.01, -0.001, -0.01, 0.1, 0.124	-0.015, -0.0015, -0.1, -0.01, 0.08, -0.15, 0.124
		⊡⊡☒⊡☒	-0.01, -0.001, -0.01, 0.101, 0.124	-0.009, -0.001, -0.1, -0.041, 0.15, -0.3, 0.124
		☒⊡☒⊡☒	-0.019, -0.001, -0.041, 0.2, 0.124	-0.02, -0.001, 0.15, -0.01, 0.2, -0.1, 0.125
	50	☒☒⊡⊡⊡	-0.023, -0.003, -0.05, 0.08, 0.124	-0.02, -0.001, -0.07, -0.05, 0.1, -0.1, 0.124
		☒⊡☒⊡⊡	-0.031, -0.002, -0.045, 0.09, 0.124	-0.022, -0.001, -0.25, -0.01, 0.12, 0.12, 0.124
		⊡☒☒⊡⊡	-0.024, -0.001, -0.05, 0.09, 0.124	-0.02, -0.002, -0.5, -0.01, 0.12, -0.12, 0.124
		☒☒☒⊡⊡	-0.024, -0.001, -0.05, 0.09, 0.124	-0.02, -0.001, -0.07, -0.05, 0.1, -0.14, 0.124
	60	☒☒⊡⊡⊡	-0.03, -0.001, -0.01, 0.12, 0.124	-0.045, -0.004, -0.095, -0.02, 0.09, -0.12, 0.124
		☒⊡☒⊡⊡	-0.021, -0.003, -0.01, 0.12, 0.124	-0.045, -0.004, -0.05, -0.02, 0.08, -0.11, 0.124
		⊡☒☒⊡⊡	-0.02, -0.001, -0.05, 0.12, 0.125	-0.02, -0.001, -0.06, -0.05, 0.1, -0.1, 0.125
		☒☒☒⊡⊡	-0.02, -0.001, -0.06, 0.12, 0.124	-0.021, -0.0011, -0.1, -0.08, 0.12, 0.12, 0.124
12	60	☒☒⊡	-0.025, -0.001, -0.01, 0.2, 0.125	-0.02, -0.001, -0.05, -0.01, 0.1, -0.1, 0.125
		☒⊡☒	-0.01, -0.001, -0.01, 0.1, 0.125	-0.01, -0.001, -0.05, -0.01, 0.1, -0.1, 0.125
		⊡☒☒	-0.011, -0.0015, -0.025, 0.15, 0.125	-0.01, -0.0015, -0.05, -0.025, 0.15, -0.06, 0.125
		☒☒☒	-0.011, -0.0015, -0.03, 0.15, 0.125	-0.011, -0.0011, -0.01, -0.015, 0.1, -0.002 , 0.125

Table A.8: Initial values for the fit parameters referring to Table 5.2. The boxes refer to the different κ values for every N_τ, cf. table Table A.9. ☒ means, that this κ is part of the fit, ⊡ means, that this κ is not part of the fit. All results were obtained with the method "Newton".

N_τ	κ	Cut-Off from below | Cut-Off from above			
		Aspect ratio 4	Aspect ratio 5	Aspect ratio 6	Aspect ratio 7
6	0.0750	–	0 | 0	0 | 0	0 | 0
	0.0850	–	0 | 0	0 | 0	0 | 0
	0.0900	–	20 | 30	30 | 20	20 | 35
	0.1000	–	–	–	–
	0.1100	–	–	–	–
8	0.1100	10 | 20	0 | 15	10 | 10	–
	0.1150	0 | 30	5 | 40	0 | 5	–
	0.1200	0 | 0	0 | 0	0 | 0	–
	0.1250	–	–	–	–
	0.1300	–	–	–	–
	0.1350	–	–	–	–
10	0.1200	0 | 40	10 | 30	5 | 30	–
	0.1250	–	40 | 20	0 | 0	–
	0.1300	0 | 0	0 | 20	0 | 0	–
	0.1350	–	–	–	–
	0.1400	0 | 0	–	–	–
12	0.1250	–	5 | 30	–	–
	0.1300	–	30 | 0	–	–
	0.1350	–	10 | 10	–	–

Table A.9: Chosen cut-off values for every κ. The cut-offs from below come from the left, the cut-offs from above from the right side of the data. This process is necessary to restrict the dataset to the linear zone around the phase transition.

Bibliography

[1] G. Hanson, G. S. Abrams, A. M. Boyarski, M. Breidenbach, F. Bulos, W. Chinowsky, G. J. Feldman, C. E. Friedberg, D. Fryberger, G. Goldhaber, D. L. Hartill, B. Jean-Marie, J. A. Kadyk, R. R. Larsen, A. M. Litke, D. Lüke, B. A. Lulu, V. Lüth, H. L. Lynch, C. C. Morehouse, J. M. Paterson, M. L. Perl, F. M. Pierre, T. P. Pun, P. A. Rapidis, B. Richter, B. Sadoulet, R. F. Schwitters, W. Tanenbaum, G. H. Trilling, F. Vannucci, J. S. Whitaker, F. C. Winkelmann, and J. E. Wiss. Evidence for jet structure in hadron production by e^+e^- annihilation. *Phys. Rev. Lett.*, 35:1609–1612, Dec 1975. URL: https://link.aps.org/doi/10.1103/PhysRevLett.35.1609, doi:10.1103/PhysRevLett.35.1609.

[2] R. F. Schwitters, A. M. Boyarski, M. Breidenbach, F. Bulos, G. J. Feldman, G. Hanson, D. L. Hartill, B. Jean-Marie, R. R. Larsen, D. Lüke, V. Lüth, H. L. Lynch, C. C. Morehouse, J. M. Paterson, M. L. Perl, T. P. Pun, P. Rapidis, B. Richter, W. Tanenbaum, F. Vannucci, F. M. Pierre, G. S. Abrams, W. Chinowsky, C. E. Friedberg, G. Goldhaber, J. A. Kadyk, A. M. Litke, B. A. Lulu, B. Sadoulet, G. H. Trilling, J. S. Whitaker, F. C. Winkelmann, and J. E. Wiss. Azimuthal asymmetry in inclusive hadron production by e^+e^- annihilation. *Phys. Rev. Lett.*, 35:1320–1322, Nov 1975. URL: https://link.aps.org/doi/10.1103/PhysRevLett.35.1320, doi:10.1103/PhysRevLett.35.1320.

[3] M. Gell-Mann. A schematic model of baryons and mesons. *Physics Letters*, 8(3):214 – 215, 1964. URL: http://www.sciencedirect.com/science/article/pii/S0031916364920013, doi:https://doi.org/10.1016/S0031-9163(64)92001-3.

[4] R. P. Feynman, M. Gell-Mann, and G. Zweig. Group u(6)$\bigotimes$u(6) generated by current components. *Phys. Rev. Lett.*, 13:678–680, Nov 1964. URL: https://link.aps.org/doi/10.1103/PhysRevLett.13.678, doi:10.1103/PhysRevLett.13.678.

[5] K.A. Olive. Review of particle physics. *Chinese Physics C*, 38(9):090001, aug 2014. doi:10.1088/1674-1137/38/9/090001.

[6] F. Englert and R. Brout. Broken symmetry and the mass of gauge vector mesons. *Phys. Rev. Lett.*, 13:321–323, Aug 1964. URL: https://link.aps.org/doi/10.1103/PhysRevLett.13.321, doi:10.1103/PhysRevLett.13.321.

[7] Peter W. Higgs. Broken symmetries and the masses of gauge bosons. *Phys. Rev. Lett.*, 13:508–509, Oct 1964. URL: https://link.aps.org/doi/10.1103/PhysRevLett.13.508, doi:10.1103/PhysRevLett.13.508.

[8] G. Aad, T. Abajyan, B. Abbott, J. Abdallah, S. Abdel Khalek, A.A. Abdelalim, O. Abdinov, R. Aben, B. Abi, M. Abolins, and et al. Observation of a new particle in the search for the standard model higgs boson with the atlas detector at the lhc. *Physics Letters B*, 716(1):1–29, Sep 2012. URL: http://dx.doi.org/10.1016/j.physletb.2012.08.020, doi:10.1016/j.physletb.2012.08.020.

[9] S. Chatrchyan, V. Khachatryan, A.M. Sirunyan, A. Tumasyan, W. Adam, E. Aguilo, T. Bergauer, M. Dragicevic, J. Erö, C. Fabjan, and et al. Observation of a new boson at a mass of 125 gev with the cms experiment at the lhc. *Physics Letters B*, 716(1):30–61, Sep 2012. URL: http://dx.doi.org/10.1016/j.physletb.2012.08.021, doi:10.1016/j.physletb.2012.08.021.

[10] Yi-Bo Yang, Jian Liang, Yu-Jiang Bi, Ying Chen, Terrence Draper, Keh-Fei Liu, and Zhaofeng Liu. Proton mass decomposition from the qcd energy momentum tensor. *Phys. Rev. Lett.*, 121:212001, Nov 2018. URL: https://link.aps.org/doi/10.1103/PhysRevLett.121.212001, doi:10.1103/PhysRevLett.121.212001.

[11] Harald Fritzsch and Murray Gell-Mann. Current algebra: Quarks and what else? *eConf*, C720906V2:135–165, 1972. arXiv:hep-ph/0208010.

[12] H. Fritzsch, M. Gell-Mann, and H. Leutwyler. Advantages of the color octet gluon picture. *Physics Letters B*, 47(4):365 – 368, 1973. URL: http://www.sciencedirect.com/science/article/pii/0370269373906254, doi:https://doi.org/10.1016/0370-2693(73)90625-4.

[13] H. David Politzer. Reliable perturbative results for strong interactions? *Phys. Rev. Lett.*, 30:1346–1349, Jun 1973. URL: https://link.aps.org/doi/10.1103/PhysRevLett.30.1346, doi:10.1103/PhysRevLett.30.1346.

[14] David J. Gross and Frank Wilczek. Ultraviolet behavior of non-abelian gauge theories. *Phys. Rev. Lett.*, 30:1343–1346, Jun 1973. URL: https://link.aps.org/doi/10.1103/PhysRevLett.30.1343, doi:10.1103/PhysRevLett.30.1343.

[15] O. W. Greenberg. Spin and Unitary Spin Independence in a Paraquark Model of Baryons and Mesons. *Phys. Rev. Lett.*, 13:598–602, 1964. doi:10.1103/PhysRevLett.13.598.

[16] M. Y. Han and Y. Nambu. Three-triplet model with double SU(3) symmetry. *Phys. Rev.*, 139:B1006–B1010, Aug 1965. URL: https://link.aps.org/doi/10.1103/PhysRev.139.B1006, doi:10.1103/PhysRev.139.B1006.

[17] G. 't Hooft and M. Veltman. Regularization and renormalization of gauge fields. *Nuclear Physics B*, 44(1):189 – 213, 1972. URL: http://www.sciencedirect.com/science/article/pii/0550321372902799, doi:https://doi.org/10.1016/0550-3213(72)90279-9.

[18] Christopher Czaban and Owe Philipsen. The QCD deconfinement critical point for $N_\tau = 8$ with $N_f = 2$ flavours of unimproved Wilson fermions. *PoS*, LATTICE2016:056, 2017. doi:10.22323/1.256.0056.

[19] David J. Gross and Frank Wilczek. Asymptotically free gauge theories. i. *Phys. Rev. D*, 8:3633–3652, Nov 1973. URL: https://link.aps.org/doi/10.1103/PhysRevD.8.3633, doi:10.1103/PhysRevD.8.3633.

[20] David J. Gross and Frank Wilczek. Asymptotically free gauge theories. ii. *Phys. Rev. D*, 9:980–993, Feb 1974. URL: https://link.aps.org/doi/10.1103/PhysRevD.9.980, doi:10.1103/PhysRevD.9.980.

[21] H David Politzer. Asymptotic freedom: An approach to strong interactions. *Physics Reports*, 14(4):129 – 180, 1974. URL: http://www.sciencedirect.com/science/article/pii/0370157374900143, doi:https://doi.org/10.1016/0370-1573(74)90014-3.

[22] C. Gattringer and C. Lang. *Quantum Chromodynamics on the Lattice: An Introductory Presentation*. Lecture Notes in Physics.

[23] I. Montvay and G. Münster. *Quantum Fields on a Lattice*. Cambridge Monographs on Mathematical Physics. Cambridge University Press, 1997.

[24] Franz J. Wegner. Duality in generalized ising models and phase transitions without local order parameters. *Journal of Mathematical Physics*, 12(10):2259–2272, 1971. arXiv:https://doi.org/10.1063/1.1665530, doi:10.1063/1.1665530.

[25] Kenneth G. Wilson. Confinement of quarks. *Phys. Rev. D*, 10:2445–2459, Oct 1974. URL: https://link.aps.org/doi/10.1103/PhysRevD.10.2445, doi:10.1103/PhysRevD.10.2445.

[26] Matthias Troyer and Uwe-Jens Wiese. Computational complexity and fundamental limitations to fermionic quantum monte carlo simulations. *Physical Review Letters*, 94(17), May 2005. URL: http://dx.doi.org/10.1103/PhysRevLett.94.170201, doi:10.1103/physrevlett.94.170201.

[27] Owe Philipsen. The QCD phase diagram at zero and small baryon density. *PoS*, LAT2005:016, 2006. arXiv:hep-lat/0510077, doi:10.22323/1.020.0016.

[28] Szabolcs Borsányi, Zoltán Fodor, Christian Hoelbling, Sándor D. Katz, Stefan Krieg, Claudia Ratti, and Kálmán K. Szabó. Is there still any t c mystery in lattice qcd? results with physical masses in the continuum limit iii. *Journal of High Energy Physics*, 2010(9), Sep 2010. URL: http://dx.doi.org/10.1007/JHEP09(2010)073, doi:10.1007/jhep09(2010)073.

[29] H. J. Rothe. *Lattice gauge theories: An Introduction*, volume 43. 1992.

[30] Michael E. Peskin and Daniel V. Schroeder. *An Introduction to quantum field theory*. Addison-Wesley, Reading, USA, 1995.

[31] Thomas DeGrand and Carleton E. Detar. *Lattice methods for quantum chromodynamics*. 2006.

[32] C. N. Yang and R. L. Mills. Conservation of isotopic spin and isotopic gauge invariance. *Phys. Rev.*, 96:191–195, Oct 1954. URL: https://link.aps.org/doi/10.1103/PhysRev.96.191, doi:10.1103/PhysRev.96.191.

[33] H.B. Nielsen and M. Ninomiya. A no-go theorem for regularizing chiral fermions. *Physics Letters B*, 105(2):219–223, 1981. URL: https://www.sciencedirect.com/science/article/pii/0370269381910261, doi:https://doi.org/10.1016/0370-2693(81)91026-1.

[34] H.B. Nielsen and M. Ninomiya. Absence of neutrinos on a lattice: (i). proof by homotopy theory. *Nuclear Physics B*, 185(1):20–40, 1981. URL: https://www.sciencedirect.com/science/article/pii/0550321381903618, doi:https://doi.org/10.1016/0550-3213(81)90361-8.

[35] H.B. Nielsen and M. Ninomiya. Absence of neutrinos on a lattice: (ii). intuitive topological proof. *Nuclear Physics B*, 193(1):173–194, 1981. URL: https://www.sciencedirect.com/science/article/pii/0550321381905241, doi:https://doi.org/10.1016/0550-3213(81)90524-1.

[36] Christian Borgs and Erhard Seiler. Lattice {Yang-Mills} Theory at Nonzero Temperature and the Confinement Problem. *Commun. Math. Phys.*, 91:329, 1983. doi:10.1007/BF01208780.

[37] G. 't Hooft. A property of electric and magnetic flux in non-abelian gauge theories. *Nuclear Physics B*, 153:141–160, 1979. URL: https://www.sciencedirect.com/science/article/pii/0550321379905959, doi:https://doi.org/10.1016/0550-3213(79)90595-9.

[38] Leonard Susskind. Lattice models of quark confinement at high temperature. *Phys. Rev. D*, 20:2610–2618, Nov 1979. URL: https://link.aps.org/doi/10.1103/PhysRevD.20.2610, doi:10.1103/PhysRevD.20.2610.

[39] A.M. Polyakov. Thermal properties of gauge fields and quark liberation. *Physics Letters B*, 72(4):477–480, 1978. URL: https://www.sciencedirect.com/science/article/pii/0370269378907372, doi:https://doi.org/10.1016/0370-2693(78)90737-2.

[40] S. Duane, A. D. Kennedy, B. J. Pendleton, and D. Roweth. Hybrid Monte Carlo. *Phys. Lett.*, B195:216–222, 1987. doi:10.1016/0370-2693(87)91197-X.

[41] Nicholas Metropolis, Arianna W. Rosenbluth, Marshall N. Rosenbluth, Augusta H. Teller, and Edward Teller. Equation of state calculations by fast computing machines. *The Journal of Chemical Physics*, 21(6):1087–1092, 1953. arXiv:https://doi.org/10.1063/1.1699114, doi:10.1063/1.1699114.

[42] Nicola Cabibbo and Enzo Marinari. A new method for updating su(n) matrices in computer simulations of gauge theories. *Physics Letters B*, 119(4):387–390, 1982. URL: https://www.sciencedirect.com/science/article/pii/0370269382906967, doi:https://doi.org/10.1016/0370-2693(82)90696-7.

[43] A.D. Kennedy and B.J. Pendleton. Improved heatbath method for monte carlo calculations in lattice gauge theories. *Physics Letters B*, 156(5):393–399, 1985. URL: https://www.sciencedirect.com/science/article/pii/0370269385916326, doi:https://doi.org/10.1016/0370-2693(85)91632-6.

[44] Ulli Wolff. Monte Carlo errors with less errors. *Comput. Phys. Commun.*, 156:143–153, 2004. [Erratum: Comput. Phys. Commun.176,383(2007)]. arXiv:hep-lat/0306017, doi:10.1016/S0010-4655(03)00467-3,10.1016/j.cpc.2006.12.001.

[45] M.E.J. Newman and G.T. Barkema. *Monte Carlo Methods in Statistical Physics*. Clarendon Press, 1999. URL: https://books.google.de/books?id=kQN6DwAAQBAJ.

[46] Alan M. Ferrenberg and Robert H. Swendsen. New monte carlo technique for studying phase transitions. *Phys. Rev. Lett.*, 61:2635–2638, Dec 1988. URL: http://link.aps.org/doi/10.1103/PhysRevLett.61.2635, doi:10.1103/PhysRevLett.61.2635.

[47] Alan M. Ferrenberg and Robert H. Swendsen. Optimized monte carlo data analysis. *Phys. Rev. Lett.*, 63:1195–1198, Sep 1989. URL: http://link.aps.org/doi/10.1103/PhysRevLett.63.1195, doi:10.1103/PhysRevLett.63.1195.

[48] Frederik Depta. Pion and quark masses along the chiral critical line in the $n_f = 2$ qcd phase diagram.

[49] Martin Lüscher. Properties and uses of the wilson flow in lattice QCD. *Journal of High Energy Physics*, 2010(8), aug 2010. URL: https://doi.org/10.1007%2Fjhep08%282010%29071, doi:10.1007/jhep08(2010)071.

[50] and Szabolcs Borsányi, Stephan Dürr, Zoltán Fodor, Christian Hoelbling, Sándor D. Katz, Stefan Krieg, Thorsten Kurth, Laurent Lellouch, Thomas Lippert, Craig McNeile, and Kálmán K. Szabó. High-precision scale setting in lattice QCD. *Journal of High Energy Physics*, 2012(9), sep 2012. URL: https://doi.org/10.1007%2Fjhep09%282012%29010, doi:10.1007/jhep09(2012)010.

[51] Alessandro* Sciarra, Christopher Pinke, Matthias Bach, Francesca Cuteri, Lars Zeidlewicz, Christian Schäfer, Tim Breitenfelder, Christopher Czaban, Stefano Lottini, and Paul Frederik Depta. Cl2qcd, February 2021. doi:10.5281/zenodo.5121894.

[52] Owe Philipsen, Christopher Pinke, Alessandro Sciarra, and Matthias Bach. Cl2qcd - lattice qcd based on opencl, 2014. arXiv:1411.5219.

[53] Matthias Bach, Volker Lindenstruth, Owe Philipsen, and Christopher Pinke. Lattice QCD based on OpenCL. *Comput. Phys. Commun.*, 184:2042–2052, 2013. arXiv:1209.5942, doi:10.1016/j.cpc.2013.03.020.

[54] Matthias Bach. *Energy- and cost-efficient Lattice-QCD computations using graphics processing units*. doctoralthesis, Universitätsbibliothek Johann Christian Senckenberg, 2015.

[55] Alessandro Sciarra. *The QCD phase diagram at purely imaginary chemical potential from the lattice*. doctoralthesis, Universitätsbibliothek Johann Christian Senckenberg, 2017.

[56] David Rohr, Matthias Bach, Gvozden Nešković, Volker Lindenstruth, Christopher Pinke, and Owe Philipsen. *Lattice-CSC: Optimizing and Building an Efficient Supercomputer for Lattice-QCD and to Achieve First Place in Green500*, pages 179–196. Springer International Publishing, Cham, 2015. doi:10.1007/978-3-319-20119-1_14.

[57] Matthias Bach, Matthias Kretz, Volker Lindenstruth, and David Rohr. Optimized hpl for amd gpu and multi-core cpu usage. *Computer Science - Research and Development*, 26(3):153, Apr 2011. doi:10.1007/s00450-011-0161-5.

[58] openqcd. https://luscher.web.cern.ch/luscher/openQCD/.

[59] Jonas Rylund Glesaaen and Benjamin Jäger. openqcd-fastsum, April 2018. Development supported by STFC grants ST/L000369/1 and ST/P00055X/1. doi:10.5281/zenodo.2216355.

[60] Jonas Rylund Glesaaen and Benjamin Jäger. openQCD-FASTSUM. http://fastsum.gitlab.io/, 4 2018.

[61] Readme of openqcd-fastsum. http://fastsum.gitlab.io/documentation/project-readme/.

[62] Programs of openqcd-fastsum. https://gitlab.com/fastsum/openqcd-fastsum/-/blob/master/main/INDEX.

[63] Alessandro Sciarra. Bahamas, February 2021. doi:10.5281/zenodo.4572833.

[64] Alessandro Sciarra. BaHaMAS: A Bash Handler to Monitor and Administrate Simulations. *EPJ Web Conf.*, 175:09003, 2018. arXiv:1710.08831, doi:10.1051/epjconf/201817509003.

[65] Plasma. https://gitlab.itp.uni-frankfurt.de/lattice-qcd/plasma.

[66] Python fitting gui. https://gitlab.itp.uni-frankfurt.de/lattice-qcd/ag-philipsen/python-fitting-gui.

[67] Nigel D Goldenfeld. *Lectures On Phase Transitions And The Renormalization Group*. Frontiers in physics. Westview Press, 1992. doi:10.1201/9780429493492.

[68] Owe Philipsen. Lattice QCD at non-zero temperature and baryon density. In *Les Houches Summer School: Session 93: Modern perspectives in lattice QCD: Quantum field theory and high performance computing*, pages 273–330, 9 2010. arXiv:1009.4089.

[69] Owe Philipsen. Lattice Constraints on the QCD Chiral Phase Transition at Finite Temperature and Baryon Density. *Symmetry*, 13(11):2079, 2021. arXiv:2111.03590, doi:10.3390/sym13112079.

[70] L. D. Landau. On the theory of phase transitions. *Zh. Eksp. Teor. Fiz.*, 7:19–32, 1937.

[71] Gregg Jaeger. The ehrenfest classification of phase transitions: Introduction and evolution. *Archive for History of Exact Sciences*, 53:51–81, 05 1998. doi:10.1007/s004070050021.

[72] C. N. Yang and T. D. Lee. Statistical theory of equations of state and phase transitions. i. theory of condensation. *Phys. Rev.*, 87:404–409, Aug 1952. URL: https://link.aps.org/doi/10.1103/PhysRev.87.404, doi:10.1103/PhysRev.87.404.

[73] T. D. Lee and C. N. Yang. Statistical theory of equations of state and phase transitions. ii. lattice gas and ising model. *Phys. Rev.*, 87:410–419, Aug 1952. URL: https://link.aps.org/doi/10.1103/PhysRev.87.410, doi:10.1103/PhysRev.87.410.

[74] Andrea Pelissetto and Ettore Vicari. Critical phenomena and renormalization group theory. *Phys. Rept.*, 368:549–727, 2002. arXiv:cond-mat/0012164, doi:10.1016/S0370-1573(02)00219-3.

[75] K. Wilson and John Kogut. The renormalization group and the epsilon expansion. 08 1974.

[76] B. Widom. Surface tension and molecular correlations near the critical point. *The Journal of Chemical Physics*, 43(11):3892–3897, 1965. doi:10.1063/1.1696617.

[77] Leo P. Kadanoff. Scaling laws for ising models near T_c. *Physics Physique Fizika*, 2:263–272, Jun 1966. URL: https://link.aps.org/doi/10.1103/PhysicsPhysiqueFizika.2.263, doi:10.1103/PhysicsPhysiqueFizika.2.263.

[78] F Karsch, E Laermann, and Ch Schmidt. The chiral critical point in 3-flavour QCD. *Physics Letters B*, 520(1-2):41–49, nov 2001. URL: https://doi.org/10.1016%2Fs0370-2693%2801%2901114-5, doi:10.1016/s0370-2693(01)01114-5.

[79] K. Binder. Finite size scaling analysis of Ising model block distribution functions. *Z. Phys. B*, 43:119–140, 1981. doi:10.1007/BF01293604.

[80] Xiao-Yong Jin, Yoshinobu Kuramashi, Yoshifumi Nakamura, Shinji Takeda, and Akira Ukawa. Critical point phase transition for finite temperature 3-flavor qcd with nonperturbatively O(a) improved wilson fermions at $N_{\mathrm{t}} = 10$. *Phys. Rev. D*, 96:034523, Aug 2017. URL: https://link.aps.org/doi/10.1103/PhysRevD.96.034523, doi:10.1103/PhysRevD.96.034523.

[81] Christopher Czaban. *Lattice discretization effects on the QCD phase structure at zero chemical potential and the Roberge-Weiss endpoint.* PhD thesis, 2018.

[82] Y. Aoki, G. Endrődi, Z. Fodor, S. D. Katz, and K. K. Szabó. The order of the quantum chromodynamics transition predicted by the standard model of particle physics. *Nature*, 443(7112):675–678, Oct 2006. URL: http://dx.doi.org/10.1038/nature05120, doi:10.1038/nature05120.

[83] Zoltan Fodor and Sandor D Katz. Lattice determination of the critical point of QCD at finite t and μ. *Journal of High Energy Physics*, 2002(03):014–014, mar 2002. URL: https://doi.org/10.1088%2F1126-6708%2F2002%2F03%2F014, doi:10.1088/1126-6708/2002/03/014.

[84] Z Fodor and S.D Katz. Critical point of QCD at finite t and , lattice results for physical quark masses. *Journal of High Energy Physics*, 2004(04):050–050, apr 2004. URL: https://doi.org/10.1088%2F1126-6708%2F2004%2F04%2F050, doi:10.1088/1126-6708/2004/04/050.

[85] Mark Alford. Color-superconducting quark matter. *Annual Review of Nuclear and Particle Science*, 51(1):131–160, 2001. arXiv:https://doi.org/10.1146/annurev.nucl.51.101701.132449, doi:10.1146/annurev.nucl.51.101701.132449.

[86] Mark G. Alford, Andreas Schmitt, Krishna Rajagopal, and Thomas Schäfer. Color superconductivity in dense quark matter. *Reviews of Modern Physics*, 80(4):1455–1515, nov 2008. URL: https://doi.org/10.1103%2Frevmodphys.80.1455, doi:10.1103/revmodphys.80.1455.

[87] KRISHNA RAJAGOPAL and FRANK WILCZEK. THE CONDENSED MATTER PHYSICS OF QCD. In *At The Frontier of Particle Physics*, pages 2061–2151. WORLD SCIENTIFIC, apr 2001. URL: https://doi.org/10.1142%2F9789812810458_0043, doi:10.1142/9789812810458_0043.

[88] Y. Iwasaki, K. Kanaya, S. Kaya, S. Sakai, and T. Yoshié. Finite temperature transitions in lattice qcd with wilson quarks: Chiral transitions and the influence of the strange quark. *Phys. Rev. D*, 54:7010–7031, Dec

1996. URL: https://link.aps.org/doi/10.1103/PhysRevD.54.7010, doi:10.1103/PhysRevD.54.7010.

[89] Frank R. Brown, Frank P. Butler, Hong Chen, Norman H. Christ, Zhihua Dong, Wendy Schaffer, Leo I. Unger, and Alessandro Vaccarino. On the existence of a phase transition for qcd with three light quarks. *Phys. Rev. Lett.*, 65:2491–2494, Nov 1990. URL: https://link.aps.org/doi/10.1103/PhysRevLett.65.2491, doi:10.1103/PhysRevLett.65.2491.

[90] Robert D. Pisarski and Frank Wilczek. Remarks on the chiral phase transition in chromodynamics. *Phys. Rev. D*, 29:338–341, Jan 1984. URL: https://link.aps.org/doi/10.1103/PhysRevD.29.338, doi:10.1103/PhysRevD.29.338.

[91] Francesca Cuteri, Owe Philipsen, and Alessandro Sciarra. The qcd chiral phase transition for different numbers of quark flavours, 2021. URL: https://arxiv.org/abs/2112.11107, doi:10.48550/ARXIV.2112.11107.

[92] Jana N. Guenther. Overview of the qcd phase diagram – recent progress from the lattice, 2021. arXiv:2010.15503.

[93] Philippe de Forcrand and Massimo D'Elia. Continuum limit and universality of the columbia plot, 2017. URL: https://arxiv.org/abs/1702.00330, doi:10.48550/ARXIV.1702.00330.

[94] Francesca Cuteri, Owe Philipsen, Alena Schön, and Alessandro Sciarra. Deconfinement critical point of lattice QCD with $n_f = 2$ wilson fermions. *Physical Review D*, 103(1), jan 2021. URL: https://doi.org/10.1103%2Fphysrevd.103.014513, doi:10.1103/physrevd.103.014513.

[95] Francesca Cuteri, Christopher Czaban, Owe Philipsen, and Alessandro Sciarra. Updates on the columbia plot and its extended/alternative versions. *EPJ Web of Conferences*, 175:07032, 2018. URL: https://doi.org/10.1051%2Fepjconf%2F201817507032, doi:10.1051/epjconf/201817507032.

[96] Philippe de Forcrand, Seyong Kim, and Owe Philipsen. A qcd chiral critical point at small chemical potential: is it there or not? 2007. URL: https://arxiv.org/abs/0711.0262, doi:10.48550/ARXIV.0711.0262.

[97] A. Bazavov, T. Bhattacharya, M. Cheng, C. DeTar, H.-T. Ding, Steven Gottlieb, R. Gupta, P. Hegde, U. M. Heller, F. Karsch, E. Laermann, L. Levkova, S. Mukherjee, P. Petreczky, C. Schmidt, R. A. Soltz, W. Soeldner, R. Sugar, D. Toussaint, W. Unger, and P. Vranas. Chiral and deconfinement aspects of the qcd transition. *Phys. Rev. D*, 85:054503, Mar 2012. URL: https://link.aps.org/doi/10.1103/PhysRevD.85.054503, doi:10.1103/PhysRevD.85.054503.

[98] J.S. Langer. Statistical theory of the decay of metastable states. *Annals Phys.*, 54:258–275, 1969. doi:10.1016/0003-4916(69)90153-5.

[99] Owe Philipsen and Christopher Pinke. Nature of the roberge-weiss transition in $N_f = 2$ qcd with wilson fermions. *Phys. Rev. D*, 89:094504, May 2014. URL: https://link.aps.org/doi/10.1103/PhysRevD.89.094504, doi:10.1103/PhysRevD.89.094504.

[100] Christopher Czaban, Francesca Cuteri, Owe Philipsen, Christopher Pinke, and Alessandro Sciarra. Roberge-weiss transition in $\mathrm{n_f} = 2$ qcd with wilson fermions and $\mathrm{n}_\tau = 6$. *Phys. Rev. D*, 93:054507, Mar 2016. URL: https://link.aps.org/doi/10.1103/PhysRevD.93.054507, doi:10.1103/PhysRevD.93.054507.

[101] Reinhold Kaiser and Owe Philipsen. Progress on the qcd deconfinement critical point for $n_\mathrm{f} = 2$ staggered fermions, 2023. arXiv:2212.14461.

[102] Rainer Sommer. Introduction to non-perturbative heavy quark effective theory, 2010. URL: https://arxiv.org/abs/1008.0710, doi:10.48550/ARXIV.1008.0710.

[103] Reinhold Kaiser, Owe Philipsen, and Alessandro Sciarra. The qcd deconfinement critical point for $n_\mathrm{f} = 2$ flavors of staggered fermions, 2021. URL: https://arxiv.org/abs/2112.08755, doi:10.48550/ARXIV.2112.08755.

[104] Yoshitaka Hatta and Takashi Ikeda. Universality, the QCD critical and tricritical point, and the quark number susceptibility. *Physical Review D*, 67(1), jan 2003. URL: https://doi.org/10.1103%2Fphysrevd.67.014028, doi:10.1103/physrevd.67.014028.

[105] Mark K. Transtrum, Benjamin B. Machta, and James P. Sethna. Why are nonlinear fits to data so challenging? *Physical Review Letters*, 104(6), 2010. URL: https://doi.org/10.1103%2Fphysrevlett.104.060201, doi:10.1103/physrevlett.104.060201.